

# **Boundary layers over wing sections**

by

Prabal S. Negi

December 2017  
Technical Reports  
Royal Institute of Technology  
Department of Mechanics  
SE-100 44 Stockholm, Sweden

Akademisk avhandling som med tillstånd av Kungliga Tekniska Högskolan i Stockholm framlägges till offentlig granskning för avläggande av teknologie doktorsexamen önsdagen den 13 December 2017 kl 15:15 i sal D3, Kungliga Tekniska Högskolan, Lindstedtsvägen 5, Stockholm.

TRITA-MEK Technical report 2017:15

ISSN 0348-467X

ISRN KTH/MEK/TR-17/15-SE

ISBN 978-91-7729-591-4

©Prabal S. Negi 2017

Universitetsservice US-AB, Stockholm 2017

*“His reading suggested a man swimming in the sea among the wreckage of his ship, and trying to save his life by greedily clutching first at one spar and then at another.”*

- Anton Chekhov  
The Bet



# Boundary layers over wing sections

Prabal S. Negi

Department of Mechanics, Linné FLOW Centre and Swedish e-Science Research Centre (SeRC), KTH Royal Institute of Technology,  
SE-100 44 Stockholm, Sweden

## Abstract

The understanding of developing boundary layers over wings is an important topic from the perspective of industrial applications. An increased understanding would be consequential not only for achieving higher fuel efficiency but also in the design of aircraft control strategies. With these aims in mind, the current work aims to further the understanding of developing boundary layer over wing sections. The study is performed with two particular perspectives in mind - unsteady aerodynamic effects in a pitching airfoil and turbulent boundary layer structure in non-equilibrium boundary layers over a stationary airfoil.

The boundary layer evolution in unsteady natural laminar flow airfoils undergoing small-amplitude pitch-oscillations is investigated. For high Reynolds numbers the origins of the non-linear unsteady aerodynamic response of laminar airfoils is explained on the basis of quasi-steady assumptions. Temporal nonlinearities in aerodynamic forces are shown to be inherently linked to the non-linearities of static aerodynamic force coefficients and that a simple phase-lag concept can model the observed non-linear unsteady response. On the other hand at lower Reynolds numbers, when there exists an unstable leading-edge laminar separation bubble, the unsteady response is dynamically rich and changes in boundary layer characteristics can be abrupt. The quasi-steady phase-lag concepts are no longer appropriate to explain the unsteady flow physics in such a case.

For the case of stationary airfoils, flow statistics for flow around an airfoil at two different Reynolds numbers are compared to assess Reynolds number effects in non-equilibrium flows. Pressure gradient effects are found to be stronger at low Reynolds numbers, leading to higher energy in the larger structures present in the outer part of the turbulent boundary layer.

**Key words:** boundary layers, unsteady aerodynamics, non-equilibrium flows

# Gränsskikt över vingsektioner

Prabal S. Negi

Institutionen för Mekanik, Linné FLOW Centre and Swedish e-Science Research Centre (SeRC), Kungliga Tekniska Högskolan  
SE-100 44 Stockholm, Sverige

## Sammanfattning

Förståelsen av det strömningsmekaniska gränsskiktet som utvecklas över vingar är av stort intresse för industriella tillämpningar. En ökad förståelse av detta är ett måste både för att uppnå en minskning av bränsleförbrukning och för för utformningen av effektivare flygstyrssystem. Med detta i åtanke, syftar detta arbetet till att vidga vår förståelse av det komplexa gränsskiktetsflödet över vingar. Studien utförs med två specifika mål i åtanke - instationära aerodynamiska effekter i strömningen över en oscillatorande vinge och strukturer i ett turbulent gränsskikt över en stationär vinge som inte är i jämvikt.

Här har vi studerat utvecklingen av ett instationär gränsskikt över en vinge designad för att ha laminär flöde (så kallade NLF vinge). Vingen genomgår oscillationer med små amplituder. För höga Reynoldstal förklaras ursprunget till det ickelinjära aerodynamiska responsen hos NLF vingar genom antagandet av kvasistationär strömning. Tidsberoende ickelinjäriteter hos de aerodynamiska krafterna visar sig vara starkt kopplade till de ickelinjäriteter hos de statiska aerodynamiska kraftkoefficienterna och med hjälp av ett enkelt fasfördröjningskoncept kan man modellera den observerade ickelinjära instationära responsen. Å andra sidan, vid lägre Reynoldstal, när det finns en instabil laminär separationsbubbla vid framkanten av vingen, visar den instationära responsen en stark dynamik och förändringar i karakteren av gränsskiktet kan vara abrupta. I sådana fall är antagandet av en kvasistationär fasfördröjning inte längre adekvat för att förklara fysiken hos det instationära flödet.

I fallet med den stationärs vingen jämför vi flödesstatistiken vid två olika Reynoldstal för att förstå effekter av detta för turbulent flöden som befinner sig i icke-jämvikt. Tryckgradientenseffekter visade sig vara starkare vid låga Reynoldstal, vilket leder till högre energi i de större strukturerna som är närvarande i den yttre delen av det turbulent gränsskiktet.

**Nyckelord:** gränsskikt, ostabil aerodynamik, icke-jämviktsflöden

## Preface

This thesis deals with boundary layers developing over a wing section. A brief introduction of the basic concepts and methods is presented in the first part. The second part contains four articles. The first two are internal technical reports. The third paper is an extended version of the paper presented at the 10<sup>th</sup> International Symposium on Turbulence & Shear Flow Phenomenon (TSFP-10), Chicago, USA. The final paper was also presented at TSFP-10. The fourth paper has been adjusted to comply with the present thesis format for consistency, but the contents have not been altered as compared with the original counterpart, except for the addition of an appendix.

**Paper 1.** NEGI, SCHLATTER & HENNINGSON. *A re-examination of filter-based stabilization for spectral-element methods.* Tech. Rep.

**Paper 2.** NEGI, HANIFI & HENNINGSON. *Dynamic response of natural laminar flow airfoils.* Tech. Rep.

**Paper 3.** NEGI, VINUESA, HANIFI, SCHLATTER & HENNINGSON. *Unsteady aerodynamic effects in small-amplitude pitch oscillations of an airfoil.* Proc. TSFP-10 (Extended version).

**Paper 4.** VINUESA, NEGI, HANIFI, HENNINGSON & SCHLATTER. *High-fidelity simulations of the flow around wings at high Reynolds numbers.* Proc. TSFP-10.

December 2017, Stockholm

*Prabal S. Negi*

## **Division of work between authors**

The main advisor for the project is Professor Dan S. Henningson (DH). Docent Ardeshir Hanifi (AH) and Assoc. Professor Philipp Schlatter (PS) act as co-advisor.

**Paper 1.** The matlab code has been developed by Prabal S. Negi (PSN). The numerical simulations have been set-up and run by PSN. The paper has been written by PSN with feedback from PS and DH.

**Paper 2.** The numerical simulation has been set-up and run by PSN. The paper has been written by PSN with feedback from AH and DH.

**Paper 3.** The numerical simulations for channel flows and pitching airfoil have been set-up and run by PSN. Numerical simulations for LES validation on wing section was setup by PSN and run by Ricardo Vinuesa (RV). The paper has been written by PSN with feedback from RV, AH, PS and DH.

**Paper 4.** The numerical simulation for the  $Re_c = 1,000,000$  case has been set-up by PSN and run by RV. The domain validation was performed by PSN. The paper has been written by RV with feedback from PSN, AH, DH and PS.

## **Conferences**

Part of the work in this thesis has been presented at the following international conferences. The presenting author is underlined.

P. S. NEGI, R. VINUESA, A. HANIFI, P. SCHLATTER & D. S. HENNINGSON. *Large-eddy simulations of a wing section undergoing small-amplitude pitch oscillations*. 16<sup>th</sup> European Turbulence Conference (ETC). Stockholm, Sweden, 2017.

P. S. NEGI, R. VINUESA, A. HANIFI, P. SCHLATTER & D. S. HENNINGSON. *Unsteady Aerodynamic effects in small-amplitude pitch oscillations of an airfoil*. 10<sup>th</sup> Int. Sym. on Turbulence & Shear Flow Phenomenon (TSFP-10). Chicago, USA, 2017.

R. VINUESA, P. S. NEGI, A. HANIFI, D. S. HENNINGSON & P. SCHLATTER. *High-fidelity simulations of the flow around wings at high Reynolds numbers*. 10<sup>th</sup> Int. Sym. on Turbulence & Shear Flow Phenomenon (TSFP-10). Chicago, USA, 2017.

P. S. NEGI, R. VINUESA, P. SCHLATTER, A. HANIFI, & D. S. HENNINGSON. *Relaxation-term filertering for SEM*. 5<sup>th</sup> Nek user's meeting. Cambridge, USA, 2016.

# Contents

<b>Abstract</b>	v
<b>Sammanfattning</b>	vi
<b>Preface</b>	vii
 <b>Part I - Overview and summary</b>	
<b>Chapter 1. Introduction</b>	1
1.1. A short history	1
1.2. Modern aircraft design	2
1.3. Boundary layers over a stationary wing	3
1.4. Unsteady boundary layers	4
<b>Chapter 2. Numerical Method</b>	7
2.1. Numerical Discretization	7
2.2. Relaxation-term large-eddy simulation (RT-LES)	7
2.3. Arbitrary-Lagrangian-Eulerian (ALE)	9
2.4. Free-stream turbulence	11
<b>Chapter 3. Overview of numerical simulations</b>	13
3.1. Flow around unsteady wings	13
3.2. Flow around a stationary wing section	15
<b>Chapter 4. Conclusions and outlook</b>	18
<b>Acknowledgements</b>	20
<b>Bibliography</b>	22

## **Part II - Papers**

<b>Summary of the papers</b>	<b>29</b>
<b>Paper 1. A re-examination of filter-based stabilization for spectral-element methods</b>	<b>31</b>
<b>Paper 2. Dynamic response of natural laminar flow airfoils</b>	<b>53</b>
<b>Paper 3. Unsteady aerodynamic effects in small-amplitude pitch oscillations of an airfoil</b>	<b>77</b>
<b>Paper 4. High-fidelity simulations of the flow around wings at high Reynolds numbers</b>	<b>103</b>

# **Part I**

## **Overview and summary**



## CHAPTER 1

# Introduction

### 1.1. A short history

The first sustained flight by the Wright brothers in 1903 marked a historic day in human achievement and ingenuity. Momentous as the achievement was, the Wright brothers did not truly invent the modern airplane. Their achievements were the fruition of nearly a century of aeronautical research, starting perhaps with Sir George Cayley, who is considered the “father of aerial navigation” (Gibbs-Smith 1962). The principal components of the modern aircraft were laid down by George Cayley as early as 1799. Prior to Cayley, the ideas for mechanical flight tended towards flapping wings, where the flapping motion produced both propulsion and lift. George Cayley was the first to break the unsuccessful chain of thought and separated the two aspects of flight into distinct systems. His triple paper “On Aerial Navigation” published in Nicholason’s *Journal of Natural Philosophy, Chemistry and the Arts* on November 1809, February and March 1810 (Cayley 1809-10) mark some of the most important works in aeronautical history. In the works, Cayley states for the first time, the principle of lift generation *i.e.* the formation of a low pressure region on the upper surface of the wing. His paper elaborates on the separation of lift from propulsion and also goes on to talk about flight control and airplane stability. Later in his life, he proposed the concept of multiplanes (multiple wings mounted on top of each other) and built the first glider triplane named the “boy carrier” in 1849.

Several investigators followed the quest of “aerial navigation”. Otto Lilienthal was the first to design and successfully fly controlled gliders in 1891, going on to make over 2500 successful glider flights. Octave Chanute brought aeronautics research to America and designed a biplane glider which directly inspired the designs of the Wright Brothers. Samuel Pierpont Langley was a contemporary of the Wright brothers who built and tested several powered model airplanes. His success in achieving powered flight directly influenced and encouraged the Wright brothers. The final historic achievement of successful powered flight was achieved by the Wright brothers. On December 17<sup>th</sup> 1903, a gasoline powered biplane by the name Wright Flyer I (figure 1.1) took flight in (modern day) Kill Devil Hills, North Carolina, ushering forth the era of practical human flight.



Figure 1.1: First flight of the Wright Flyer I, December 17, 1903, Orville piloting, Wilbur running at wingtip. Image from Wikipedia, the free encyclopedia (2017b).

## 1.2. Modern aircraft design

Since that fateful day, modern airplanes have been used in a variety of different conditions, varying from commercial passenger planes, to supersonic military aircrafts (NASA 2014), to endurance flights around the world lasting 9 days (Blakeslee 1986). The myriad uses have resulted in various challenges that need to be overcome by the aircraft designers. One significant challenge has been due to the dynamic interaction of air flow with the airplane structures, now studied under the field of aeroelasticity. These problems came to the fore as the design speed of aircrafts increased over the years and designers came to favor monoplanes over the biplane design. An early example was that of the Fokker D-8 German aircraft during World War I which suffered wing failure under steep dives, which was the first documented case of static aeroelastic effects.

Today the designers of commercial aircrafts face another challenge brought about by global climate change and rising oil prices. With the realization of the contribution of the aviation industry towards global climate change (Green 2008), aircraft designers now face a need to significantly improve the fuel efficiency of commercial aircrafts in a bid to reduce the carbon footprint of the industry. In an effort to quantify the opportunities of achieving such an improvement, Schrauf (2005) showed a break-down of the drag experienced by a typical transport aircraft highlighting that frictional drag accounted for more than half the drag experienced by the aircraft. Clearly a favorable modulation of the boundary layer over the wing could help achieve large improvements in

fuel efficiency. The modulation could come in the form of effective flow control strategies, or with wing design strategies such as the use of natural laminar flow (NLF) airfoils. Both Schrauf (2005) and Green (2008) push forward the idea that NLF airfoils and laminar flow control strategies are the low-hanging fruits in the goal of higher fuel efficiency and a concerted effort into addressing the engineering challenges for practical implementation must be made. Some of these challenges may require revisiting the aeroelasticity problems from the perspective of laminar wings. However laminar flow at high Reynolds numbers is susceptible to destabilization and may not always be possible. Thus turbulent drag reduction strategies need to be used effectively where needed (Bushnell 2003). Whatever the form of drag reduction technique that may finally be implemented on a particular aircraft, the understanding of developing boundary layers over wings (including the influence of control strategies) occupies a central position in aerodynamic research if the goal of higher fuel efficiency is to be realized. With this goal in mind, the current thesis work aims to further the understanding of developing boundary layers over airplane wings, focusing on two particular aspects.

- Understanding the structure of the turbulent boundary layer developing over a wing section.
- Understanding the evolution of the developing boundary layer over a natural laminar flow airfoil in unsteady flight conditions.

### 1.3. Boundary layers over a stationary wing

The understanding of the structure and scaling of wall-bounded turbulent flows has been in study for several decades and a complete understanding still remains far from complete. These flows have been studied with different canonical geometries such as channels (Kim *et al.* 1987; Moser *et al.* 1999; Lee & Moser 2015), pipes (El Khoury *et al.* 2013; Jiménez & Hoyas 2008; Chin *et al.* 2015) and flat plates Spalart (1988); Schlatter & Örlü (2010); Eitel-Amor *et al.* (2014). For the case of spatially evolving boundary layers over a flat plate, the simplest canonical case involves boundary-layer evolution subjected to a zero pressure gradient (ZPG). These flows may be uniquely characterized by a single parameter, *i.e.* the Reynolds number  $Re$ , which is the ratio of the inertial and viscous scales of the flow. However practical flow cases are often influenced by pressure gradients. Such flow cases can no longer be uniquely defined using a single parameter. Clauser (1954) with intuitive reasoning proposed a concept of an equilibrium boundary layer which may be uniquely defined by two parameters. He argued that, if the ratio of the average pressure gradient force across the boundary layer and the viscous shear force at the wall remains constant, the boundary layer would experience a similar flow history throughout its evolution. Thus the equilibrium pressure gradient boundary layers are uniquely defined by two parameters, namely the Reynolds number ( $Re$ ) and the pressure gradient parameter  $\beta$ , defined as

$$\beta = \delta^*(dp/dx)/\tau_w, \quad (1.1)$$

where  $\delta^*$  is the displacement thickness,  $dp/dx$  is the pressure gradient and  $\tau_w$  is the wall-shear stress. The parameter is commonly referred to as the Clauser parameter. A flow case with a spatially constant Clauser parameter is categorized as an equilibrium boundary layer and a ZPG boundary layer is a special case of an equilibrium boundary layer with  $\beta = 0$ . Several works have focused on pressure gradient boundary layers ranging from theoretical studies by Townsend (1956*a,b*); Mellor & Gibson (1966), experimental works of Skåre & Krogstad (1994); Harun *et al.* (2013) and numerical simulations by Spalart & Watmuff (1993); Skote *et al.* (1998). The developing boundary layer over an airfoil however further increases in complexity since these boundary layers fall under the category of non-equilibrium boundary layers where the Clauser parameter is spatially varying. In such cases the flow history also plays a role in determining the local boundary layer properties (Clauser 1954; Bobke *et al.* 2017). Analysis of such flow cases becomes significantly more difficult since the local boundary layer parameters do not uniquely define the state of the boundary layer. Nonetheless the study of such boundary layers is important since generic boundary layers found in nature would belong to this category, including the boundary layers over wings. The boundary layer developing over the NACA 4412 airfoil has the property that the spatially varying Clauser parameter is insensitive to Reynolds number. This presents us with the opportunity to study the Reynolds number effects of a non-equilibrium boundary layer with a constant pressure gradient history. That is indeed the methodology followed in this work. The developing boundary layer over a NACA 4412 wing section is analyzed at two different Reynolds numbers in order to understand Reynolds number effects in non-equilibrium boundary layers.

#### 1.4. Unsteady boundary layers

Unsteady aerodynamic studies started with the emergence of aeroelastic phenomenon in the early part of the 20<sup>th</sup> century. With the gradual shift to monoplane designs, the inherent high torsional stiffness of biplanes was lost and aerodynamic instabilities, such as the one experienced by the Fokker D-8 became important. Pioneering works of Glauert (1930); Karman & Sears (1938); Theodorsen (1935) *etc*, provided the insight and modeling of such unsteady aerodynamic behavior and by the 1940s the foundations of unsteady aerodynamics for incompressible attached flows had been laid down. The mathematical framework these unsteady aerodynamic theories relied on simple inviscid and quasi-steady assumptions, which proved to be highly attractive to the wing designers (Leishman 2000). Experimental corroboration by Halfman (1952) and Rainey (1957) further added support to the validity of the simple assumptions. Over the next few decades, investigations of unsteady aerodynamics shifted focus to the understanding of the dynamic stall phenomenon, with works of McCroskey *et al.* (1976); McCroskey (1981); McCroskey *et al.* (1982); McCroskey (1982); Carr *et al.* (1977); Crisler *et al.* (1994). A large body of work on unsteady separated flows was presented by Ericsson & Reding (1986, 1987, 1988*a,b*). The studies continue to this day with the works of Visbal (2011, 2014); Visbal &

Garmann (2017); Dunne & McKeon (2015) and several other authors, a recent review can be found in Coorke & Thomas (2015).



Figure 1.2: North American P-51 Mustang. Image from Wikipedia, the free encyclopedia (2017a).

However it appears that the aeroelasticity problem was not considered from the perspective of natural laminar flow airfoils. This is a surprising fact considering the P-51 Mustang (figure 1.2), a fighter aircraft in the Royal Air Force designed in 1940, incorporated a wing with a natural laminar flow airfoil section (Green 2008). The first aeroelastic study on laminar wings was performed as late as 2011 by Mai & Hebler (2011). This, along with a subsequent investigation by Hebler *et al.* (2013), brought to light a peculiar characteristic of unsteady laminar wings, *i.e.* the presence of non-linearities in the unsteady aerodynamic forces. The classical unsteady aerodynamic theories did not predict non-linear unsteady responses and thus fail to account for such behavior. Inspired by this, Lokatt (2017) performed experiments on unsteady NLF airfoils and also found strong non-linearities in the aerodynamic forces. Consistent in the explanation for the non-linearities in all these studies was the role of transition over the wing surface. When transition on the airfoil suction-side was fixed (with a trip) near the leading edge, the non-linearities seemed to disappear. These results indicated a need for a more in-depth study of the evolving boundary layer in such unsteady laminar airfoils. Classical theories negate the role of the boundary layer by invoking the inviscid assumption and it is apparent that such an assumption is no longer be justified for laminar wings.

Characteristics of the unsteady boundary layer are the subject of investigation in the present work.

**Thesis structure.** The thesis is structured as follows:

- An overview of the numerical method used for the simulations is given in Chapter 2.
- Chapter 3 gives an overview of the numerical simulations performed in the study.
- The main conclusions of the current work are given in Chapter 4 along with an outlook for future work.
- The next part of the thesis includes the individual papers and internal reports.

## CHAPTER 2

# Numerical Method

### 2.1. Numerical Discretization

The numerical code used for the simulations is Nek5000, which is an open source research code developed by Fischer *et al.* (2008) at Argonne National Laboratory. The code solves the incompressible Navier–Stokes equations (2.1) in non-dimensional form:

$$\frac{\partial u_i}{\partial t} + u_j \frac{\partial u_i}{\partial x_j} = -\frac{1}{\rho} \frac{\partial p}{\partial x_i} + \frac{1}{Re} \left( \frac{\partial^2 u_i}{\partial x_j \partial x_j} \right) + f_i \quad (2.1a)$$

$$\frac{\partial u_i}{\partial x_i} = 0 \quad (2.1b)$$

where  $x_i$  is the coordinate direction,  $u_i$  is the velocity component,  $p$  is the pressure and  $Re$  is the defined Reynolds number. The discretization of the Navier–Stokes equations is based on a spectral-element method, first proposed by Patera (1984). The method allows the mapping of elements to complex geometries along with a high-order spatial discretization within the elements, thus combining the generality of finite-element methods with the accuracy of spectral methods (Patera 1984). The spatial discretization in each element is performed following the  $P_N$ - $P_{N-2}$  (Maday & Patera 1989) formulation with velocity represented by high-order Lagrange interpolants through the Gauss–Lobatto–Legendre (GLL) quadrature points, while the pressure is represented on the staggered Gauss–Legendre (GL) quadrature points. The nonlinear terms are treated explicitly by third-order extrapolation (EXT3), while the viscous terms are treated implicitly by a third-order backward differentiation scheme (BDF3). Over-integration is used for the removal of aliasing errors. Nek5000 is written in Fortran 77 and C with efficient scaling for up to 1 million MPI ranks (Fischer *et al.* 2015).

### 2.2. Relaxation-term large-eddy simulation (RT-LES)

Owing to the high Reynolds numbers and large time-scales of integration for some of the flow cases, a direct numerical simulation (DNS), which requires a resolution of all the spatial scales of the flow, leads to prohibitively high computational costs. In recent years a technique of wall-resolved large-eddy simulations has emerged as a computationally cheaper alternative to DNS, while

also exhibiting the high-fidelity characteristics of DNS. The technique has been utilized in the studies of spatially developing boundary layers (Eitel-Amor *et al.* 2014), pipe flows (Chin *et al.* 2015) and flow over wings (Uzun & Hussaini 2010; Lombard *et al.* 2016). The success of the approach has motivated its use in the present work. The wall-resolved LES method used is based on the RT3D variant of the ADM-RT approach first used by Schlatter *et al.* (2004). The method has been shown to be reliable in accurately predicting transition and also preserving the characteristic structures which are seen in the DNS of transitional flows by Schlatter *et al.* (2006b). This particular quality of the LES model is crucial since there is a large focus on the unsteady transition in the present work. The LES method supplements the governing equations with a dissipative term  $-\chi\mathcal{H}(u)$ . The equations of motion for the resolved velocity and pressure thus read as

$$\frac{\partial u_i}{\partial t} + u_j \frac{\partial u_i}{\partial x_j} = -\frac{1}{\rho} \frac{\partial p}{\partial x_i} + \frac{1}{Re} \left( \frac{\partial^2 u_i}{\partial x_j \partial x_j} \right) + f_i - \chi\mathcal{H}(u_i), \quad (2.2a)$$

$$\frac{\partial u_i}{\partial x_i} = 0, \quad (2.2b)$$

where  $\mathcal{H}$  is a defined high-pass spectral filter and  $\chi$  is a model parameter which together with  $\mathcal{H}$  determines the strength of the dissipative term. The high-pass filter function  $\mathcal{H}$  is defined such that the resultant relaxation-term only has energy in the highest modes, defined by a cut-off mode-number  $N_c$ . Figure 2.1 illustrates the shape of the filter function in spectral space.

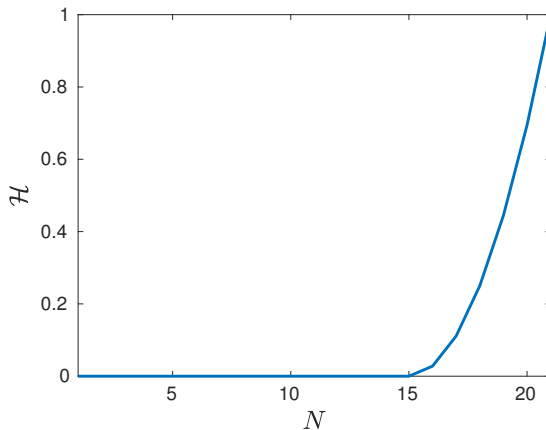


Figure 2.1: Transfer function for the spectral coefficients for the filter  $\mathcal{H}$  with number of modes  $N = 21$  and cut-off mode number  $N_c = 16$ .

Several parameter optimization studies were performed to determine the optimum value of  $\chi$  and filter shape  $\mathcal{H}$  using turbulent channel flow simulations. The LES results were compared with the DNS database of Moser *et al.* (1999) and the optimum parameters were further validated for a flow around a wing

section at  $Re_c = 400,000$ . A good agreement was found between the LES and the DNS data of Hosseini *et al.* (2016), and the optimized parameters were then used for all subsequent simulations.

### 2.3. Arbitrary-Lagrangian-Eulerian (ALE)

Typical solutions of unsteady fluid flows utilize the Eulerian framework where the coordinate system is fixed in space. A fixed coordinate system however becomes infeasible when the domain boundaries are in motion, as is the case of fluid-structure interaction problems, or when there is a free surface which may lead to a deforming interface. An appropriate method is needed to account for the motion of the boundaries and/or the interior grid points. One such method which substantially simplifies the difficulties arising out of moving boundaries is the Arbitrary-Lagrangian-Eulerian (ALE) method. The method was proposed in a finite-difference framework by Hirt *et al.* (1974) and later brought to the spectral-element framework by Ho & Patera (1990, 1991). The technique combines both the Lagrangian and Eulerian formulations such that, the Navier-Stokes may be solved with the grid points moving with the fluid elements *i.e.* in a Lagrangian framework, or with fixed grid points (Eulerian), or with grid points moving in an arbitrary prescribed manner. The heart of the technique lies in the formulation of the total time rate of change of a quantity in the ALE frame, defined analogously to the material derivative. Thus for a quantity  $\mathbf{F}(\mathbf{x}_i, t)$ , the change due to small increments  $dx_i$  and  $dt$  may be expressed as (Kundu & Cohen 2002)

$$dF = \frac{\partial F}{\partial t} dt + \frac{\partial F}{\partial x_i} dx_i. \quad (2.3)$$

One may choose to follow any arbitrary path along which this quantity is evaluated, in which case the quantities  $dx_i$  and  $dt$  are related by the velocity of the (grid) point along this arbitrary path  $w_i = dx_i/dt$ . The relation results in the expression referred to as the ALE derivative (Deville *et al.* 2004), here denoted as  $\delta F/\delta t$  to differentiate it from the very similar expression for the material derivative (which is evaluated along the fluid particle trajectory)

$$\frac{\delta F}{\delta t} = \frac{\partial F}{\partial t} + w_i \frac{\partial F}{\partial x_i}. \quad (2.4)$$

When  $w_i$  is equal to the fluid velocity  $u_i$ , we recover the familiar Lagrangian expression for the material derivative  $DF/Dt$ . On the other hand, when  $w_i = 0$ , we get the local (Eulerian) rate of change of the quantity  $F$ . The material derivative and the ALE derivative share a simple relationship defined using a relative velocity of the fluid particle with respect to the grid motion  $c_i = u_i - w_i$ , which may be used in the definition of material derivative to obtain

$$\frac{DF}{Dt} = \frac{\delta F}{\delta t} + c_i \frac{\partial F}{\partial x_i}. \quad (2.5)$$

Thus the Navier–Stokes in the ALE formulation may be expressed as

$$\frac{\delta u_i}{\delta t} + (u_j - w_j) \frac{\partial u_i}{\partial x_j} = -\frac{1}{\rho} \frac{\partial p}{\partial x_i} + \frac{1}{Re} \left( \frac{\partial^2 u_i}{\partial x_j \partial x_j} \right) + f_i, \quad (2.6a)$$

$$\frac{\partial u_i}{\partial x_i} = 0, \quad (2.6b)$$

where  $w_j$  is the velocity of the grid points. The solution of the Navier–Stokes is then a simple matter of evaluating a suitable grid velocity.

In many cases, such as the flow over an oscillating airfoil, the velocity of the grid points at the boundary (airfoil surface) may be explicitly known. Ho & Patera (1990, 1991) propose to extend this velocity to the interior points of the domain by solving an elliptic problem for the mesh velocity. In the present work we take a simpler approach to prescribing the mesh velocities in the interior domain. Recognizing the simple trigonometric form of a harmonic pitching motion, all mesh points may simply be prescribed a solid body rotation with the instantaneous angular velocity of the airfoil. However a pure solid-body rotation would also displace the domain boundaries. Therefore a damping function is used to smoothly reduce the rotational velocity away from the airfoil boundary such that the mesh motion is zero at the far-field, inlet and outflow boundaries. Thus for an airfoil with an instantaneous rotation rate of  $\Omega_z(t)$ , the mesh velocity is prescribed as:

$$w_i(x, y, z, t) = \underbrace{(\Omega_z(t) \times \vec{R})}_{\text{Solid body rotation}} \overbrace{f(|\vec{r}|)}^{\text{Damping}} \quad (2.7)$$

where  $\vec{r}$  is the normal distance of a grid point from the airfoil surface,  $\vec{R}$  is the distance from the rotational axis and  $f(r)$  is a damping function which can be prescribed in many different ways, depending on one's preferences. The damping function needs to have two essential properties, *i.e.* it must be equal to 1 when  $|\vec{r}| = 0$ , which implies the mesh points at the airfoil boundary move with the surface (solid body rotation at the airfoil surface), and it must smoothly decay to zero close to the far-field boundaries, which allows the external boundaries of the computational domain to remain fixed in physical space. Figure 2.2 shows the damping function used in the present work as a function of the normal distance from the airfoil surface. The damping function moves the grid points close to the airfoil surface with the same rotational velocity of the airfoil and spreads out the mesh deformation into the interior of the domain. This damping function is calculated once at the beginning of the simulation. Hence all quantities  $\Omega_z(t)$ ,  $\vec{r}$ ,  $f(r)$  which are needed for prescribing the mesh velocity are explicitly known at each time-step without the need for solving an elliptic equation as in Ho & Patera (1990, 1991).

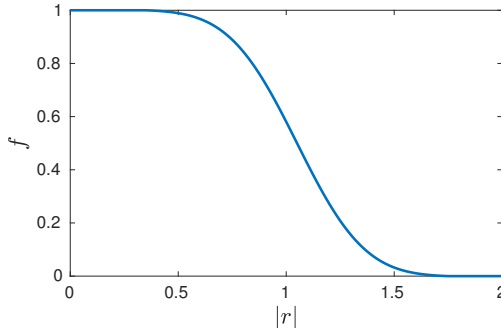
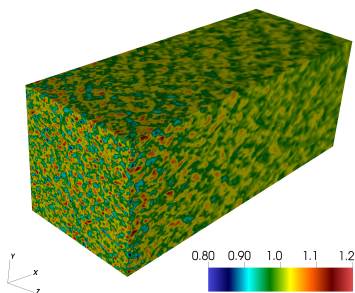


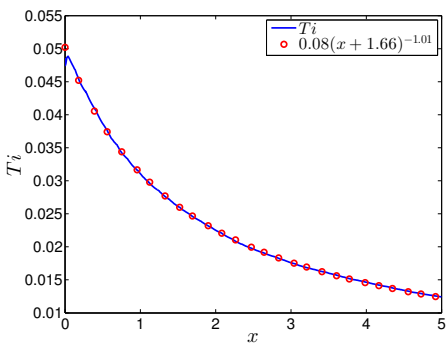
Figure 2.2: Damping function  $f(r)$  for the mesh velocities.

## 2.4. Free-stream turbulence

Isotropic, homogeneous free-stream turbulence is prescribed at the inlet and far-field boundaries to add small disturbances to the flow-field, which simulate the disturbances found in a wind-tunnel or in free-flight conditions. The free-stream turbulence is prescribed as a superposition of Fourier modes with a random phase shift. The maximum and minimum amplitudes of the wavenumber vector are prescribed quantities and are limited by the resolution of the spatial discretization and size of the domain respectively. The wavenumber space between the minimum and the maximum is divided into 20 concentric shells with each shell representing the amplitude of the three-dimensional wavenumber vectors lying on the shell. 20 points are randomly chosen on each shell with the location of each point representing the three-dimensional components of the wavenumber vector. Thus the free-stream turbulence is represented by a total of 400 fourier modes. Care is taken to avoid very small wavenumber components which result in wavelengths in physical space that are larger than the computational domain. The streamwise length scales are transformed to a temporal frequency by invoking Taylor's frozen turbulence hypothesis and using the local mean streamwise velocity at the inlet for the space-time conversion. The amplitude of the free-stream modes on each spherical shell is scaled using the von Kármán spectrum. Figure 2.3a shows an instantaneous visualization of the streamwise velocities in a doubly-periodic duct flow case with high (5%) free-stream turbulence intensity prescribed at the the inlet. Figure 2.3b shows the spatial decay of turbulence intensity. After a small initial distance of adjustment from the inlet, the turbulence intensity decays as a power law. A very similar method for generating free-stream turbulence for simulations of flat-plate boundary layers is used by Schlatter (2001); Brandt *et al.* (2004); Schlatter *et al.* (2008) and more recently for wind turbine simulations by Kleusberg (2017).



(a) Visualization of free-stream turbulence prescribed at the inlet for a doubly periodic duct flow. Colors represent the instantaneous streamwise velocity.



(b) Decay of turbulence intensity with streamwise distance, along with the least-squares fit of a power law.

## CHAPTER 3

# Overview of numerical simulations

### 3.1. Flow around unsteady wings

The unsteady experiments of Mai & Hebler (2011); Hebler *et al.* (2013) and Lokatt (2017) have shown that aerodynamic non-linearities are related to the movement of transition over the suction side of the airfoil. Thus unsteady boundary layer dynamics play an important role in aerodynamic response of NLF airfoils. The present work investigates the unsteady boundary layers with a particular focus on unsteady transition with the aim to shed light on the phenomenon of non-linear unsteady aerodynamic response. The airfoil used in the investigation is the ED36F128 (with a 13.8° flap deflection), designed at the Aeronautical and Vehicle Engineering department at KTH. It is a natural laminar flow airfoil, which has been used in several steady and unsteady experiments (Lokatt & Eller 2017; Lokatt 2017). The unsteady experiments have shown the non-linearities that appear to be typical of laminar airfoils (Lokatt 2017). The results of the steady and unsteady experiments using this airfoil have been made available to us by Dr. Eller and Dr. Lokatt. Non-linearities in the unsteady aerodynamic forces are observed for only a certain range of angle of attack  $\alpha$ . Therefore a careful assessment of the data was needed in order to select the right parameter range where the relevant flow physics could be observed in the numerical simulations. The data in the experimental campaign was gathered primarily through pressure taps located around airfoil for the calculation of unsteady aerodynamic forces. Thus measurements of the unsteady boundary layer characteristics was not available through the experimental data. Calculations using an integral boundary layer code XFOIL (Drela 1989), were used to complement the experimental data and better evaluate the state of the boundary layer in the static measurements.

Figure 3.1a shows the calculated transition locations for two different Reynolds numbers ( $Re_c = 100,000$  and  $Re_c = 750,000$ ) using XFOIL and figure 3.1b shows the experimentally measured normal force coefficient as well as calculations from XFOIL for  $Re_c = 750,000$ . For the higher Reynolds number case, transition location varies sharply with angle of attack within the range  $3.4^\circ < \alpha < 6.5^\circ$ . Aerodynamic non-linearities can also be observed approximately within the same angle of attack range (figure 3.1b). For the lower Reynolds number case, no experimental data is available. Therefore solely

XFOIL calculations are used and the parameter range is selected where the transition location varies rapidly with angle of attack. This is found for an angle of attack range of  $6.7^\circ < \alpha < 8.0^\circ$ . Numerical simulations are performed with

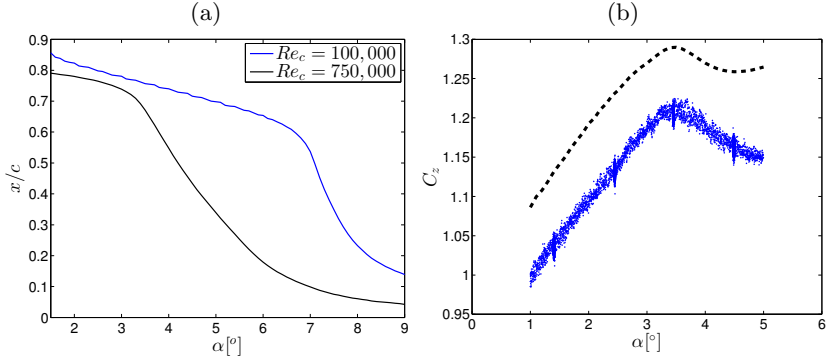


Figure 3.1: (a) Transition location calculated using XFOIL for two different Reynolds numbers. (b) Normal force coefficient measured in experiments (dots) and from XFOIL calculations (dashed line) for  $Re_c = 750,000$ .

stationary airfoils to ensure the expected static boundary layer characteristics are captured by the numerical simulations. Figure 3.2 depicts the instantaneous vortical structures in the flow for  $Re_c = 750,000$  for an angle of attack  $\alpha = 2.4^\circ$  and  $\alpha = 4.4^\circ$  which shows the change in boundary layer characteristics in the static cases. Similarly, figure 3.3 shows the static boundary layer characteristics for  $Re_c = 100,000$  at  $\alpha = 6.7^\circ$  and  $\alpha = 8.0^\circ$ .

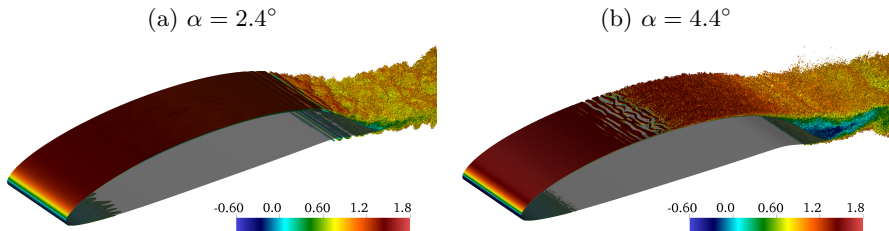


Figure 3.2: Instantaneous vortical structures identified by the  $\lambda_2$  criterion for the two stationary angle of attack simulations at  $Re_c = 750,000$ .

For both the Reynolds number cases, significant temporal variation of transition location is also found for the unsteady cases. Figure 3.4 shows

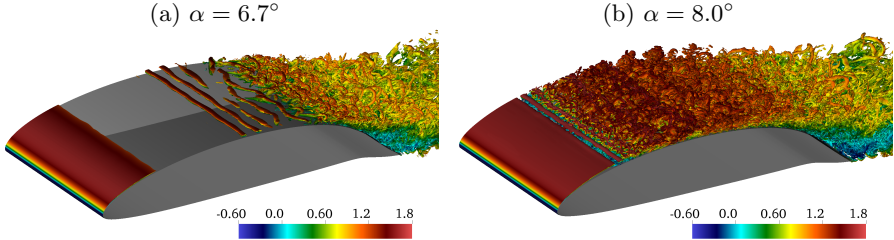


Figure 3.3: Isocontours of instantaneous  $\lambda_2$  structures observed for two different (stationary) angles of attack at  $Re_c = 100,000$ .

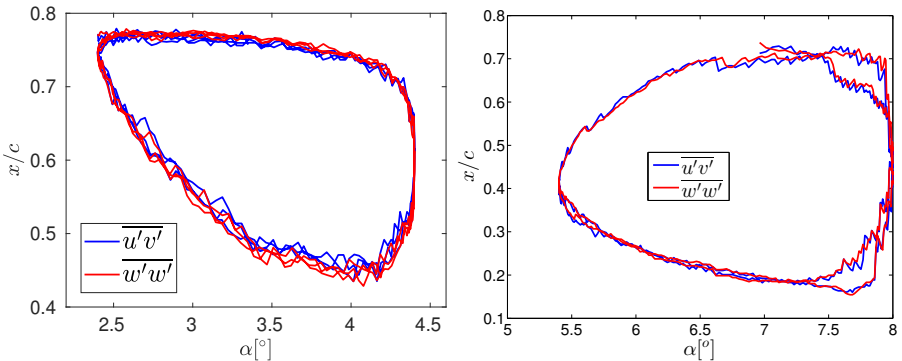


Figure 3.4: Phase portraits of transition location for (left)  $Re_c = 750,000$  and (right)  $Re_c = 100,000$ .

the variation of transition with respect to  $\alpha$ . The transition locations were calculated using thresholds on the instantaneous spanwise-averaged Reynolds stress  $\overline{u'v'}$  and spanwise fluctuation intensity  $\overline{w'w'}$ . For the lower Reynolds number case the boundary layer also develops a leading-edge laminar separation bubble during the pitch cycle which significantly influences the boundary-layer dynamics.

### 3.2. Flow around a stationary wing section

The final paper in the thesis deals with the study of the boundary layer over a wing section at a chord-based Reynolds number of  $Re_c = 1,000,000$ . The airfoil used for the study is the asymmetric NACA 4412. A DNS database for the flow around the same airfoil at  $Re_c = 400,000$  is available and comparisons are made between the two cases to assess the effects of changing Reynolds number on the developing boundary layer. The numerical setup is done in a manner very similar to the computational study by Hosseini *et al.* (2016). Figure 3.5 shows a section of the numerical grid and the instantaneous vortical structures

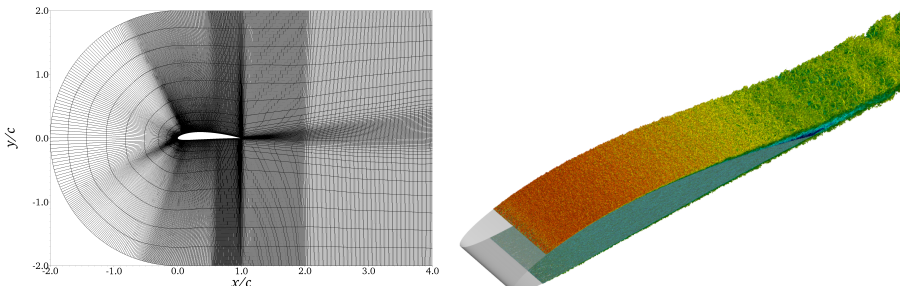


Figure 3.5: (Left) Two-dimensional slice of the computational domain showing the spectral-element distribution. (Right) Instantaneous flow field showing coherent structures identified with the  $\lambda_2$  method (Jeong & Hussain 1995), and colored with horizontal velocity. In this figure, dark blue represents a horizontal velocity of  $-0.1$  and dark red a value of  $2$ .

in the flow field. Figure 3.6 shows a comparison of the different measures of the boundary layer over the chord-wise distance for the two different Reynolds numbers. While both wall-shear stress (indicated by  $Re_\tau$ ) and boundary layer thickness (measured with momentum thickness Reynolds number  $Re_\theta$ ) change between the two cases, the Clauser parameter stays nearly the same throughout the chord. This allows comparisons across different Reynolds numbers without ambiguity since the pressure gradient histories remain the same with changing Reynolds numbers.

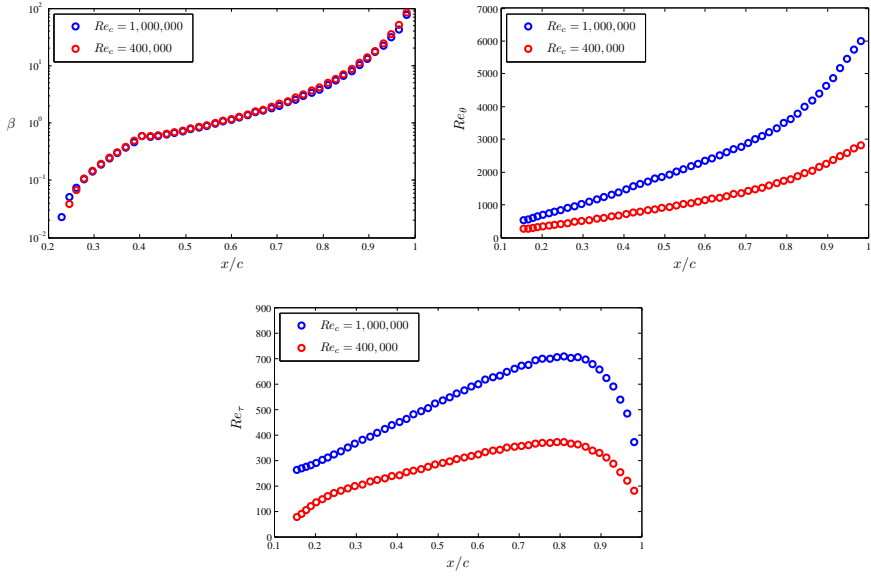


Figure 3.6: Streamwise evolution of (top left) the Clauser pressure-gradient parameter  $\beta$ , (top right) the Reynolds number based on momentum thickness  $Re_\theta$  and (bottom) the friction Reynolds number  $Re_\tau$ , for the two wing cases under study.

## CHAPTER 4

# Conclusions and outlook

The current thesis work concerns three different fields of research.

In the first part of the thesis, the “evolve and filter” technique for the stabilization of spectral-element methods is analyzed and it is found the filter operation causes an undesirable loss of divergence-free quality of the solution. This loss of divergence is shown to be particularly large for the test case of a double shear layer. An alternate formulation of the stabilization called the relaxation-term (RT) stabilization is shown to overcome the drawbacks of the explicit filtering technique, while maintaining the simplicity of the original explicit filter. This RT stabilization technique is very closely related to explicit filtering, with the two operations being equivalent to the leading order in time. Stability limits of the RT stabilization are explored and is shown to be stable within the practical parameter range.

In the second part, an NLF airfoil undergoing small-amplitude pitch-oscillations is analyzed at two different Reynolds numbers. In both cases a large variation of transition, and thus boundary layer characteristics is observed over the airfoil resulting in a non-linear response of the aerodynamic force coefficients. For  $Re_c = 750,000$  it shown that the temporal evolution of the transition point can be understood with a simple phase-lag concept, with the implication that boundary-layer evolution may be considered quasi-steady in time. Using this phase-lag concept a simple empirical model is developed which is able to explain a fairly wide range of experimental data.

On the other hand, for  $Re_c = 100,000$  a qualitatively different picture emerges for the unsteady boundary layer. The boundary-layer response displays a dynamically rich behavior with marked asymmetry of upstream and downstream transition movement. In this case, transition location is governed by the properties of the leading-edge laminar separation bubble (LSB) and it is conjectured that the absolute instability of the LSB may be responsible for abrupt changes in boundary layer characteristics.

Finally, in the third part of the study, flow over a stationary NACA 4412 airfoil is studied at two different Reynolds numbers with the aim of better understanding the boundary-layer evolution in non-equilibrium pressure gradient boundary layers. Two flow cases at a chord-based Reynolds number of  $Re_c = 400,000$  and  $Re_c = 1,000,000$  are compared at different streamwise locations.

It is found that the effect of the streamwise pressure gradients is higher at low Reynolds numbers, leading to greater energy in the larger structures present in the outer part of the turbulent boundary layer.

The current work has laid the foundation for several interesting questions that may be the focus of future work. Can the simple empirical aerodynamic model be extended for a wider range of unsteady motions? Can the phase-lag be predicted a-priori as in the case of the classical model by Theodorsen (1935)? When does the quasi-steady assumption break down and the boundary layer becomes truly unsteady? For  $Re_c = 100,000$ , can the asymmetry of the (upstream and downstream) velocities of transition point be linked with the stability properties of the LSB? What is the influence of free-stream turbulence on unsteady LSB? In stationary airfoils, how does the velocity spectrum change with Reynolds number in non-equilibrium flows? What are the characteristics of boundary layer streaks in non-equilibrium flows? Some of these questions will be the focus of further research.

## Acknowledgements

My foremost gratitude goes to my supervisor Dan Henningson for giving me the opportunity to join his research group. His knowledge and guidance have helped me immensely as a student. His encouragement, for which there is no substitute, have always provided the inspiration I needed to constantly push myself further in my work. Next I would like to thank my co-advisors Philipp Schlatter and Ardesir Hanifi. Philipp for his patience during all my ignorant and sometimes foolish questions on numerics, conferences, papers and others that I probably can't recall. Ardesir for the laughter, the sandwiches, the beers and most importantly, always being available on short notice when I needed help. I would also like to thank the members of the NFFP project, Roger Larsson, Dr. David Eller and Dr. Mikaela Lokatt for all the interesting discussions on aerodynamics.

I am grateful to Adam Peplinski for all the help he provided with Nek5000, MPI and coding in general. I can not imagine figuring out the workings of Nek5000 without his support. Armin and Ricardo have helped me more than others during my crucial time as a new Phd student. The help is greatly appreciated.

Special mentions go to Mattias for all the coffee breaks, introducing me to Swedish food, the spontaneous discussions and being the bouncing board for all my (mostly wrong) ideas. Your company shall be missed once you leave the department. Jacopo and Giandomenico for all the great company, joining for the spontaneous plans and granting me the honorary Italian citizenship. I'll learn Italian very soon I promise! Marco for the constant dinner company. Freddy for the weekend food+beer+movie routine. Elektra for being one of the greatest friends of all time. Politics, late-night and of course Trump shall keep us entertained for times to come. But mostly, thanks for correcting my manuscripts and the support during this licentiate period. A mention must also go to my unrequited love, Walter Fornari. Where will I find another like you?

A hearty thanks goes out to all my friends here at the department who make this a wonderful place. Eric, Clio, Nicolas, Sudhakar, Ugis, Evelyn, Anthony, Mehdi, Ali, Guillaume, Luca, Luca, Pierluigi, enrico, Francesco, Kristina, Ekatrina, J.C., Matthias, Priti, Ning, Sagar, Krishne, Dhiya, and

everyone else. All of you, with your quirks, jokes, stories and gossip (looking at you Pierluigi) add a little bit of color to life everyday.

Perhaps most importantly, my deepest gratitude goes towards my family for their patience, unconditional love and support during my ever wandering path through life.

Lastly, financial support for this work was provided by Vinnova through the NFFP project UMTAPS, with grant number 2014-00933, the Knut and Alice Wallenberg Foundation, and the European Research Council under grant agreement 694452-TRANSEP-ERC-2015-AdG. The computations were performed on resources provided by the Swedish National Infrastructure for Computing (SNIC) at the PDC Center for High Performance Computing at the Royal Institute of Technology (KTH). Simulation have also been performed at the Barcelona Supercomputing Center, Barcelona, with computer time provided by the 12<sup>th</sup> PRACE Project Access Call (number 2015133182) and at the High Performance Computing Center, Stuttgart (HLRS) with the computer time provided by the 15<sup>th</sup> PRACE Project Access Call (number 2016163965).

## Bibliography

- BLAKESLEE, S. 1986 Voyager succeeds in historic flight. *The New York Times* .
- BOBKE, A., VINUESA, R., ÖRLÜ, R. & SCHLATTER, P. 2017 History effects and near equilibrium in adverse-pressure-gradient turbulent boundary layers. *Journal of Fluid Mechanics* **820**, 667–692.
- BRANDT, L., SCHLATTER, P. & HENNINGSON, D. S. 2004 Transition in boundary layers subject to free-stream turbulence. *Journal of Fluid Mechanics* **517**.
- BUSHNELL, D. M. 2003 Aircraft drag reduction - a review. *Proceedings of the Institution of Mechanical Engineers, Part G: Journal of Aerospace Engineering* **217** (1), 1–18.
- CARR, L. W., MCALISTER, K. W. & MCCROSKEY, W. J. 1977 Analysis of the development of dynamic stall based on oscillating airfoil experiments. *Tech. Rep.*. NASA Ames Research Center; Moffett Field, CA, United States.
- CAYLEY, S. G. 1809-10 On aerial navigation. <http://ota.ox.ac.uk/text/3075.html>.
- CHIN, C., NG, H., BLACKBURN, H., MONTY, J. & OOI, A. 2015 Turbulent pipe flow at  $Re_\tau = 1000$ : A comparison of wall-resolved large-eddy simulation, direct numerical simulation and hot-wire experiment. *Computers and Fluids* **122**, 26 – 33.
- CLAUSER, F. H. 1954 Turbulent boundary layers in adverse pressure gradients. *Journal of Aeronautical Sciences* **21** (2), 91–108.
- COORKE, T. C. & THOMAS, F. O. 2015 Dynamic stall in pitching airfoils: Aerodynamic damping and compressibility effects. *Annual Review of Fluid Mechanics* **47** (1), 479–505.
- CRISLER, W. C., KROTHAPALI, A. & LOURENCO, L. M. 1994 PIV investigation of high speed flow over a pitching airfoil. In *32nd Aerospace Sciences Meeting and Exhibit, Aerospace Sciences Meetings, AIAA*. Reno, N.V., USA.
- DEVILLE, M. O., FISCHER, P. F. & MUND, E. H. 2004 *High-Order Methods for Incompressible Fluid Flow*. Cambridge University Press.
- DRELA, M. 1989 *XFOIL: An Analysis and Design System for Low Reynolds Number Airfoils*, pp. 1–12. Berlin, Heidelberg: Springer Berlin Heidelberg.
- DUNNE, R. & McKEON, B. J. 2015 Dynamic stall on a pitching and surging airfoil. *Experiments in Fluids* **56** (8), 157.
- EITEL-AMOR, G., ÖRLÜ R. & SCHLATTER, P. 2014 Simulation and validation of a spatially evolving turbulent boundary layer up to  $Re_\theta = 8300$ . *International Journal of Heat and Fluid Flow* **47**, 57–69.
- EL KHOURY, G. K., SCHLATTER, P., NOORANI, A., FISCHER, P. F., BRETHOUWER, G. & JOHANSSON, A. V. 2013 Direct numerical simulation of turbulent pipe flow

- at moderately high reynolds numbers. *Flow, Turbulence and Combustion* **91** (3), 475–495.
- ERICSSON, L. & REDING, J. 1986 Fluid dynamics of unsteady separated flow. part i. bodies of revolution. *Progress in Aerospace Sciences* **23** (1), 1 – 84.
- ERICSSON, L. & REDING, J. 1987 Fluid dynamics of unsteady separated flow. part ii. lifting surfaces. *Progress in Aerospace Sciences* **24** (4), 249 – 356.
- ERICSSON, L. & REDING, J. 1988a Fluid mechanics of dynamic stall part i. unsteady flow concepts. *Journal of Fluids and Structures* **2** (1), 1 – 33.
- ERICSSON, L. & REDING, J. 1988b Fluid mechanics of dynamic stall part ii. prediction of full scale characteristics. *Journal of Fluids and Structures* **2** (2), 113 – 143.
- FISCHER, P., HEISEY, K. & MIN, M. 2015 Scaling Limits for PDE-Based Simulation (Invited). In *22nd AIAA Computational Fluid Dynamics Conference, AIAA AVIATION Form*. AIAA.
- FISCHER, P. F., LOTTES, J. W. & KERKEMEIER, S. G. 2008 Nek5000 web page. <http://nek5000.mcs.anl.gov>.
- GIBBS-SMITH, C. H. 1962 Sir George Cayley\* 'Father of aerial navigation' (1773-1857). *Notes and Records of the Royal Society* **17** (1), 36–56.
- GLAUERT, H. 1930 The force and moment on an oscillating aerofoil. In *Vorträge aus dem Gebiete der Aerodynamik und verwandter Gebiete: Aachen 1929* (ed. A. Gilles, L. Hopf & T. v. Kármán), pp. 88–95. Berlin, Heidelberg: Springer Berlin Heidelberg.
- GREEN, J. E. 2008 Laminar flow control-back to the future. *38th Fluid Dynamics Conference and Exhibit, Fluid Dynamics and Co-located Conferences, AIAA 3738*.
- HALFMAN, R. L. 1952 Experimental aerodynamic derivatives of a sinusoidally oscillating airfoil in two-dimensional flow. *Tech. Rep.*.. National Advisory Committee for Aeronautics; Washington, DC, United States.
- HARUN, Z., MONTY, J. P., MATHIS, R. & MARUSIC, I. 2013 Pressure gradient effects on the large-scale structure of turbulent boundary layers. *J. Fluid Mech.* **715**, 477–498.
- HEBLER, A., SCHOJDA, L. & MAI, H. 2013 Experimental investigation of the aeroelastic behavior of a laminar airfoil in transonic flow. In *Proceedings IFASD*.
- HIRT, C., AMSDEN, A. & COOK, J. 1974 An arbitrary lagrangian-eulerian computing method for all flow speeds. *Journal of Computational Physics* **14** (3), 227 – 253.
- HO, L.-W. & PATERA, A. T. 1990 A Legendre spectral element method for simulation of unsteady incompressible viscous free-surface flows. *Computer Methods in Applied Mechanics and Engineering* **80** (1), 355 – 366.
- HO, L.-W. & PATERA, A. T. 1991 Variational formulation of three-dimensional viscous free-surface flows: Natural imposition of surface tension boundary conditions. *International Journal for Numerical Methods in Fluids* **13** (6), 691–698.
- HOSSEINI, S. M., VINUESA, R., SCHLATTER, P., HANIFI, A. & HENNINGSON, D. S. 2016 Direct numerical simulation of the flow around a wing section at moderate Reynolds number. *International Journal of Heat and Fluid Flow* **61**, 117 – 128.
- JEONG, J. & HUSSAIN, F. 1995 On the identification of a vortex. *Journal of Fluid Mechanics* **285**.
- JIMÉNEZ, J. & HOYAS, S. 2008 Turbulent fluctuations above the buffer layer of wall-bounded flows. *Journal of Fluid Mechanics* **611**, 215–236.

- KARMAN, T. V. & SEARS, W. R. 1938 Airfoil theory for non-uniform motion. *Journal of Aeronautical Sciences* **5** (10), 379–390.
- KIM, J., MOIN, P. & MOSER, R. 1987 Turbulence statistics in fully developed channel flow at low reynolds number. *Journal of Fluid Mechanics* **177**, 133–166.
- KLEUSBERG, E. 2017 Wind turbine simulations using spectral elements. Licentiate thesis, Royal Institute of Technology (KTH), Stockholm, Sweden.
- KUNDU, P. K. & COHEN, I. M. 2002 *Fluid Mechanics*. Academic press.
- LEE, M. & MOSER, R. D. 2015 Direct numerical simulation of turbulent channel flow up to  $Re_\tau \approx 5200$ . *Journal of Fluid Mechanics* **774**, 395–415.
- LEISHMAN, J. G. 2000 *Principles of Helicopter Aerodynamics*. Cambridge University Press.
- LOKATT, M. 2017 On aerodynamic and aeroelastic modeling for aircraft design. Doctoral thesis, KTH Royal Institute of Technology.
- LOKATT, M. & ELLER, D. 2017 Robust viscous-inviscid interaction scheme for application on unstructured meshes. *Computers & Fluids* **145**, 37 – 51.
- LOMBARD, J.-E. W., MOXEY, D., SHERWIN, S. J., HOESSLER, J. F. A., DHANDAPANI, S. & TAYLOR, M. J. 2016 Implicit Large-Eddy Simulation of a Wingtip Vortex. *AIAA Journal* **54**, 506–518.
- MADAY, Y. & PATERA, A. T. 1989 Spectral element methods for the incompressible Navier-Stokes equations. In *State-of-the-art surveys on computational mechanics (A90-47176 21-64)*. New York, American Society of Mechanical Engineers, 1989, p. 71-143. Research supported by DARPA., pp. 71–143.
- MAI, H. & HEBLER, A. 2011 Aeroelasticity of a laminar wing. In *Proceedings IFASD*. Paris.
- MCCROSKEY, W. J. 1981 Phenomenon of dynamic stall. *Tech. Rep.*. NASA Ames Research Center; Moffett Field, CA, United States.
- MCCROSKEY, W. J. 1982 Unsteady airfoils. *Annual Review of Fluid Mechanics* **14** (1), 285–311.
- MCCROSKEY, W. J., CARR, L. W. & McALISTER, K. W. 1976 Dynamic stall experiments on oscillating airfoils. *AIAA Journal* **14** (1), 57 – 63.
- MCCROSKEY, W. J., McALISTER, K. W., CARR, L. W. & PUCCI, S. L. 1982 An experimental study of dynamic stall on advanced airfoil sections. volume 1: Summary of the experiment. *Tech. Rep.*. NASA Ames Research Center, Moffett Field, CA, United States.
- MELLOR, G. L. & GIBSON, D. M. 1966 Equilibrium turbulent boundary layers. *J. Fluid Mech.* **24**, 225–253.
- MOSER, R. D., KIM, J. & MANSOUR, N. N. 1999 Direct numerical simulation of turbulent channel flow up to  $Re_\tau = 590$ . *Physics of Fluids* **11** (4), 943–945.
- NASA 2014 Sr-71 blackbird. [Https://www.nasa.gov/centers/armstrong/news/FactSheets/FS-030-DFRC.html](https://www.nasa.gov/centers/armstrong/news/FactSheets/FS-030-DFRC.html).
- PATERA, A. T. 1984 A spectral element method for fluid dynamics: Laminar flow in a channel expansion. *Journal of Computational Physics* **54** (3), 468 – 488.
- RAINEY, A. G. 1957 Measurement of aerodynamic forces for various mean angles of attack on an airfoil oscillating in pitch and on two finite-span wings oscillating in bending with emphasis on damping in the stall. *Tech. Rep.*. National Advisory Committee for Aeronautics. Langley Aeronautical Lab.; Langley Field, VA, United States.

- SCHLATTER, P. 2001 Direct numerical simulation of laminar-turbulent transition in boundary layer subject to free-stream turbulence. Diploma thesis, Royal Institute of Technology (KTH), Stockholm, Sweden.
- SCHLATTER, P., BRANDT, L., DE LANGE, H. C. & HENNINSON, D. S. 2008 On streak breakdown in bypass transition. *Physics of Fluids* **20** (10), 101505.
- SCHLATTER, P. & ÖRLÜ, R. 2010 Assessment of direct numerical simulation data of turbulent boundary layers. *Journal of Fluid Mechanics* **659**, 116–126.
- SCHLATTER, P., STOLZ, S. & KLEISER, L. 2004 LES of transitional flows using the approximate deconvolution model. *International Journal of Heat and Fluid Flow* **25** (3), 549 – 558, turbulence and Shear Flow Phenomena (TSFP-3).
- SCHLATTER, P., STOLZ, S. & KLEISER, L. 2006 Large-eddy simulation of spatial transition in plane channel flow. *Journal of Turbulence* **7**, N33.
- SCHRAUF, G. 2005 Status and perspectives of laminar flow. *The Aeronautical Journal* **109** (1102), 639–644.
- SKOTE, M., HENNINSON, D. S. & HENKES, R. A. W. M. 1998 Direct numerical simulation of self-similar turbulent boundary layers in adverse pressure gradients. *Flow Turbul. Combust.* **60**, 47–85.
- SKÅRE, P. E. & KROGSTAD, P.-R. 1994 A turbulent equilibrium boundary layer near separation. *J. Fluid Mech.* **272**, 319–348.
- SPALART, P. R. 1988 Direct simulation of a turbulent boundary layer up to  $r_\theta = 1410$ . *Journal of Fluid Mechanics* **187**, 61–98.
- SPALART, P. R. & WATMUFF, J. H. 1993 Experimental and numerical study of a turbulent boundary layer with pressure gradients. *J. Fluid Mech.* **249**, 337–371.
- THEODORSEN, T. 1935 General theory of aerodynamic instability and the mechanism of flutter. *Tech. Rep.*. National Advisory Committee for Aeronautics; Langley Aeronautical Lab.; Langley Field, VA, United States.
- TOWNSEND, A. A. 1956a The properties of equilibrium boundary layers. *Journal of Fluid Mechanics* **1** (6), 561–573.
- TOWNSEND, A. A. 1956b The Structure of Turbulent Shear Flow. *Cambridge Univ. Press, Cambridge, UK*.
- UZUN, A. & HUSSAINI, M. Y. 2010 Simulations of vortex formation around a blunt wing tip. *AIAA Journal* **48**, 1221–1234.
- VISBAL, M. R. 2011 Numerical investigation of deep dynamic stall of a plunging airfoil. *AIAA Journal* **49** (10), 2152 – 2170.
- VISBAL, M. R. 2014 Analysis of the onset of dynamic stall using high-fidelity large-eddy simulations. In *52nd Aerospace Sciences Meeting, AIAA SciTech Forum*. AIAA.
- VISBAL, M. R. & GARMANN, D. J. 2017 Numerical investigation of spanwise end effects on dynamic stall of a pitching naca 0012 wing. In *55th AIAA Aerospace Sciences Meeting, AIAA SciTech Forum*. AIAA.
- WIKIPEDIA, THE FREE ENCYCLOPEDIA 2017a North American P-51 Mustang.
- WIKIPEDIA, THE FREE ENCYCLOPEDIA 2017b Wright Brothers.



## **Part II**

## **Papers**



# Summary of the papers

## Paper 1

*A re-examination of filter-based stabilization for spectral-element methods*

We revisit the “filter-based stabilization” approach proposed by Fischer & Mullen (2001) and find that the loss of divergence-free condition due to commutation errors can be particularly severe in the cases of marginally resolved flows. In light of this, an alternative approach based on “relaxation-term-based stabilization” is proposed which is closely related to the explicit filter operation. The method retains the advantages of simplicity and efficiency of an explicit filter while also remedying some of its drawbacks. The effect of this relaxation-term is analyzed and it found to be an effective method of stabilization within the practical parameter range. Parameter limits of the stabilization procedure are also presented.

## Paper 2

*Dynamic response of natural laminar flow airfoils*

Large-eddy simulations are performed to investigate the dynamic response of a natural laminar flow airfoil undergoing harmonic pitch oscillations at a chord based Reynolds number of  $Re_c = 750,000$ . Large changes in the transition location are observed throughout the pitch cycles which leads to a non-linear response of the aerodynamic force coefficients. Preliminary results show that the evolution of the boundary layer over the airfoil can be modeled by using a simple phase-lag concept which implies that the boundary-layer evolution is quasi-steady in nature. A simple empirical model is developed based on this quasi-steady, phase-lag assumption which fits very well with the measured experimental data.

## Paper 3

*Unsteady aerodynamic effects in small-amplitude pitch oscillations of an airfoil*

High-fidelity wall-resolved large-eddy simulations (LES) are utilized to investigate the flow-physics of small-amplitude pitch oscillations of an airfoil at  $Re_c = 100,000$ . The investigation of the unsteady phenomenon is done in the context of natural laminar flow airfoils, which can display sensitive dependence

of the aerodynamic forces on the angle of attack in certain “off-design” conditions. The dynamic range of the pitch oscillations is chosen to be in this sensitive region. Large variations of the transition point on the suction-side of the airfoil are observed throughout the pitch cycle resulting in a dynamically rich flow response. Changes in the stability characteristics of a leading-edge laminar separation bubble has a dominating influence on the boundary layer dynamics and causes an abrupt change in the transition location over the airfoil. The LES procedure is based on a relaxation-term which models the dissipation of the smallest unresolved scales. The validation of the procedure is provided for channel flows and for a stationary wing at  $Re_c = 400,000$ .

## Paper 4

### *High-fidelity simulations of the flow around wings at high Reynolds numbers*

Reynolds-number effects in the adverse-pressure-gradient (APG) turbulent boundary layer (TBL) developing on the suction side of a NACA4412 wing section are assessed in the present work. To this end, we conducted a well-resolved large-eddy simulation of the turbulent flow around the NACA4412 airfoil at a Reynolds number based on freestream velocity and chord length of  $Re_c = 1,000,000$ , with  $5^\circ$  angle of attack. The results of this simulation are used, together with the direct numerical simulation by Hosseini *et al.* (Int. J. Heat Fluid Flow **61**, 2016) of the same wing section at  $Re_c = 400,000$ , to characterize the effect of Reynolds number on APG TBLs subjected to the same pressure-gradient distribution (defined by the Caluser pressure-gradient parameter  $\beta$ ). Our results indicate that the increase in inner-scaled edge velocity  $U_e^+$ , and the decrease in shape factor  $H$ , is lower in the APG on the wing than in zero-pressure-gradient (ZPG) TBLs over the same Reynolds-number range. This indicates that the lower- $Re$  boundary layer is more sensitive to the effect of the APG, a conclusion that is supported by the larger values in the outer region of the tangential velocity fluctuation profile in the  $Re_c = 400,000$  wing. Future extensions of the present work will be aimed at studying the differences in the outer-region energizing mechanisms due to APGs and increasing Reynolds number.

1

Paper 1



# A re-examination of filter-based stabilization for spectral-element methods

P. S. Negi, P. Schlatter and D. S. Henningson

Department of Mechanics, Linné FLOW Centre and Swedish e-Science Research Centre (SeRC), KTH Royal Institute of Technology, SE-100 44 Stockholm, Sweden

*Technical Report*

We revisit the “filter-based stabilization” approach proposed by Fischer & Mullen (2001) and find that the loss of divergence-free condition due to commutation errors can be particularly severe in the cases of marginally resolved flows. In light of this, an alternative approach based on “relaxation-term-based stabilization” is proposed which is closely related to the explicit filter operation. The method retains the advantages of simplicity and efficiency of an explicit filter while also remedying some of its drawbacks. The effect of this relaxation-term is analyzed and it found to be an effective method of stabilization within the practical parameter range. Parameter limits of the stabilization procedure are also presented.

---

## 1. Introduction

Stability of numerical methods is a well-known challenge. This is particularly true in the case of high Reynolds number ( $Re$ ) flows where low physical dissipation allows small numerical errors to grow in time. Especially if the solution method provides very low numerical dissipation as is the case with high-order methods. A particular type of numerical oscillation arises due to the violation of the *inf-sup* or Ladyzenskaya-Brezzi-Babuška (LBB) condition. These occur due to inconsistent approximation spaces for the velocity and pressure and are found in both high and low Reynolds number flows. Instabilities specific to high Reynolds number flows have often been associated with the non-linear advection term. These instabilities have been known since Phillips (1959), who showed an instability arising due to non-linear interactions within a finite difference scheme. Phillips was able to remove the instability by periodically removing energy from half the wavelengths in the simulation. Orszag (1971) noted that only the highest third of the scales are necessary to be filtered out. The effects of aliasing due to non-linear interactions on the flow quality are discussed in Krist & Zang (1987); Chow & Moin (2003) and Canuto *et al.* (1988). For non-uniform grids, Kirby & Karniadakis (2003) showed improved stability and accuracy of the incompressible Navier–Stokes solutions for spectral-element methods when using consistent integration (over-integration) of the non-linear

term. This involves the evaluation of the non-linear term on a higher number of grid points, which provides a complete integration of the term. Malm *et al.* (2013) showed that the non-linear advection term is skew-symmetric and an incomplete integration of this term leads to a loss of skew-symmetry. This loss of skew-symmetry causes some of the eigenvalues of the operator to have a positive real part, in turn leading to numerical instability. These works on aliasing, over-integration and skew-symmetry provide valuable insight into the numerical instability associated with the advection term. However the current knowledge of the sources of numerical instability does not appear to be exhaustive. Indeed Malm *et al.* (2013) show that one of their test cases suffered from numerical instability despite the use of over-integration. The authors conjecture that even small amounts of errors in divergence would lead to instability. The same test cases were used by Fischer & Mullen (2001) where the authors say that they were unable to stabilize the simulation with only over-integration within a reasonable resolution. In light of these issues other methods are necessary to suppress numerical oscillations. One of the earliest methods employed simple addition of a second order dissipative operator by Von Neumann & Richtmyer (1950). Tadmor (1989) first proposed the spectral vanishing viscosity (SVV) method for the stabilization of a 1D Burgers' equation. Maday *et al.* (1993) used SVV in the context of legendre pseudospectral methods. The method was used for a large-eddy simulation (LES) by Karamanos & Karniadakis (2000) and further shown as a useful stabilization method for spectral element methods (Kirby & Sherwin 2006). An alternate method that has been proposed in the context of spectral element methods has been that of filter-based stabilization by Fischer & Mullen (2001). Instead of adding a dissipative term to the Navier-Stokes, the method involves a simple two-step procedure of “*evolve one time-step and filter*”. This particular stabilization strategy has been analyzed in some detail by Eryin *et al.* (2012). The filter function is a low-pass filter, built in modal space. The loss of  $C_0$  continuity which occurs when applying the low-pass filter can be averted by using a simple basis transformation which preserves the physical values at the element boundaries after the application of the filter (Boyd 1998). This completely negates the need for inter-element information transfer and thus makes the filtering operation local to each spectral-element. The method has been shown to be effective at stabilizing flows even at high Reynolds numbers and the simplicity of the method is highly attractive. However, it suffers from a few potential drawbacks. For one, the “*evolve and filter*” operation is time-step dependent with more energy being filtered out of the system for a smaller time-step since that requires more time-steps to solution and hence more filter applications. Secondly the simple transform procedure introduced by Boyd (1998) creates a filter operation which is not strictly dissipative and may in some situations be a source of energy in the flow. This was pointed out by Pasquetti & Xu (2002) and also mentioned in the original paper by Fischer & Mullen (2001). However Pasquetti & Xu (2002) note that to their knowledge such a redistribution of energy has not led to anomalies in the results. A third drawback involves the violation of the divergence-free condition of the

incompressible Navier–Stokes. The “evolution” part of the method solves for a divergence-free field at each time-step. Since the filter operation is applied after this evolution and the filter operation does not commute with the derivative operation, the divergence-free property of the solution is lost. Typically, for well-resolved flow cases less than 1% of energy of the highest spectral mode is filtered out at each time-step. For well-resolved flows, the energy in the highest mode is expected to be negligibly small and thus this operation is not expected to create large errors. However, in the case of marginally resolved flows, this could potentially lead to sizable errors in the divergence. In the light of these potential drawbacks, the filter-based stabilization technique is re-examined. We start by looking at the filter formulation proposed by Boyd (1998). For the sake of completeness we include some of theory that may already be found in Boyd (1998); Fischer & Mullen (2001) and Pasquetti & Xu (2002).

## 2. Filter-based stabilization

In spectral methods, a convenient strategy for the reduction of numerical noise is to replace the finite order spectral representation of a solution  $u_N$  with a filtered solution  $\bar{u}_N$  such that

$$u_N(x) = \sum_{i=0}^N a_i P_i(x) \rightarrow \bar{u}_N(x) = \sum_{i=0}^N \sigma_i a_i P_i(x). \quad (1)$$

In the context of spectral-element methods  $P_i(x)$  may be Legendre or Chebyshev polynomials.  $a_i$  are the spectral coefficients for the finite series expansion of the solution and  $\sigma_i$  is a defined filter transfer function. While the procedure is simple, it violates the boundary conditions of the solution such that  $u_N(\pm 1) \neq \bar{u}_N(\pm 1)$ . The solution to the problem as proposed by Boyd (1998) was to apply the filter function on a transformed basis  $\phi_i(x)$  defined as

$$\phi_i(x) = P_{i+2}(x) - P_i(x). \quad (2)$$

The filtering operation may now be represented as

$$u_N(x) = \sum_{i=0}^N b_i \phi_i(x) \rightarrow \bar{u}_N(x) = \sum_{i=0}^N \sigma_i b_i \phi_i(x), \quad (3)$$

where  $b_i$  are the coefficients in this new transformed basis. This meant that in practical flow cases where one may wish to remove energy from highest mode  $P_N$ , only mode  $P_{N-2}$  needs to be modified in order to preserve the boundary points of the solution. This is a convenient operation since it only affects the high wavenumber modes while leaving the low wavenumber spectrum untouched. However this creates a filtering procedure which is not purely dissipative, as pointed out by Pasquetti & Xu (2002); Fischer & Mullen (2001). To take an example where one filters out a fraction “ $\alpha$ ” of the last mode such that

$$\sigma_i = \begin{cases} 1, & i < N \\ 1 - \alpha, & i = N. \end{cases} \quad (4)$$

After applying the filter in the transformed basis, the filtered solution in the original basis is

$$\bar{u}_N = \sum_{i=0}^{N-3} a_i P_i + (a_{N-2} + \alpha a_N) P_{N-2} + a_{N-1} P_{N-1} + (1 - \alpha) a_N P_N \quad (5)$$

In terms of difference in energy between the unfiltered and filtered solution, one can easily obtain the expressions:

$$\Delta E = \|u_N\|_w^2 - \|\bar{u}_N\|_w^2 \quad (6)$$

$$\begin{aligned} \Delta E &= (a_{N-2}^2 + (a_{N-2} + \alpha a_N)^2) P_{N-2}^2 + (1 - (1 - \alpha)^2) a_N^2 P_N^2 \\ \Delta E &= a_N^2 \underbrace{[(r^2 - (r + \alpha)^2) P_{N-2}^2 + (1 - (1 - \alpha)^2) P_N^2]}_{\gamma}. \end{aligned} \quad (7)$$

Here  $r$  is the ratio of  $a_{N-2}$  and  $a_N$ , *i.e.* the ratio of the modal coefficients of the two modes affected by the filter operation. To understand the dissipative character of the filter one can look at the sign of the term denoted as  $\gamma$  in equation 7 parametrically with  $r$  and  $\alpha$  for certain polynomial approximation order  $N$ . Figure 1 demarcates the regions of positive and negative  $\gamma$  for a polynomial order  $N = 10$ . Interestingly the filter acts as an energy source in a fairly large region in this  $r$ - $\alpha$  plane. This qualitative picture does not change substantially with changing polynomial orders. While slightly surprising, this may not necessarily be a negative characteristic of the filter. Fischer & Mullen (2001) and Malm *et al.* (2013) show the filter to be effective in stabilizing flows without any apparent adverse effects.

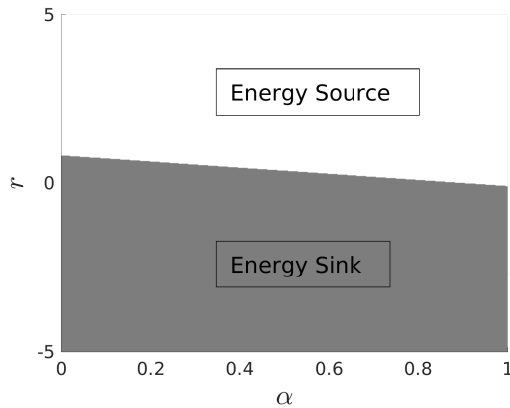


Figure 1: Dissipative character of filtering for polynomial order  $N = 10$ . Grey regions indicate the filter is dissipative while the white region indicates energy is being introduced into the flow by the filter.

The other aspect of the filtering operation which was not discussed by Fischer & Mullen (2001) is its effect on the divergence-free condition. Since the

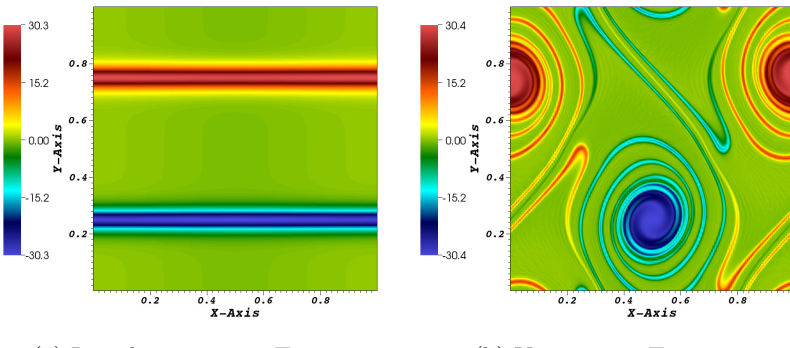
filtering operation is performed after the divergence-free condition is enforced, the filtered solution loses this quality. This error arises because the filter and derivative operators do not commute. Such commutation errors have previously been discussed in the context of large-eddy simulations by several authors (van der Bos & Geurts 2005; Geurts & Holm 2006; Geurts *et al.* 1997; Domaradzki & Adams 2002; Vasilyev *et al.* 1998). In order to asses the effects on divergence we revisit the double shear layer case studied in Fischer & Mullen (2001) and Malm *et al.* (2013).

The flow case is setup in a two-dimensional domain  $\Omega = [0, 1]^2$  with doubly-periodic boundary conditions. The initial conditions are introduced as:

$$u_0 = \begin{cases} \tanh(\rho(y - 0.25)), & y \leq 0.5 \\ \tanh(\rho(0.75 - y)), & y > 0.5 \end{cases} \quad (8)$$

$$v_0 = 0.05 \sin(2\pi x), \quad \forall x, y$$

The domain is discretized with  $16 \times 16$  spectral-element grid and each element uses  $N = 16$  Legendre polynomial modes, corresponding to 256 points per element. The non-linear term is calculated using over-integration so as to preserve skew-symmetry of the advection term. The filtering stabilization procedure is also used to asses the effect of filtering on the divergence. 1% of the last mode is filtered out at the end of each time-step. The tolerance of the solver for the divergence free condition is set to  $10^{-10}$ . Figure 2a shows the initial condition at time  $T = 0$  and Figure 2b shows the flow state at time  $T = 2$ .



(a) Initial vorticity at  $T = 0$

(b) Vorticity at  $T = 2.0$

Figure 2: Vorticity evolution for the double shear layer test case.

Figure 3 shows the divergence of the flow field calculated before and after the application of the filter. At the start of the simulation, when negligible energy is present in the last mode, the filter has very little impact on the divergence of the flow-field. However as the flow evolves and the energy in the smaller scales increase, violation of the divergence-free condition due to

the action of the filter increases. This violation is significant once the flow is fully developed, with the flow dropping nearly 6 orders of magnitude in accuracy between the pressure-correction and the filtering step. This impact is surprisingly large. The case may be considered to be a stringent test with thin shear layers, which demand high resolution and thus even the small scales may contain dynamically significant energy. The situation however is representative of marginally resolved simulations where the smallest scales may still contain dynamically relevant energy, and thus filtering may have an unexpectedly large impact on the divergence-free condition of the flow-field.

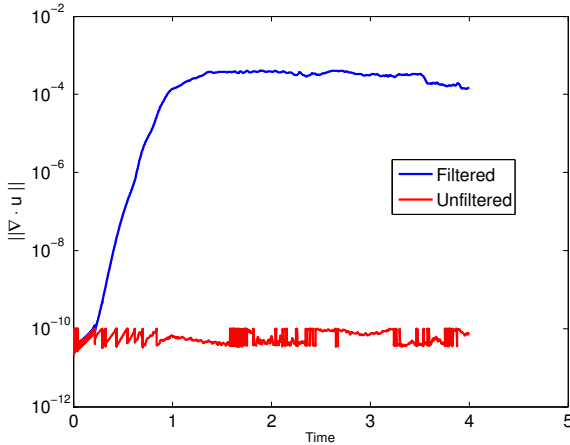


Figure 3: The norm of the divergence after pressure correction and after filter application.

A puzzling aspect of the test as reported in the results of Fischer & Mullen (2001) and Malm *et al.* (2013) is that the case always needed some filter based stabilization. Malm *et al.* (2013) study the case with and without the use of over-integration for the non-linear term. They report that an order of magnitude lower filtering strength was needed when over-integration was used. However only over-integration did not ensure complete stabilization and the simulation experienced numerical instability at  $T \sim 6.7$  without filtering. Malm *et al.* (2013) attribute the destabilization to the finite accuracy of the divergence-free constraint, stating that even small errors would lead to numerical instability in the absence of dissipative terms (viscous or numerical) or stabilizing procedures (filtering). Although the authors do not report the tolerance to which the divergence-free condition was satisfied. To check this again we run our test case with over-integration and without any filtering for a long duration. However contrary to the results obtained in Malm *et al.* (2013), the simulation was stable (at least up to  $T = 20$ ). An explanation might be found when looking at the original test case reported in Fischer & Mullen (2001). The authors there report using time steps such that the CFL number is between 1 and 5. The standard

BDF3-K3 time-stepper would be unstable for these CFL numbers. This suggests that a characteristic time-stepping scheme may have been employed. We test the case by employing a the characteristic time-stepping scheme with over-integration but no filtering and indeed the simulation experienced numerical instabilities. This would implicate the characteristics time-stepper as the source of numerical instability.

In retrospect, the results are to be expected. The use of consistent spaces for velocity and pressure avoids the spurious pressure oscillations. The absence of boundary conditions due to a doubly-periodic domain negates errors due to boundary terms, the use of over-integration dismisses aliasing errors as the source of instabilities and the spectral-element grid is perfectly Cartesian. Then as per the conclusion derived in Malm *et al.* (2013), small divergence errors remain the obvious (known) source of numerical instability. However, these errors should be of the order of the specified solver tolerance for divergence. The (instantaneous) advection operator being real and skew-symmetric is a normal matrix (if evaluated completely using over-integration). Any violation of divergence-free condition of  $O(\epsilon)$  can be regarded as a small perturbation to a normal matrix and one would expect a change in the eigenvalues to be of the same order  $\epsilon$ . Since in the ideal case the eigenvalues must lie on the imaginary axis with exactly zero real part, any perturbation due to numerical errors of order  $O(\epsilon)$  would introduce new eigenvalues with a real part of  $O(\epsilon)$ . Thus a practical value for the solver tolerance of  $10^{-8}$  would result in an advection matrix which would have eigenvalues with real parts of the order  $10^{-8}$ . Such a scenario creates an ever present numerical instability. However it should be an extremely weak instability, at least in such idealized test cases where other sources of instabilities are absent.

One can easily check the change of eigenvalues with varying degree of error in the advecting field. To do so we created a simple advection operator in Matlab following the spectral-element framework. A square domain with  $\Omega = [0, 1]^2$  is built and discretized using  $3 \times 3$  spectral-elements which are further discretized using  $10^{\text{th}}$  order Legendre polynomials. The advection operator is built on an over-integration grid with  $19 \times 19$  grid points. The grid point spacing and weights for numerical integration correspond to the Gauss-Lobatto-Legendre points (GLL) for a polynomial of order  $N_d = 18$  resulting in the desired 18 grid points for a complete integration of the convection term. Individual matrices are built independently for each spectral element and then a larger matrix for the whole system is built using direct stiffness summation. A simple sinusoidal divergence-free field can be used for building the  $C \cdot \nabla$  matrix:

$$\begin{aligned} C_x &= 1.0 + 0.1 \sin(2\pi x + 2\pi y) & + \epsilon \sin(2\pi x) \sin(2\pi y) \\ C_y &= 1.0 - 0.1 \sin(2\pi x + 2\pi y) & + \epsilon \sin(2\pi x) \sin(2\pi y) \end{aligned} \quad (9)$$

When  $\epsilon = 0$  the field is analytically divergence free. Within the current numerical approximation the normalized divergence field defined as  $\|\nabla \cdot C\| = (\nabla \cdot C, \nabla \cdot C)/\text{Volume}$  is of the order  $10^{-11}$ . The parameter  $\epsilon$  can thus be

used to add a controlled perturbation to the advecting field and study the resulting change in eigenvalues. Figure 4a and 4b show the spectra of advection operator using  $\epsilon = 0$  and  $\epsilon = 10^{-4}$ , resulting in divergence norms of the order  $O(10^{-11})$  and  $O(10^{-4})$  respectively. Tracking  $\lambda_{max}$ , defined as the eigenvalue with the largest real part, one can obtain how the instability of the advection operator changes with the variation of the divergence field. Figure 5 shows the change in  $\lambda_{max}$  with  $\|\nabla \cdot C\|$ . As expected the trend is linear in a log-log scale with a slope of 1 across a variation of 8 orders of magnitude for  $\|\nabla \cdot C\|$ . This would suggest that relatively large divergence errors would be required for numerical instabilities to be caused by the advection term, as long as the term is evaluated completely. Of course as shown by Malm *et al.* (2013) and by Kirby & Karniadakis (2003), the evaluation of this term without over-integration leads to instabilities in the absence of stabilization. These instabilities are much stronger than just divergence errors. Figure 6 shows the eigenvalue spectra for the advection operator (with  $\epsilon = 0$ ) evaluated on  $11 \times 11$  GLL points in each element. The largest unstable eigenvalue is of the order  $10^{-1}$ , making the instability due to aliasing much stronger than the instabilities arising from the violation of the divergence-free condition. Malm *et al.* (2013)

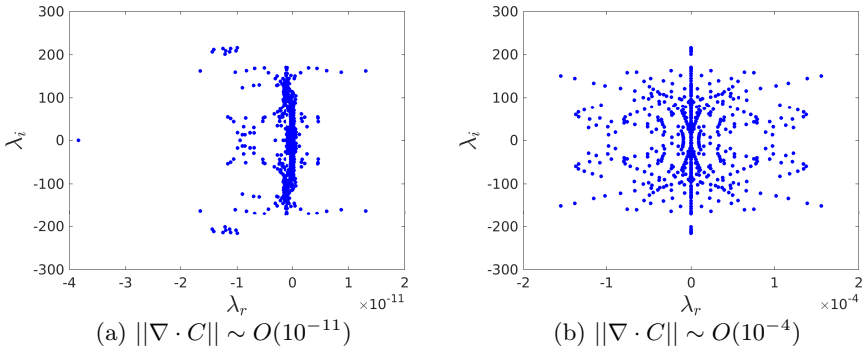


Figure 4: Eigenvalue spectra for the advection operator with different divergence norms for a perturbed advecting field.

found that for the double shear layer case, the numerical instabilities first manifested in the thinnest part of the shear layers, thus concluding high shear regions necessarily need numerical stabilization. Since we do not experience any numerical instabilities using the BDF-EXT-k time stepping scheme, we further test this conclusion by reducing the resolution for the test case. We run the simulation with the same  $16 \times 16$  spectral-elements but with polynomial orders of  $N = 11, 7$  and  $5$ . These would lead to under-resolved shear layers. The under-resolution is strongly visible in the flow-field for the lowest polynomial order case of  $N = 5$ . Figure 7 shows the vorticity in the flow field at time  $t = 1.0$  for  $N = 5$ . However in all cases we find that the simulation does not

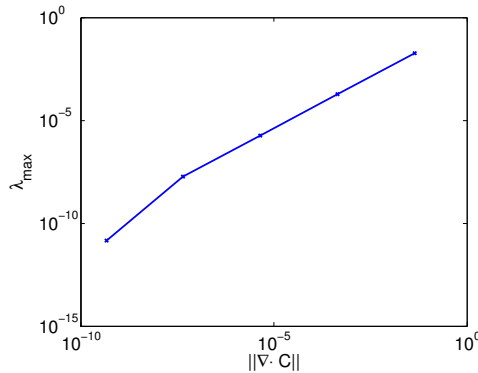


Figure 5: Variation of maximum real part of the eigenvalue spectrum with the norm of the divergence of the advection operator

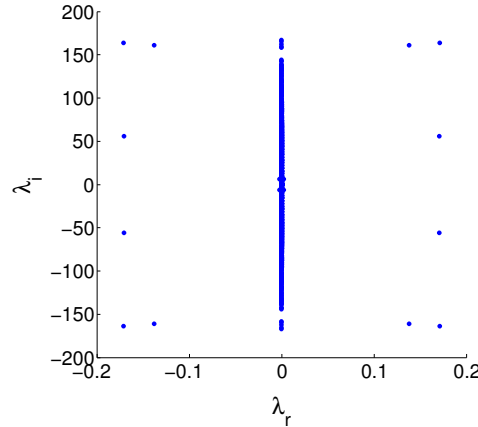


Figure 6: Eigenvalues for the advection term evaluated without over-integration

experience any numerical instabilities (at least up till  $T = 20$ ) and additional stabilization was not required. The results indicate that in the absence of boundary terms and other sources of errors, under-resolution alone may not lead to numerical instabilities as long as the flow-field divergence remains small and the non-linear term is evaluated using complete over-integration. These results are consistent with those presented by Kirby & Karniadakis (2003) who found that they were able to simulate transition and turbulence in triangular ducts as well as turbulent channel flow simulations after employing over-integration but without additional flow stabilization.

### 3. Relaxation-term based stabilization

In practical simulations aliasing errors may not be the only source of numerical instability and often it is found that simulations, especially those involving

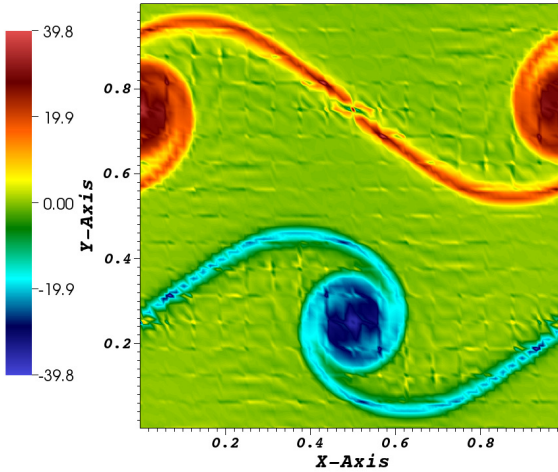


Figure 7: Vorticity at  $T = 1.0$  for the double shear layer case using polynomial order  $N = 5$

complex geometries or truncated domains require some amount to stabilization despite the use of over-integration. Filter-based stabilization has been an effective and efficient method to suppress such numerical instabilities. However the results of the previous section highlight some of the drawbacks of such a procedure. The loss of divergence free condition may be particularly severe for marginally resolved cases. In such a scenario, one may wish to look for an alternative method which preserves the advantages of explicit filtering, namely, efficiency and simplicity, while doing away with the potential drawbacks. One possible alternative in the context of the pressure-correction method is to perform the filtering procedure before the pressure-correction step. In the standard algorithm, the pressure-correction would follow a three-step procedure as follows:

- Velocity prediction → Pressure correction → Filtering.

A modified procedure would then follow:

- Velocity prediction → Filtering → Pressure Correction.

This allows the filtering of the highest scales but leaves the solution unchanged after the divergence-free condition has been enforced. Such a procedure would remedy perhaps the most striking drawback of explicit filtering, which is the loss of divergence, while still retaining the simplicity and efficiency of explicit filtering operation. However the other drawbacks mentioned earlier, *i.e* time-step dependence of filtered energy and the statistical nature of filter dissipation, still remain.

As it would turn out, there is an equally simple method that can resolve all the above mentioned deficiencies and is analogous to performing an explicit filtering procedure. As has been pointed out in Stolz *et al.* (2001); Mathew *et al.* (2003) and Schlatter *et al.* (2004), performing an explicit filtering operation is equivalent to an implicit time-relaxation. Formally, the two may be shown to be equivalent using a simple evolution equation

$$\frac{\partial u}{\partial t} + \mathcal{F}(u) = 0, \quad (10)$$

where  $\mathcal{F}(u)$  is a (possibly non-linear) evolution operator. The explicit filtering procedure may then be shown using a semi-discretized form of the evolution equation

$$\begin{aligned} u^* &= u^n - \mathcal{F}(u^n)\Delta t + O(\Delta t^2) \\ u^{n+1} &= \mathcal{G}(u^*), \end{aligned} \quad (11)$$

where  $\mathcal{G}$  is a defined low-pass filter. As an alternate method, one may consider the same evolution equation supplemented by a relaxation-term

$$\frac{\partial u}{\partial t} + \mathcal{F}(u) = -\chi \mathcal{H}(u), \quad (12)$$

which may be evolved using a time-splitting scheme

$$\begin{aligned} u^* &= u^n - \mathcal{F}(u)\Delta t + O(\Delta t^2) \\ u^{n+1} &= u^* - \chi \mathcal{H}(u^*)\Delta t + O(\Delta t^2) \end{aligned} \quad (13)$$

Taking the parameter  $\chi = 1/\Delta t$  and  $\mathcal{H} = (\mathcal{I} - \mathcal{G})$  to be the corresponding high-pass filter of  $\mathcal{G}$ , and substituting in equation 13 one obtains:

$$u^{n+1} = \mathcal{G}(u^*) + O(\Delta t^2) \quad (14)$$

which is equivalent to the expression obtained in equation 11 to leading order of time discretization. The relaxation-term may be interpreted as the equivalent to a low-pass filter operation  $\mathcal{G}$  every  $1/(\chi\Delta t)$  time-steps (Stolz *et al.* 2001; Mathew *et al.* 2003; Schlatter *et al.* 2004) or the application of the filter  $\mathcal{G}$  with the strength  $\chi\Delta t$  every time-step Mathew *et al.* (2003).

Thus the “filter-based stabilization” operation proposed by Fischer & Mullen (2001) may be reformulated as an equivalent “relaxation-term-based stabilization”, which we refer to as “RT stabilization”. It can be easily incorporated into the Navier-Stokes by a simple addition of a relaxation-term on the right hand side. Thus the equivalent RT stabilized equation may be written as (Schlatter *et al.* 2004)

$$\frac{\partial u}{\partial t} + u \cdot \nabla u = -\frac{\nabla p}{\rho} + \nu \nabla^2 u - \chi \mathcal{H}(u), \quad (15)$$

$$\nabla \cdot u = 0. \quad (16)$$

Here  $\mathcal{H}(u)$  is a high-pass-filtered velocity field. The parameter  $\chi$  may be used as a weighting parameter similar to the filter weight ‘ $\alpha$ ’ used in Fischer & Mullen (2001) and Malm *et al.* (2013). Such a formulation immediately provides us with

two advantages over the explicit filtering operation. Firstly, since there are no more explicit filtering operations after the pressure-correction step, the velocity field remains divergence free. Secondly, with the RT now part of the evolution equations, for a fixed  $\chi$  and  $\mathcal{H}$  the physical energy drain provided by the RT should be independent of the chosen time-step (as long as numerical stability is ensured). The final aspect of the stabilization concerning the dissipative character of the RT requires more constraints. For scalar transport equations  $\mathcal{H}$  may be chosen to be positive semi-definite, and  $\chi$  a positive constant. In such a scenario the RT is purely dissipative in nature. However with spatially varying  $\chi$  and  $\mathcal{H}$  the relaxation-term may be non-dissipative (Stolz & Adams 2003).

### 3.1. RT parameters

In the context of spectral-elements Malm *et al.* (2013) describe a simple transfer function  $\mathcal{G}$  defined for a variable in a one-dimensional domain  $\Omega = [-1, 1]$  such that the filtering operation takes the simple form

$$\bar{u}_N(x) = \mathcal{G}(u_N(x)) = \sum_{k=0}^N \sigma_k a_k \phi_k(x), \quad (17)$$

where  $\phi_k$  is the basis function and the definition of  $\sigma_k$  describes the low-pass filter function  $\mathcal{G}$  which takes the form

$$\sigma_k = \begin{cases} 1 - \alpha \left( \frac{k-k_c}{N-k_c} \right)^2, & k > k_c \\ 1, & k \leq k_c. \end{cases} \quad (18)$$

Where  $N$  is the number of modes in the spectral-element discretization and  $k_c$  is the cut-off mode in spectral space used for building the filter. Amplitudes for modes  $k \leq k_c$  are unaffected by the filter operation.  $\alpha$  is the filter weight such that  $0 \leq \alpha \leq 1$ . In keeping with our analysis earlier, we may define the corresponding high-pass filter  $\mathcal{H}$  for the RT as:

$$\mathcal{H}(u_N(x)) = \sum_{k=0}^N \gamma_k a_k \phi_k(x) \quad (19)$$

$$\gamma_k = \begin{cases} \left( \frac{k-k_c}{N-k_c} \right)^2, & k > k_c, \\ 0, & k \leq k_c \end{cases} \quad (20)$$

where the parameter  $\alpha$  is absorbed into  $\chi$  which acts as an RT strength term. To formally have the same operation as the explicit filter, the value of  $\chi$  can be set to  $\chi = (\alpha/\Delta t)$ . This is in agreement with the interpretation that the RT procedure is equivalent to performing a low-pass filter operation every time-step with a strength of  $(\chi\Delta t)$ . Using this value we get  $\chi\Delta t = \alpha$  and thus we recover the correct weighting for the equivalent explicit filter operation.

The basis functions  $\phi$  used for the definition of  $\mathcal{H}$  however is different from the one used by Malm *et al.* (2013) who use the transformed basis functions described by Boyd (1998) which are described in equation 2. Using this basis

function however, the form of  $\mathcal{H}$  is not semi-positive definite and thus the relaxation term is not purely dissipative. This is rather expected from our earlier results which show that the explicit filter operation using such a transformed basis has a substantial parameter range where it acts as an energy source. The equivalent RT formulation then can not be purely dissipative. We use the Legendre polynomials as the basis functions (for a Legendre-spectral-element method) for building the RT which makes  $\mathcal{H}$  semi-positive definite. Thus for  $\chi > 0$  the relaxation term  $-\chi\mathcal{H}(u)$  is purely dissipative in a scalar transport equation.

### 3.2. Stability and parameter range

The action of the RT can be inferred from the change in eigenvalues of the system due to the added stabilization. As an illustration we build the system matrices using the simple  $3 \times 3$  spectral-element grid in Matlab for a linear advection operator stabilized by a relaxation-term. The advection operator is built using the parameters in equation 9. We set  $\epsilon = 10^{-2}$  so that the operator now models a numerically unstable system with positive eigenvalues. The eigenvalues of the unstable system without the addition of a relaxation term are shown in figure 8a. As expected, there are unstable eigenvalues with positive real part of order  $O(10^{-2})$ . With the addition of an RT as defined earlier, with  $k_c = 10$  and  $\chi = 0.4$  causes the eigenvalues to shift towards the negative real plane (figure 8b). In the example shown here, the instability appears to be completely suppressed and the largest real part of the eigenvalues of the resulting system is zero. The overall system is more dissipative as evidenced by the general negative shift of the real part of the eigenvalues. A stabilization of eigenvalues has also been shown by Ohlsson *et al.* (2011) for the explicit filtering operation in the Burgers' equation.

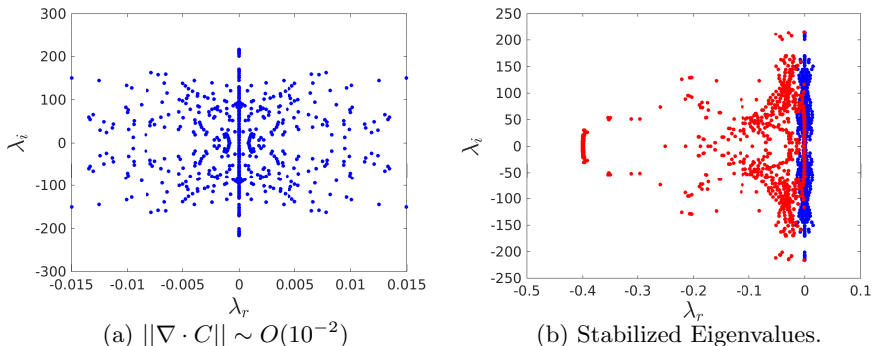


Figure 8: Comparison of eigenvalues for an unstable system (a) with  $\|\nabla \cdot C\| \sim O(10^{-2})$  and a system stabilized using a relaxation-term (b)

While the RT clearly has a stabilizing effect on the system, it can also be destabilizing for a certain range of parameters. From figure 8b one can notice some eigenvalues of the stabilized system have a large negative shift with the smallest real part being  $\lambda_r^{min} = -0.4$ . As it turns out this particular eigenvalue sets the stability limits of the RT stabilization approach. For a particular temporal discretization such as the BDF-EXT-3, the region of stability may cover a finite region of the negative plane. For a system with eigenvalues such that  $\lambda\Delta t$  falls outside the stability region of the time-stepping scheme, the system becomes numerically unstable. The scaled eigenvalues with varying values of the parameter  $\chi\Delta t$  (and  $k_c = 10$ ) are shown in figure 9 with a black line enveloping the region of stability for a BDF-EXT-3 temporal discretization scheme. As the strength of the RT stabilization is increased by varying  $\chi$ , the eigenvalues become more negative and the dissipative character of the stabilization procedure becomes stronger. Eventually as  $\chi\Delta \approx 1$  the stabilization procedure itself becomes numerically unstable and the time-step needs to be reduced in order to render the simulation numerically stable again. The analysis is exemplified using the BDF-EXT-3 scheme but the concept generalizes to other schemes and the limit of stability will be governed by the stability region of the respective schemes. The same conclusion may also be drawn by analyzing a scalar transport equation with a time-splitting scheme and applying the numerical stability arguments to the relaxation step. Schlatter (2005) mentions a similar numerical stability criterion for  $0 < \chi < 1/\Delta t$ . This condition limits the parameter range for which a relaxation-term type stabilization can be used. Practical values of the  $\chi$  parameter should not reach such a limit. To compare with an explicit filtering case, practical values of the filter strength vary between  $0 \leq \alpha \leq 0.3$  which correspond to  $0 \leq \chi\Delta t \leq 0.3$ . Fischer & Mullen (2001) apply the filtering procedure with  $\alpha = 1.0$  and note that lower values of  $\alpha$  are preferable. Should one find that the dissipation provided at low values of  $\chi$  is not enough, the alternative would be to change the cut-off wavenumber  $k_c$ . This increases the added dissipation by the relaxation-term but does not substantially change the stability limits. Figure 10 shows the change in eigenvalues with different  $\chi\Delta t$  using the cut-off mode number as  $k_c = 8$ . The system is clearly more dissipative with many more eigenvalues with large negative real parts. However the approach to numerical instability remains approximately the same at  $\chi\Delta t \approx 1.0$ .

It is important to note that such a formulation is very similar to the RT-3D approach used by Schlatter *et al.* (2004) in the context of large-eddy simulations of transitional flows. In the study the authors compare different variants of the ADM-RT (approximate deconvolution model with relaxation term) for transitional and turbulent regimes. In the RT-3D variant the non-linear terms are computed without the deconvolution procedure and hence only the relaxation-term is used for modeling the sub-grid stresses. A comparison of the LES performance between the explicit filtering technique and relaxation-term is also performed in Schlatter *et al.* (2006a). In the current study we are

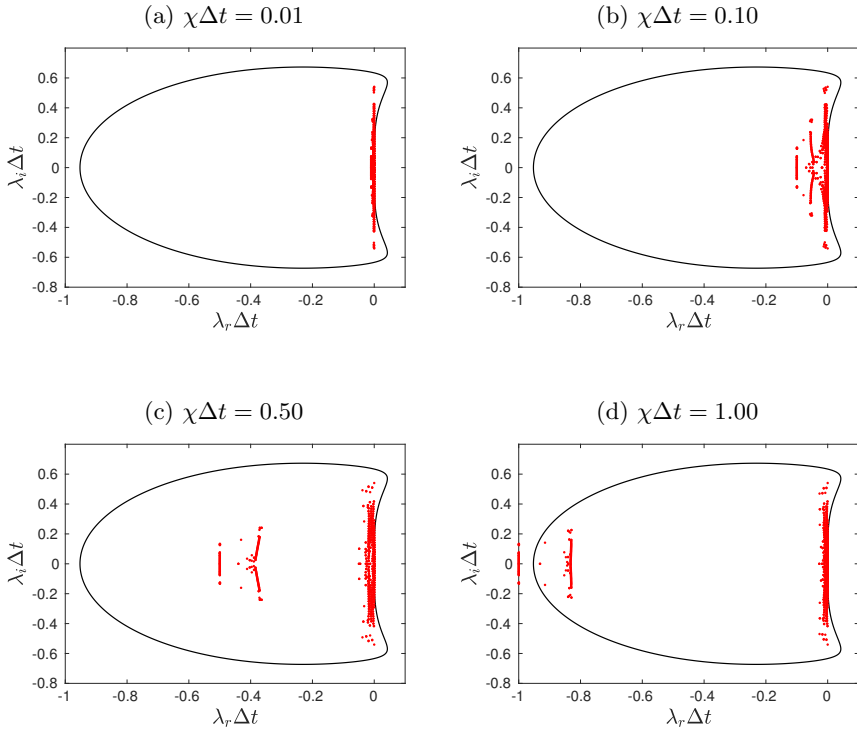


Figure 9: Changes in eigenvalues with varying filter strength  $\chi\Delta t$  with  $k_c = 10$ .

only concerned with the relaxation-term procedure in the context of numerical stabilization.

### 3.3. Double shear layer

We test the RT stabilization in the 2D model test case of double shear layer as done by Fischer & Mullen (2001) and Malm *et al.* (2013) for a several different parameters. Quite expectedly the procedure successfully stabilizes the simulations. We show the results of only one test case when no over-integration is employed, which would be the most stringent test case for stabilization. We ran the test using a  $16 \times 16$  spectral-element grid with  $N = 16$  Legendre modes in each spectral-element. The RT parameters of  $\chi = 1.5 \times 10^{+3}$  (corresponding to  $\chi\Delta t = 0.3$ ) and  $k_c = 15$  were used. Figure 11 shows the vorticity in the field at  $T = 2.0$  where the thin shear layers are clearly visible. The simulation ran without numerical instabilities up to  $T = 20$ .

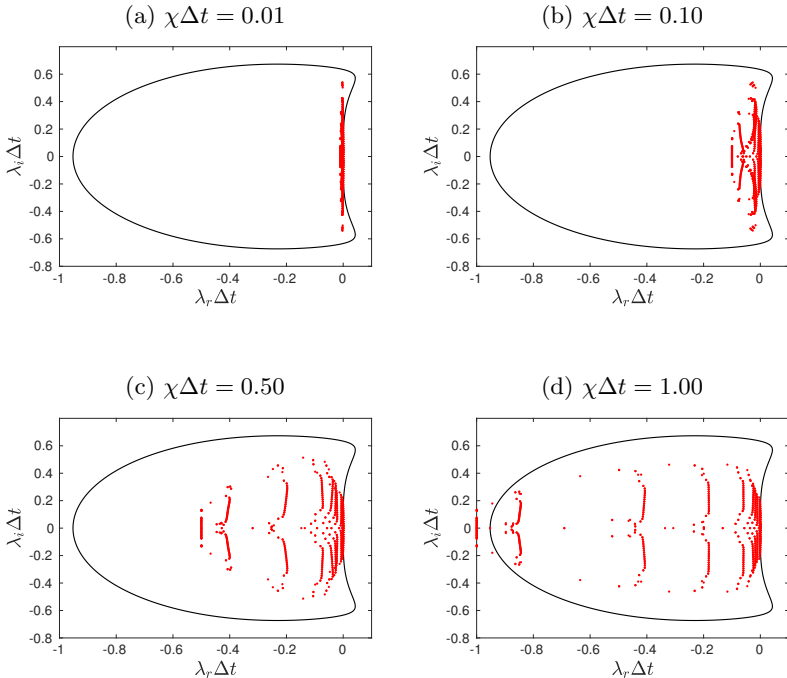


Figure 10: Changes in eigenvalues with varying filter strength  $\chi\Delta t$  with  $k_c = 8$ .

#### 4. Conclusion

We reassess the filter-based stabilization proposed by Fischer & Mullen (2001) and find that despite its appealing simplicity and efficiency, it suffers from a few drawbacks, the most striking of which is the loss of the divergence-free quality of the flow field due to commutation errors. In marginally resolved simulations, this loss may be severe as in our model test case where 6 orders of accuracy was lost for the divergence-free condition. Two other drawbacks are the time-step dependence of the filtered energy and the statistical character of the filter dissipation. A closely related alternate formulation for the explicit filtering involves a relaxation regularization referred to as “relaxation-term-based stabilization” or RT stabilization. With appropriate parameters it can be shown to be equivalent to an explicit filter operation to leading order of time discretization. The procedure stabilizes the numerical method without destroying the divergence-free property. Moreover, the stabilization is now part of the evolution equations, and thus the energy drain due to relaxation-term is independent of the chosen time-step. Limits of the stabilization are also shown and under certain parameters the stabilization itself becomes numerically

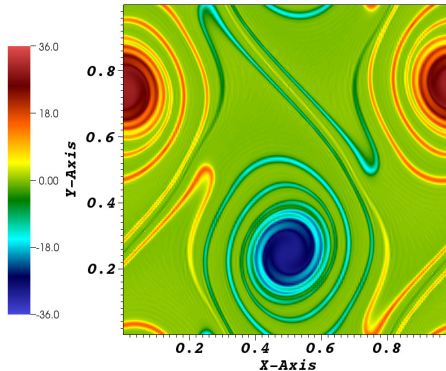


Figure 11: Vorticity at  $t = 2.0$  for the double shear layer case using polynomial order  $N = 16$  without over-integration and using a relaxation-term stabilization.

unstable. However the procedure is stable under the standard parameter ranges which may be expected for numerical stabilization. Test cases with the double shear layer shows the relaxation-term is able to stabilize the numerical simulation even in the absence of over-integration, which corresponds to a fairly stringent case of numerical stability in the presence of negligible viscosity.

## REFERENCES

- BOYD, J. P. 1998 Two comments on filtering (artificial viscosity) for chebyshev and legendre spectral and spectral element methods: Preserving boundary conditions and interpretation of the filter as a diffusion. *Journal of Computational Physics* **143** (1), 283 – 288.
- CANUTO, C., QUARTERONI, A., HUSSAINI, M. Y. & ZANG, T. A. 1988 *Spectral Methods in Fluid Dynamics*. Springer.
- CHOW, F. K. & MOIN, P. 2003 A further study of numerical errors in large-eddy simulations. *Journal of Computational Physics* **184** (2), 366 – 380.
- DOMARADZKI, J. A. & ADAMS, N. A. 2002 Direct modelling of subgrid scales of turbulence in large eddy simulations. *Journal of Turbulence* **3**, N24.
- ERVIN, V. J., LAYTON, W. J. & NEDA, M. 2012 Numerical analysis of filter-based stabilization for evolution equations. *SIAM Journal on Numerical Analysis* **50** (5), 2307–2335.
- FISCHER, P. & MULLEN, J. 2001 Filter-based stabilization of spectral element methods. *Comptes Rendus de l'Académie des Sciences - Series I - Mathematics* **332** (3), 265 – 270.
- GEURTS, B., VREMAN, B., KUERTEN, H. & VAN BUUREN, R. 1997 *Noncommuting Filters and Dynamic Modelling for Les of Turbulent Compressible Flow in 3D Shear Layers*, pp. 47–56. Dordrecht: Springer Netherlands.
- GEURTS, B. J. & HOLM, D. D. 2006 Commutator errors in large-eddy simulation. *Journal of Physics A: Mathematical and General* **39** (9), 2213.

- KARAMANOS, G.-S. & KARNIADAKIS, G. 2000 A spectral vanishing viscosity method for large-eddy simulations. *Journal of Computational Physics* **163** (1), 22 – 50.
- KIRBY, R. M. & KARNIADAKIS, G. E. 2003 De-aliasing on non-uniform grids: algorithms and applications. *Journal of Computational Physics* **191** (1), 249 – 264.
- KIRBY, R. M. & SHERWIN, S. J. 2006 Stabilisation of spectral/hp element methods through spectral vanishing viscosity: Application to fluid mechanics modelling. *Computer Methods in Applied Mechanics and Engineering* **195** (23), 3128 – 3144, incompressible CFD.
- KRIST, S. E. & ZANG, T. A. 1987 Numerical simulation of channel flow transition, resolution requirements and structure of the hairpin vortex. *Tech. Rep.*. NASA Langley Research Center; Hampton, VA, United States.
- MADAY, Y., KABER, S. M. O. & TADMOR, E. 1993 Legendre pseudospectral viscosity method for nonlinear conservation laws. *SIAM J. Numer. Anal* **30**, 321–342.
- MALM, J., SCHLATTER, P., FISCHER, P. F. & HENNINGSON, D. S. 2013 Stabilization of the spectral element method in convection dominated flows by recovery of skew-symmetry. *Journal of Scientific Computing* **57** (2), 254–277.
- MATHEW, J., LECHNER, R., FOYSI, H., SESTERHENN, J. & FRIEDRICH, R. 2003 An explicit filtering method for large eddy simulation of compressible flows. *Physics of Fluids* **15** (8), 2279–2289.
- OHLSSON, J., SCHLATTER, P., FISCHER, P. F. & HENNINGSON, D. S. 2011 *Stabilization of the Spectral-Element Method in Turbulent Flow Simulations*, pp. 449–458. Berlin, Heidelberg: Springer Berlin Heidelberg.
- ORSZAG, S. A. 1971 On the Elimination of Aliasing in Finite-Difference Schemes by Filtering High-Wavenumber Components. *Journal of the Atmospheric Sciences* **28** (6), 1074–1074.
- PASQUETTI, R. & XU, C. 2002 Comments on filter-based stabilization of spectral element methods. *Journal of Computational Physics* **182** (2), 646 – 650.
- PHILLIPS, N. A. 1959 An example of non-linear computational instability. *The Atmosphere and the Sea in motion* **501**.
- SCHLATTER, P., STOLZ, S. & KLEISER, L. 2004 LES of transitional flows using the approximate deconvolution model. *International Journal of Heat and Fluid Flow* **25** (3), 549 – 558, turbulence and Shear Flow Phenomena (TSFP-3).
- SCHLATTER, P., STOLZ, S. & KLEISER, L. 2006 *Analysis of the SGS energy budget for deconvolution- and relaxation-based models in channel flow*, pp. 135–142. Dordrecht: Springer Netherlands.
- SCHLATTER, P. C. 2005 Large-eddy simulation of transition and turbulence in wall-bounded shear flow. Doctoral thesis, Swiss Federal Institute of Technology Zürich.
- STOLZ, S. & ADAMS, N. A. 2003 Large-eddy simulation of high-reynolds-number supersonic boundary layers using the approximate deconvolution model and a rescaling and recycling technique. *Physics of Fluids* **15** (8), 2398–2412.
- STOLZ, S., ADAMS, N. A. & KLEISER, L. 2001 An approximate deconvolution model for large-eddy simulation with application to incompressible wall-bounded flows. *Physics of Fluids* **13** (4), 997–1015.
- TADMOR, E. 1989 Convergence of spectral methods for nonlinear conservation laws. *SIAM Journal on Numerical Analysis* **26** (1), 30–44.

- VAN DER BOS, F. & GEURTS, B. J. 2005 Commutator errors in the filtering approach to large-eddy simulation. *Physics of Fluids* **17** (3), 035108.
- VASILEV, O. V., LUND, T. S. & MOIN, P. 1998 A General Class of Commutative Filters for LES in Complex Geometries. *Journal of Computational Physics* **146** (1), 82 – 104.
- VON NEUMANN, J. & RICHTMYER, R. D. 1950 A method for the numerical calculation of hydrodynamic shocks. *Journal of Applied Physics* **21** (3), 232–237.



**2**

**Paper 2**



# Dynamic response of natural laminar flow airfoils

P. S. Negi , A. Hanifi and D. S. Henningson

Department of Mechanics, Linné FLOW Centre and Swedish e-Science Research Centre (SeRC), KTH Royal Institute of Technology, SE-100 44 Stockholm, Sweden

*Technical Report*

Large-eddy simulations are performed to investigate the dynamic response of a natural laminar flow airfoil undergoing harmonic pitch oscillations at a chord based Reynolds number of  $Re_c = 750,000$ . Large changes in the transition location are observed throughout the pitch cycles which leads to a non-linear response of the aerodynamic force coefficients. Preliminary results show that the evolution of the boundary layer over the airfoil can be modeled by using a simple phase-lag concept which implies that the boundary-layer evolution is quasi-steady in nature. A simple empirical model is developed based on this quasi-steady, phase-lag assumption which fits very well with the measured experimental data.

**Key words:** unsteady aerodynamics, natural laminar flow, empirical model

---

## 1. Introduction

The foundations of unsteady aerodynamics of two-dimensional airfoils were laid down in the 1930s (Leishman 2000), with the works of Glauert (1930), Theodorsen (1935) and Karman & Sears (1938) providing much of the early mathematical basis for understanding unsteady, attached, incompressible flows. Experimental corroboration was provided by Halfman (1952), who performed experiments on subsonic airfoils oscillating in pitch and translation motions and found a good agreement between the experimental data and theoretical predictions of Theodorsen (1935). Lomax *et al.* (1952) and Lomax (1954) provided the basis for the development of linearized unsteady aerodynamic models for compressible flows. An overview of these unsteady theories can be found in Leishman (2000) and for a more comprehensive account one may refer to Bisplinghoff *et al.* (1983). The underlying feature of the classical theories has been an assumption of linearity, resulting in mathematically elegant and computationally simple expressions for the unsteady aerodynamic forces (Leishman 2000). A feature which is found highly attractive by design engineers. With the emerging challenges of global warming, focus of the aerodynamic community has turned towards laminar flow wing technology (Green 2008), which has

brought forward the questions of aeroelastic behavior of natural laminar flow (NLF) airfoils. As recently as 2011, aeroelastic studies focusing on laminar airfoils were virtually non-existent, with Mai & Hebler (2011) noting that “no systematic aeroelastic investigation has been performed for natural laminar flow airfoils”. The first studies to remedy this situation were performed by Mai & Hebler (2011) and Hebler *et al.* (2013), whose experiments on the aeroelasticity of laminar wings in the transonic regime have shown a non-linear behavior of the aerodynamic forces for a simple harmonic pitch oscillation. The cause of such behavior was related to the free movement of transition on the suction side of the wing surface. When the authors fixed the transition on the wing surface by introducing a trip near the leading edge, the non-linearities became negligible. In the experiments of Mai & Hebler (2011), the non-linearities were not confined to the transonic regime but were also observed for the subsonic case. These works inspired the studies of Lokatt (2017) who performed experiments on harmonic pitching of a laminar airfoil in the subsonic regime. The author also found strongly non-linear behavior of the normal force coefficient ( $C_z(t)$ ) for small-amplitude pitch oscillations. The strength of the non-linearity was determined by the departure of the measured time-dependent  $C_z(t)$  from a purely harmonic response. Again, when the authors fixed the transition near the leading edge, the non-linearities seem to disappear. Interestingly, the non-linearities emerged only for a certain range of angles of attack  $\alpha$ . When static experiments were performed in the same  $\alpha$  range, the slope  $\partial C_z / \partial \alpha$  also showed a strong departure from the linear behavior expected from thin-airfoil theory. The emergence of these non-linearities clearly indicates that the classical theories are no longer appropriate to describe the unsteady behavior for natural laminar flow airfoils. Since these pioneering aeroelasticity studies point to the free movement of transition as one of the factors responsible for such behavior, the spatially developing boundary layers clearly play a dominant role in the unsteady dynamics. In the classical theories, the role of the boundary layer over the airfoil is virtually neglected by invoking the inviscid assumption (along with the Kutta condition). While the early experiments of Halfman (1952) show that this may be a valid assumption, evidently it is no longer appropriate for unsteady laminar airfoils.

The current work investigates the unsteady aerodynamic response of a natural laminar airfoil, at a chord-based Reynolds number of  $Re_c = 750,000$ . The airfoil used in the investigation is the ED36F128 (Lokatt & Eller 2017; Lokatt 2017) with a  $13.8^\circ$  flap deflection. The same airfoil was used by Lokatt (2017) for her aeroelasticity experiments. This report documents the initial results of the ongoing investigation. The remainder of the report is structured as follows. In section 2 we present a hypothetical argument that connects the temporal non-linearities of aerodynamic force coefficients observed in unsteady airfoils with the non-linearity of the static aerodynamic coefficients (with respect to  $\alpha$ ). Section 3 describes the computational setup and some of the results of the numerical simulations obtained with a stationary airfoil which form the basis of parameter selection for the unsteady case. Section 4 presents the initial

results for the unsteady case and in section 5 we use the insight gained from the initial unsteady results to build an empirical model to explain some of the unsteady experimental data obtained by Lokatt (2017). The summary and conclusions are presented in section 6.

## 2. A quasi-steady case

We present a hypothetical case of an airfoil undergoing small-amplitude pitch oscillations with a vanishingly-small reduced frequency  $k$ . The reduced frequency is defined as  $k = \omega b/U_\infty$ , where  $\omega$  is angular frequency of pitch oscillations,  $b$  is the semi-chord length, and  $U_\infty$  is the free stream velocity. The relation for the instantaneous angle of attack of the airfoil can be described as:

$$\alpha(t) = \alpha_0 + \Delta\alpha \sin(\omega t). \quad (1)$$

Here  $\alpha_0$  is the mean angle of attack and  $\Delta\alpha$  is the amplitude of pitch oscillations. When the frequency of oscillation is extremely small, *i.e.*  $k \lll 1$ , the time-dependent coefficient of normal force  $C_z(t)$  would simply be equal to the static value throughout the pitch cycle, *i.e.*

$$C_z(t) \approx C_z^s(\alpha(t)). \quad (2)$$

Where  $C_z^s(\alpha)$  is the value of the normal force coefficient evaluated at the static angle of attack of  $\alpha$ . To exemplify, we consider the static normal force coefficients for the ED36F128 airfoil, obtained using an integral boundary layer code, XFOIL (Drela 1989). Figure 1 shows the static  $C_z$  curve which is approximately linearly increasing for  $0 < \alpha < 2.7^\circ$ . It exhibits a region of strong non-linearity and non-monotonic behavior for  $2.7^\circ < \alpha < 4.6^\circ$ , after which it is approximately linear again. Consider a quasi-steady response of an oscillation at a mean angle

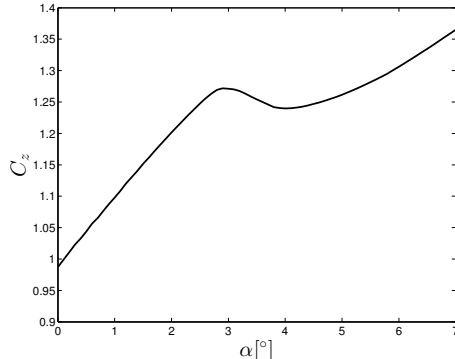


Figure 1: The static normal force coefficient for different angles of attack at  $Re_c = 10^6$ .

of attack of  $\alpha_0 = 1.5^\circ$ , pitch amplitude of  $\Delta\alpha = 1.0^\circ$  and a very small reduced frequency ( $k = 0.0001$  for example). The instantaneous angle of attack is then given by equation 1 and the time-dependent response can be constructed using

equation 2. The thick red line in figure 2a shows the region covered by the quasi-steady variation of angle of attack and figure 2b shows the quasi-steady response ( $T_{osc}$  is the time period of oscillation). When the harmonic oscillations occur within the linear regime, the time response will be linear in the frequency domain, and a pure harmonic of a single frequency is obtained. On the other

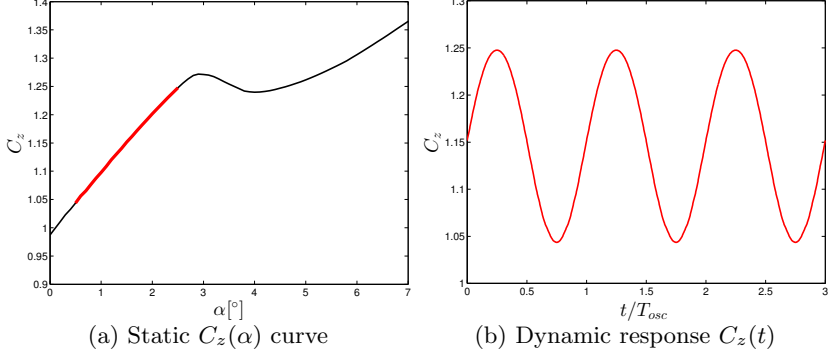


Figure 2: Quasi-steady response of  $C_z$  in the linear region ( $0.5 < \alpha < 2.5$ ).

hand, the same procedure may be followed such that the quasi-steady oscillation occurs in the non-linear regime with  $\alpha_0 = 2.7^\circ$ , as shown by the thick red line in figure 3a. Clearly the quasi-steady response is no longer linear in the frequency domain and multiple frequencies are obtained in the quasi-steady response. While this may be a hypothetical case, it is reasonable to expect that

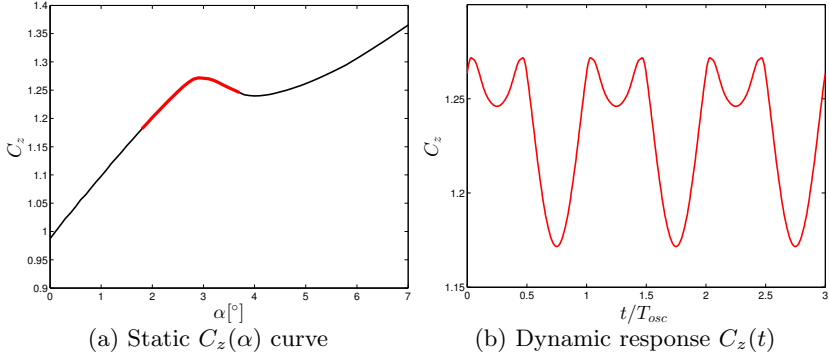


Figure 3: Quasi-steady response of  $C_z$  in the non-linear region ( $1.7 < \alpha < 3.7$ ).

for a small enough value of  $k$ , and in the absence of hysteresis there would be no perceptible dynamic effects and the flow would adjust to the slowly varying instantaneous angle of attack. As the value of  $k$  is increased and unsteady

effects become important, the dynamic response would slowly depart from this quasi-steady response. The simple example suggests that the classical linearized unsteady aerodynamic models, such as the one proposed by Theodorsen (1935), are no longer applicable even in the simplest quasi-steady conditions when inherent non-linearities exist in the static case. Unsteady aerodynamic models which account for this non-linearity of the static aerodynamic coefficients are necessary to accurately describe the unsteady response in such conditions.

### 3. Stationary airfoil simulations

#### 3.1. Parameter identification

In order to study the dynamic response of unsteady natural laminar flow airfoils, it is necessary to establish the flow conditions for representative static angles of attack. However the high Reynolds numbers of the flow case make it prohibitively expensive to simulate several flow cases at different (static) angles of attack. To reduce the computational cost and narrow down the parameter range, we make use of experimental data provided by Lokatt (2017) and also perform calculations using XFOIL. Two factors govern the final choice of parameter selection for the unsteady simulations.

- Firstly, the earlier studies indicate that the dynamic non-linearities are observed when there is a free movement of transition on the suction side of the airfoil (Mai & Hebler 2011; Hebler *et al.* 2013; Lokatt 2017). Thus the parameter range must have large variations in transition location.
- Secondly, in the previous section we established the link between the non-linearities in the temporal and static responses. Thus we also look for the  $\alpha$  range that shows the strongest non-linearities in the static response of the lift coefficient.

The static response curves for the airfoil obtained using XFOIL as well the experimental data from Lokatt (2017) are shown in figure 4a. While the experimental data and XFOIL calculations differ in magnitude, the range of angle of attack where qualitative changes take place is the same. In both cases the static response curve is linear between  $1^\circ < \alpha < 3^\circ$  and at around  $\alpha = 3.4^\circ$  the static curves strongly depart from their linear behavior, with the lift coefficient decreasing with increasing  $\alpha$ . Figure 4b shows the variation of transition location on the suction side of the airfoil as predicted by XFOIL. Within the same range where non-linearities are observed in the static lift coefficient ( $\alpha > 3.4^\circ$ ), there is a sharp change in the slope of the transition location curve. Between  $1^\circ < \alpha < 3^\circ$  the transition location has a very slow upstream movement, while for  $\alpha > 3.4^\circ$ , the upstream movement is much more rapid with respect to angle of attack. Both governing factors mentioned earlier indicate the same angle of attack region where non-linearities are to be expected (*i.e.*  $\alpha \approx 3.4^\circ$ ). Thus the pitching range where non-linearities are expected to show up strongly is near  $\alpha \approx 3.4^\circ$ . Therefore this is defined as the mean angle of attack of oscillation. The pitch amplitude is taken to be small in accordance

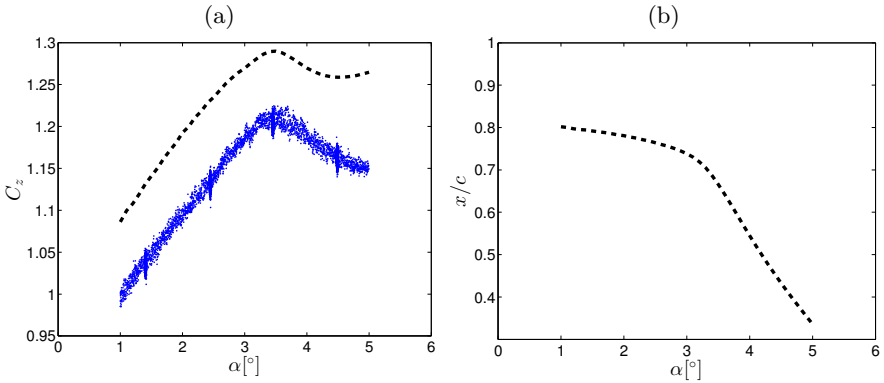


Figure 4: Static aerodynamic characteristics of the NLF airfoil obtained from XFOIL calculations. Normal force coefficient (left) and transition location (right) variation with  $\alpha$ .

with the experimental results of Lokatt (2017). The pitching motion of the unsteady case may be described by equation 3:

$$\alpha(t) = \alpha_0 + \Delta\alpha \sin(\Omega(t - t_0) + \phi_0). \quad (3)$$

where  $\alpha_0 = 3.4^\circ$  is the mean angle of attack,  $\Delta\alpha = 1.0^\circ$  is the pitch amplitude,  $\Omega$  is the angular frequency of oscillation,  $t$  represents the simulation time,  $t_0$  is the starting time of the pitching motion and  $\phi_0$  is the initial phase at the start of the oscillations.

In order to verify the static characteristics observed in experiments and also predicted by XFOIL, simulations of stationary airfoils are performed in the range chosen above to ensure that the expected variation of transition location is captured by the numerical simulations.

### 3.2. Computational Setup

The numerical simulations are set up to perform wall-resolved large-eddy simulations (LESs) of the stationary and pitching airfoils. All numerical simulations are carried out using Nek5000 (Fischer *et al.* 2008). The setup is done in a manner very similar to our previous works relating to simulations of flow around airfoils (Hosseini *et al.* 2016; Vinuesa *et al.* 2017; Negi *et al.* 2017). The spectral-element mesh is generated using ANSYS® ICEMCFD, which is structured and orthogonal near the airfoil surface. The numerical simulation is set up such that the final resolution utilizes an 11<sup>th</sup> order polynomial representation for the velocity and a staggered 9<sup>th</sup> order representation for the pressure. The Navier-Stokes equations are solved using the Arbitrary-Lagrangian-Eulerian (ALE) framework (Ho & Patera 1990, 1991) to account for the motion of boundary and the internal points. The coordinate system is defined such that the  $x$  direction

is aligned with the inflow direction,  $z$  is the spanwise homogeneous direction and  $y$  is normal to the airfoil plane. All length scales are normalized by the chord length  $c$ , and velocities are normalized by the free-stream velocity,  $U_\infty$ . The far field boundaries are two chords away from the airfoil leading edge in either direction and the outflow boundary is four chords downstream from the airfoil leading edge. The inlet is designed as a curved inflow boundary with a constant radial distance of two chords from the leading edge of the airfoil. The spanwise width of the computational domain is  $l_z = 0.15c$ . Periodic boundary conditions are imposed on the spanwise boundaries, while the energy-stabilized outflow condition (Dong *et al.* 2014) is imposed on the outflow boundary. A URANS simulation is performed using the transition  $k-\Omega$  SST model (Langtry & Menter 2009) for the same case with far-field and outflow boundaries set at a 100 chords distance. Time-averaged velocity field data from the URANS simulation is extracted for the locations corresponding to the domain boundaries of the LES simulation. This extracted data is imposed as a Dirichlet boundary condition on the inlet and far-field boundaries. In order to simulate low turbulence flight conditions, free-stream turbulence of intensity  $Ti = 0.1\%$  is superimposed on the Dirichlet boundary conditions. The free-stream turbulence is generated using Fourier modes with a von Kármán spectrum. The integral length scale of the spectrum is set to  $l = 0.01$  which is approximately 5-10 times the boundary layer height near the leading edge. The procedure is similar to the one described in Schlatter (2001); Brandt *et al.* (2004); Schlatter *et al.* (2008), where it has been used for the study of by-pass transition in flat-plate boundary layers. It has also been used for wind turbine simulations (Kleusberg 2017) and in our earlier work on pitching airfoils at  $Re_c = 100,000$  (Negi *et al.* 2017).

The grid resolution on the airfoil surface varies with the chord-wise location in accordance with the changing boundary layer characteristics. Thus the guidelines for grid design use the following criteria:

- For  $0.1 < x/c < 0.6$ ,  $\Delta x^+ = 18$ ,  $\Delta y_{wall}^+ = 0.64$  and  $\Delta y_{max}^+ = 11$ , on the suction side and use the local wall-shear ( $\tau_w$ ) values on the airfoil. Since the flow is expected to be laminar on the pressure side, the stream-wise resolution is slightly relaxed to  $\Delta x^+ = 25$  while keeping the same wall-normal resolution.
- For  $x/c < 0.1$ , the peak  $\tau_w$  value over the suction side of the airfoil is used to estimate the grid spacing for both the suction and pressure sides.
- for  $x/c > 0.6$ , the suction side experiences a large adverse pressure gradient which significantly reduces  $\tau_w$  values. Therefore, the  $\tau_w$  values from the pressure side are used for both the suction and pressure sides.
- A structured mesh is used, which is extruded in the span-wise direction. Hence the spanwise resolution is constant throughout the domain. The resolution is set to  $\Delta z^+ = 12$ , where the the peak  $\tau_w$  value from the suction side is used.

The symbol  $^+$  indicates normalization with inner units using kinematic viscosity  $\nu$ , and local friction velocity  $u^*$ . Wall-shear stress data is obtained using XFOIL

to estimate the local friction velocity. A trip is introduced in XFOIL at  $x/c \approx 0.1$  to obtain turbulent wall-shear values on both the suction and pressure sides of the airfoil. A different criterion is needed for defining the resolution in the wake where the wall-based criteria are not valid. Accordingly, the URANS data is used to estimate the Kolmogorov length scale ( $\eta$ ) in the wake region. The grid in the wake region is designed such that the average grid spacing in the near wake ( $1 < x/c < 2$ ) follows the criteria:  $\Delta x/\eta < 9$ . For  $x/c > 2$  the grid spacing in the wake is slowly increased such that  $\Delta x/\eta \approx 20$  near the outflow boundary at  $x/c = 4$ .

Note that the above guidelines are for the final resolution of the numerical simulation. In our methodology we simulate the initial transients with a lower order polynomial representation on the same spectral-element grid and slowly increase the polynomial order. Currently, only the results from the low order polynomial simulations (5<sup>th</sup> order for the velocity) are reported. The effective grid spacings for the current results is therefore twice the values reported above. Nonetheless, tests with stationary airfoil simulations indicate that the qualitative features of the flow do not change with changing polynomial orders.

### 3.3. Stationary simulation results

In accordance with the angle of attack range selected earlier, we perform two simulations with a stationary airfoil, with angles of attack corresponding to the two extremities of the pitching cycle, *i.e.* at  $\alpha = 2.4^\circ$  and  $\alpha = 4.4^\circ$ . Figure 5 shows the instantaneous vortical structures identified by the  $\lambda_2$  criterion (Jeong & Hussain 1995). From the figures it is clear that the transition occurs at widely different chord-wise locations for the two angles of attack, which is in accordance with the predictions of XFOIL as seen earlier in figure 4b. The instantaneous structures for both cases are extracted after running the two simulations for about 6 flow through times. After the initial transients are convected away, the overall qualitative state of the flow does not change and the transition location remains constant. To ensure that the low order of the simulations is not affecting the transition location, and thus the overall qualitative flow state, the simulation with the lower angle of attack ( $\alpha = 2.4^\circ$ ) is restarted with a higher polynomial order ( $N = 8$ ) and the simulation is continued for about 1 flow over time. No qualitative change is detected in the flow state and the transition location does not change.

## 4. Unsteady results

### 4.1. Lift coefficient

Once the flow state for the stationary airfoil cases is established, oscillations of a pitching airfoil are performed with the pitching motion prescribed by equation 1. The angular frequency ( $\Omega$ ) of the oscillation is chosen such that the non-dimensional reduced frequency,  $k = 0.4$  and the pitch axis is located at  $(x_0, y_0) = (0.35, 0.034)$ . The time period of oscillation ( $T_{osc}$ ) for the chosen reduced frequency is equal to 7.85. The pitching simulations are started from the

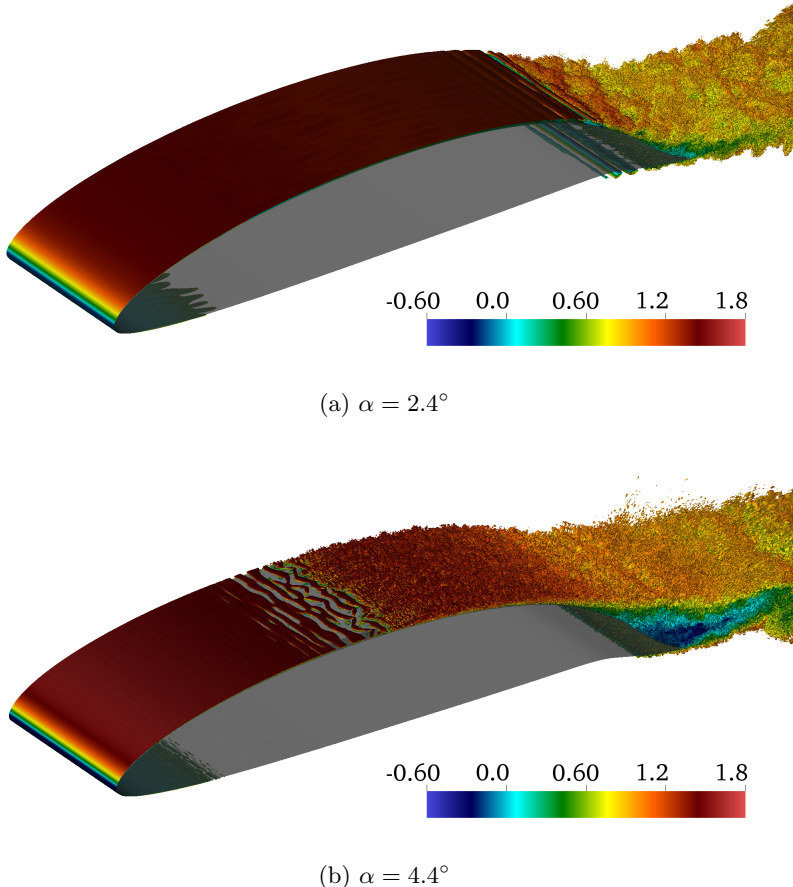


Figure 5: Instantaneous vortical structures identified by the  $\lambda_2$  criterion for the two stationary angle of attack simulations.

solutions of the stationary airfoil simulation at the angle of attack of  $\alpha = 2.4^\circ$ . This point represents the minimum of the pitch cycle and starting the pitching motion from this minimum allows us to smoothly increase the angular velocity from zero. Thus no impulsive velocities are imparted to the airfoil when the pitching motion starts. The oscillatory motion is thus prescribed by equation 4:

$$\alpha(t) = \alpha_0 + \Delta\alpha \sin(\Omega(t - t_0) + \phi_0), \quad (4a)$$

$$\text{with } \alpha_0 = 3.4^\circ, \quad \Delta\alpha = 1.0^\circ, \quad t_0 = 6.0 \quad \text{and} \quad \phi_0 = -\pi/2. \quad (4b)$$

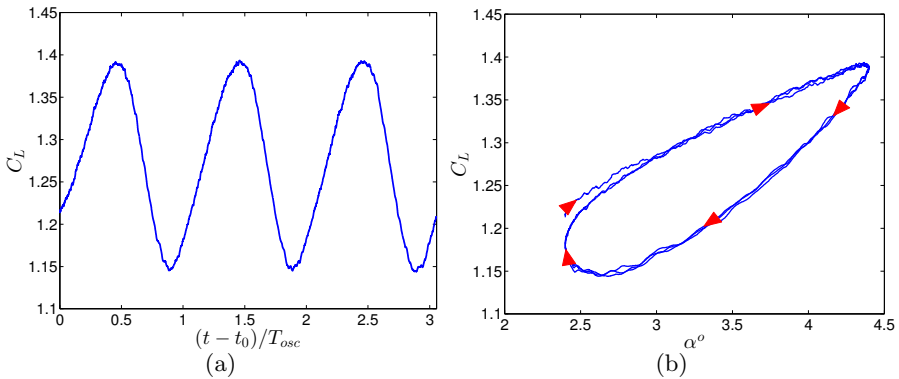


Figure 6: Variation of unsteady lift coefficient with time (left) and instantaneous angle of attack (right). Red arrows in the phase portrait indicate direction of time.

Figure 6 shows the variation of the unsteady lift coefficient  $C_L$  with time, as well as the phase portrait with respect to  $\alpha$ . One can immediately observe from the phase portrait (figure 6b) that (after a small initial transient) no large deviations of the lift coefficient occur between consecutive cycles of oscillation, indicating that the flow has settled into a regular cyclic state and further qualitative changes that may be transient in nature are not expected to occur with more pitch cycles. While the non-linearity is less obvious from the time series plot, the phase portrait clearly shows the non-linearities by way of a distorted ellipse. Linear responses trace an ellipse in the phase portrait with respect to angle of attack. Distortions of the ellipse indicate the presence of additional frequencies in the time response.

#### 4.2. Unsteady boundary layer

The spatio-temporal variation of the boundary layer can be analyzed via the instantaneous wall-shear stress. Figure 7 shows the space-time variation of the instantaneous, spanwise averaged wall-shear stress on the suction side of the airfoil surface. Areas which are strongly red in color are high shear-stress regions and thus signify turbulent flow (except the region very close to the leading edge which has a very thin boundary layer). The turbulent regions show periodic bumps in the space-time plot which are indicative of the movement of transition throughout the oscillation phases. This is consistent with the earlier studies of Mai & Hebler (2011); Hebler *et al.* (2013) and Lokatt (2017) which suggest the free movement of transition is responsible for non-linearities in the aerodynamic force coefficients. Figure 8 shows horizontal slices from the space-time plot for two different time instants which represent the instantaneous spatial variations of  $\tau_w$ .

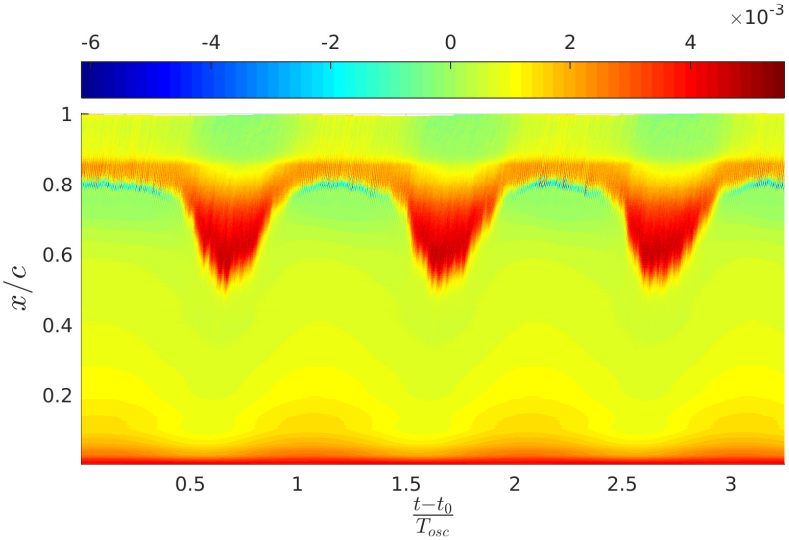


Figure 7: Spatio-temporal variation of wall-shear stress. The  $y$ -axis represents the chord-wise location while the  $x$ -axis represents the normalized simulation time. The colors represent the instantaneous, spanwise-averaged wall-shear stress value,  $\tau_w(x, t)$ , for each chord-wise location.

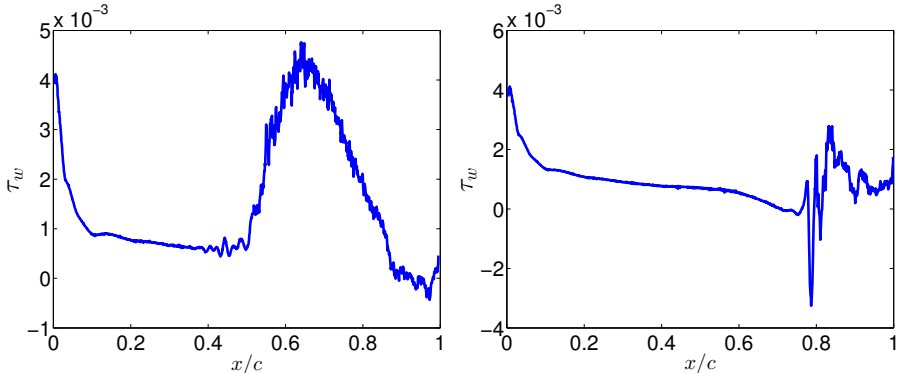


Figure 8: Instantaneous chord-wise variation of  $\tau_w(x, t)$ . Figures represent time-instants when the transition is close to its most upstream location at time  $(t - t_0)/T_{osc} = 1.60$  (left) and when it is close to the most downstream location at time  $(t - t_0)/T_{osc} = 2.25$  (right).

#### 4.3. Transition location

For further analysis a quantification of the transition point variation is necessary and to this end the instantaneous transition point needs to be defined. Since

the transition changes continuously with time, a criterion is required which is based on the instantaneous state of the flow rather than the long-time statistical average. In order to define quantities representative of the instantaneous state of the flow, we take advantage of the homogeneous direction and also perform a temporal averaging operation for a very short duration in time. Thus we evaluate statistical quantities “ $\bar{q}(x, y, t)$ ” which are defined as in equation 5:

$$\bar{q}(x, y, t) = \left( \frac{1}{z_{max} - z_{min}} \right) \left( \frac{1}{\Delta t} \right) \int_{t'=t}^{t'=t+\Delta t} \int_{z=z_{min}}^{z=z_{max}} q(x, y, z, t') dz dt'. \quad (5)$$

Here  $(z_{max} - z_{min})$  is the spanwise width of the computational domain and  $\Delta t$  is a short temporal averaging period. In order for such a quantity to be representative of the instantaneous state of the flow, the time duration of the averaging must be small. For the current case we use  $\Delta t = 3 \times 10^{-2}$ , which amounts to 0.38% of the oscillation time period during which the flow can be assumed to remain approximately in the same state. Using this procedure we evaluate the fluctuating Reynolds stress,  $\overline{u'v'}(x, y, t)$ . Large Reynolds stresses indicate turbulent flow, thus the most upstream location (on the suction side) where the quantity  $\overline{u'v'}(x, y, t)$  becomes large is denoted as the transition location. In order to prescribe a suitable threshold for “large”, the maximum value of  $|\overline{u'v'}(x, y, t)|$  across the entire boundary layer is evaluated for all times. This maximum value does not have very large variations, staying within the same order of magnitude with its mean value being  $|\overline{u'v'}|_{max} = 10^{-2}$ . The threshold for determining transition is set to 5% of this value. The transition point is thus the first point where  $|\overline{u'v'}(x, y, t)| > 5 \times 10^{-4}$ . Since the criterion is a bit arbitrary, it is cross-checked by evaluating the variance of the spanwise velocity fluctuations  $\overline{w'w'}(x, y, t)$  following the same procedure. In this case the threshold is set as  $|\overline{w'w'}(x, y, t)| > 10^{-3}$ , since the peak spanwise fluctuation intensity is found to be nearly twice the peak Reynolds stress. Growing spanwise velocity fluctuations indicate the onset of three-dimensionality, and thus they constitute a physically meaningful indicator of transition. Despite the rather ad-hoc nature of the threshold criteria, the qualitative picture of transition movement is not very sensitive to small changes in the threshold. Reducing or increasing the thresholds by a factor of 2 still produces the same qualitative trends (not shown). Figure 9 shows the phase portrait of the transition location, determined by the aforementioned criteria. The two criteria show a good quantitative agreement with each other. Figure 10 shows the calculated transition location (using  $\overline{u'v'}$ ) superposed on the wall-shear stress space-time plot. The calculated transition locations are consistent with the picture of wall-shear stress with transition marginally preceding regions of turbulent flow.

The phase portrait in figure 9 clearly shows the asymmetric flow states between the pitch-up (upper branch) and the pitch-down (lower branch) phases of the oscillation. During the pitch-up phase the transition point is near the trailing edge and has a very slow upstream movement for most part of pitch-up cycle, and later moves upstream sharply at the end of the pitch-up phase. During the pitch-down phase of the oscillation, the transition location is constantly

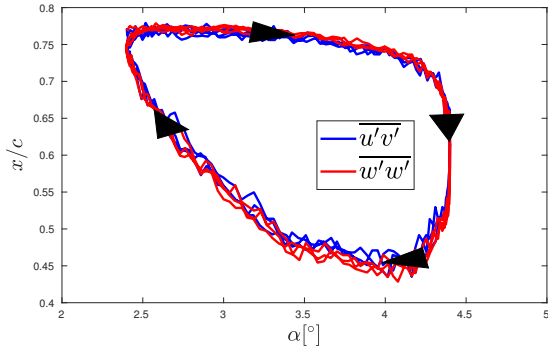


Figure 9: Empirically determined transition location using the  $|\overline{u'v'}|$  and  $|\overline{w'w'}|$  criteria. Arrows indicate the forward direction in time.

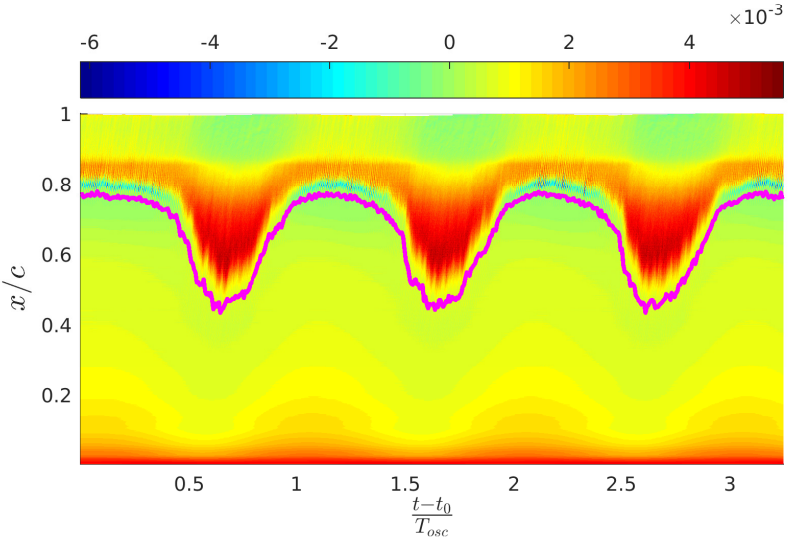


Figure 10: Empirically determined transition location (magenta curve) superposed on the space-time plot of  $\tau_w$ .

moving downstream with the motion appearing much more gradual in phase space. This phase portrait can be transformed to give a more insightful picture of the ongoing dynamics by using a phase-lag concept. In this transformation we consider the evolution of the boundary layer with respect to an effective angle of attack  $\alpha_e$  which differs from the instantaneous angle of attack by a phase-lag. The physical interpretation of the phase-lag is a simple one, *i.e.* the boundary layer adjusts to the changing flow-field in a quasi-steady manner, however there is a time lag between the airfoil motion and the boundary-layer adjustment,

and the effective angle of attack that the boundary layer perceives is different from the instantaneous angle of attack. The expression for the effective angle of attack for the current case may be written by adding an additional term to equation 4

$$\alpha_e(t) = \alpha_0 + \Delta\alpha \sin(\Omega(t - t_0) + \phi_0 + \phi_{lag}), \quad (6)$$

where  $\phi_{lag}$  is the phase lag between the instantaneous and effective angles of attack.

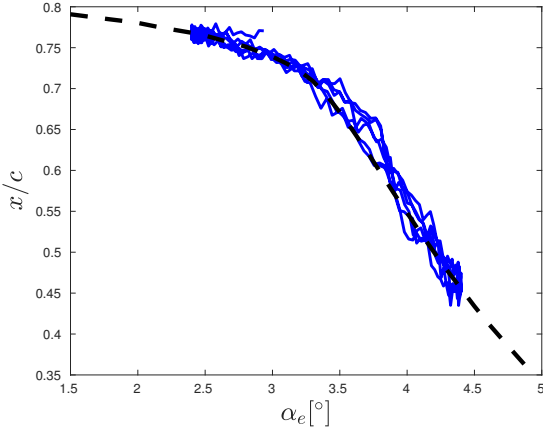


Figure 11: Phase portrait of the transition location with respect to the effective angle of attack( $\alpha_e$ ). The blue lines represent the evaluated transition location (using  $|\bar{u}'\bar{v}'|$ ) and the black dashed line represents static transition location values obtained from Xfoil.

The phase-lag concept is often used in unsteady aerodynamics (Theodorsen 1935; Leishman 2000; Bisplinghoff *et al.* 1983; McCroskey 1982; Ericsson & Reding 1988a) to describe the unsteady response of aerodynamic forces. In this case we apply the concept specifically to the evolution of the boundary layer. Figure 11 shows the phase portrait with respect to the effective angle of attack, when evaluated using a phase lag of  $\phi_{lag} = -1.0976$ . What was initially a closed orbit in the  $x/c - \alpha$  plane (figure 9) transforms into a single line when visualized in the  $x/c - \alpha_e$  plane. Surprisingly, this new phase portrait corresponds well with the static transition curve calculated using XFOIL. While such a collapse seems remarkable at first, it simply implies a quasi-steady evolution of the boundary layer in time. The transition location can be considered as a scalar value which describes the instantaneous state of the boundary layer on the airfoil. If a boundary layer evolves in a quasi-steady manner in time, its trajectory in the  $x/c - \alpha$  phase space would simply follow the trajectory of the static curve. For the unsteady cases one simply needs to consider the effective angle of attack perceived by the boundary layer, since the boundary-layer response lags behind the instantaneous angle of attack variations.

## 5. An empirical unsteady model

Given the failure of classical unsteady models to predict non-linear unsteady response, we build an empirical model which has its roots in the unsteady aerodynamic model of Theodorsen (1935), while utilizing the insight gained in the previous section on the quasi-steady evolution of the boundary layer over the airfoil. The model proposed by Theodorsen (1935) incorporates several different forms of unsteady motions (pitching, plunging and flap rotations). Once simplified to pure pitch oscillations the model for the normal force coefficient reads as

$$C_z(t) = \underbrace{\pi[\dot{\alpha} - a\ddot{\alpha}]}_{\text{I}} + \underbrace{2\pi[\alpha + \dot{\alpha}\left(\frac{1}{2} - a\right)]C(k)}_{\text{II}}, \quad (7)$$

where term I represents the added mass contribution to the normal force coefficient and term II may be viewed as the quasi-steady lift modulated by the Theodorsen transfer function  $C(k)$ . This modulation term represents the attenuation of the unsteady lift force due to the oscillating shed wake vorticity, and is a function of the reduced frequency only. Here “ $a$ ” is the distance of the axis of rotation from the mid chord location. The added-mass term is a purely harmonic term which represents the additional force on the airfoil due to the mass of the fluid close to the airfoil being accelerated along with the surface as the airfoil undergoes a pitching motion. Term II represents the effects of the quasi-steady lift force and may be reformulated as

$$2\pi[\alpha + \dot{\alpha}\left(\frac{1}{2} - a\right)] = 2\pi\alpha_{eff} = C_z^{inv}(\alpha_{eff}), \quad (8)$$

where  $\alpha_{eff}$  is an effective angle of attack perceived by the boundary layer, which differs from the instantaneous angle of attack  $\alpha$ . Since the Theodorsen model is derived from inviscid assumptions of thin airfoil theory, the term  $2\pi\alpha_{eff}$  is simply the normal force coefficient as predicted by the quasi-steady thin airfoil theory at an angle of attack of  $\alpha_{eff}$ , denoted here as  $C_z^{inv}(\alpha_{eff})$ . When non-linearities are present in the static  $C_z$  curve, this assumption is clearly violated. Calculating the contribution of the quasi-steady term from the inviscid assumptions would lead to erroneous results. In order to account for these non-linearities, we make a similar quasi-steady assumption, wherein, we assume that to a first order approximation, the boundary layer evolves in a quasi-steady manner throughout the pitch cycle. The results of the previous section strengthen the validity of this assumption. However the effective angle of attack is different from the instantaneous angle of attack and the phase-lag is not known a-priori. Since the flow does not satisfy inviscid assumptions, the value of the quasi-steady term would need to be determined by an empirically calculated  $C_z$  curve. Therefore we replace  $C_z^{inv}(\alpha_{eff})$  with an empirically calculated static normal force coefficient curve, denoted as  $C_z^{emp}(\alpha_{eff})$ . The empirically calculated curve for a Reynolds number of  $Re_c = 10^6$  with the current airfoil is shown in figure 1. Since it is unclear that the phase lag (or gain) for both the added mass term as well as the quasi-steady term would

remain the same as when the inviscid thin airfoil theory applies, we leave these terms as parameters to be determined from the data. The empirical model thus reads

$$C_z(t) = A_1 \sin(\omega t + \theta) + C_z^{emp}(\gamma(t)), \quad (9a)$$

$$\gamma(t) = \alpha_0 + \Delta\alpha \sin(\omega t - \phi_{lag}). \quad (9b)$$

Where the instantaneous angle of attack follows the relation

$$\alpha(t) = \alpha_0 + \Delta\alpha \sin(\omega t). \quad (10)$$

Thus the empirical model has three independent parameters to be determined.  $A_1$ , which represents the strength of the added-mass term.  $\theta$ , which represents the phase gain/lag of this added-mass contribution with respect to the instantaneous angle of attack, and  $\phi_{lag}$ , which represents the phase-lag of the quasi-steady term. If the empirical  $C_z^{emp}(\alpha)$  curve is linear with respect to  $\alpha$ , the time-response of the model will be purely harmonic.

The model parameters are then obtained using a least-squares fit to the experimental (or numerical) data. In the present work we utilize the unsteady experimental measurements of Lokatt (2017) to test the applicability of the model described by equation 9. The measurements were carried out for a Reynolds number of  $Re_c = 10^6$  and  $Re_c = 7.5 \times 10^5$  for a wide range of angles of attack and with small amplitude pitch oscillations. The static  $C_z$  curve required by the model was also obtained from the experimental data provided by Lokatt (2017). Figure 12 shows the static curve obtained in the experimental results for  $Re_c = 10^6$ . Surprisingly, the simple model showed a good fit with the

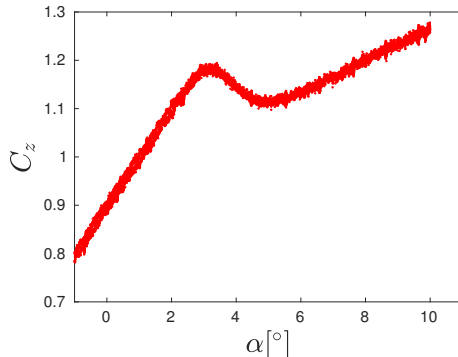


Figure 12: The experimental static normal force coefficient curve  $C_z^{emp}(\alpha)$  obtained by Lokatt (2017).

experimental data. Figure 13 shows the least-squares fit for the data obtained at a mean angle of attack of  $\alpha_0 = 2.8^\circ$ , pitch amplitude of  $\Delta\alpha = 1^\circ$  and different reduced frequencies. The red dots indicate the experimental values while the solid black line is the least-squares fit to the experimental data. As can be seen

in figure 12, the mean angle of  $2.8^\circ$  places the oscillation region at the start of the  $\alpha$  region exhibiting non-linearities in the static curve. The good agreement

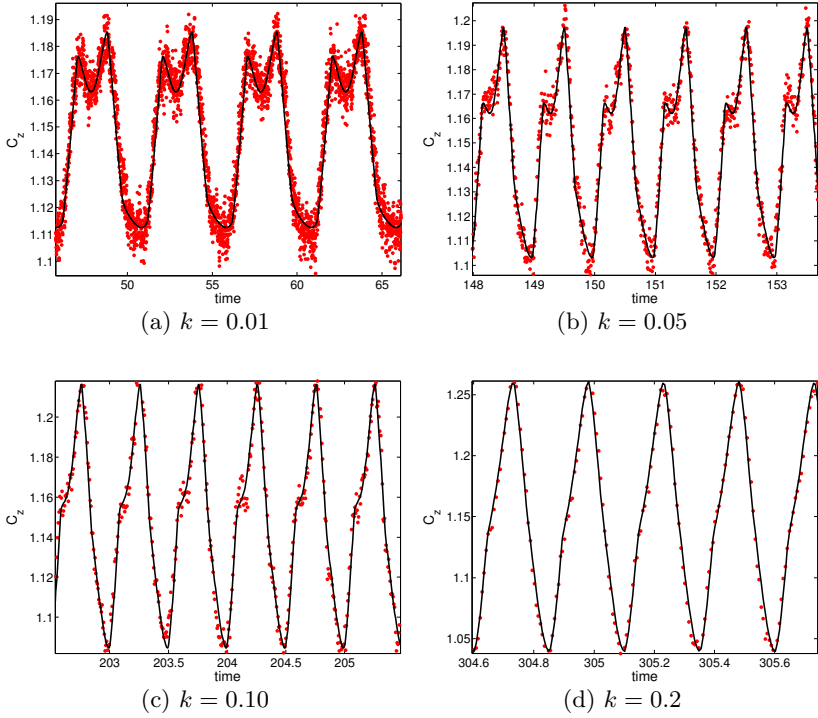


Figure 13: Least-squares fit of the empirical model to the experimental data for a mean angle of attack of  $\alpha_0 = 2.8^\circ$ ,  $\Delta\alpha = 1^\circ$  and a selection of reduced frequencies  $k$ .

is not confined to a single mean angle of attack. The model was tested with several different parameter combinations of mean angle of attack and reduced frequencies and a fairly good agreement was found for all cases considered, even for some cases with relatively high reduced frequencies of  $k \approx 0.4$ . Figure 14 shows another set of experimental data within the non-linear regime along with the least squares fit of the model. Thus the quasi-steady phase-lag concept for the temporal evolution of the boundary layer over the airfoil appears to be applicable for several different parameter values, even when boundary-layer transition location changes significantly. The model however is not predictive, but rather allows for a-posteriori analysis of the data since the phase lag/gain of the boundary-layer and added-mass terms are not known a-priori. It must be kept in mind however that only data from small-amplitude pitch oscillations with a relatively narrow range of reduced frequencies  $k < 0.4$  was available and thus the applicability of such a simple model for more general cases of

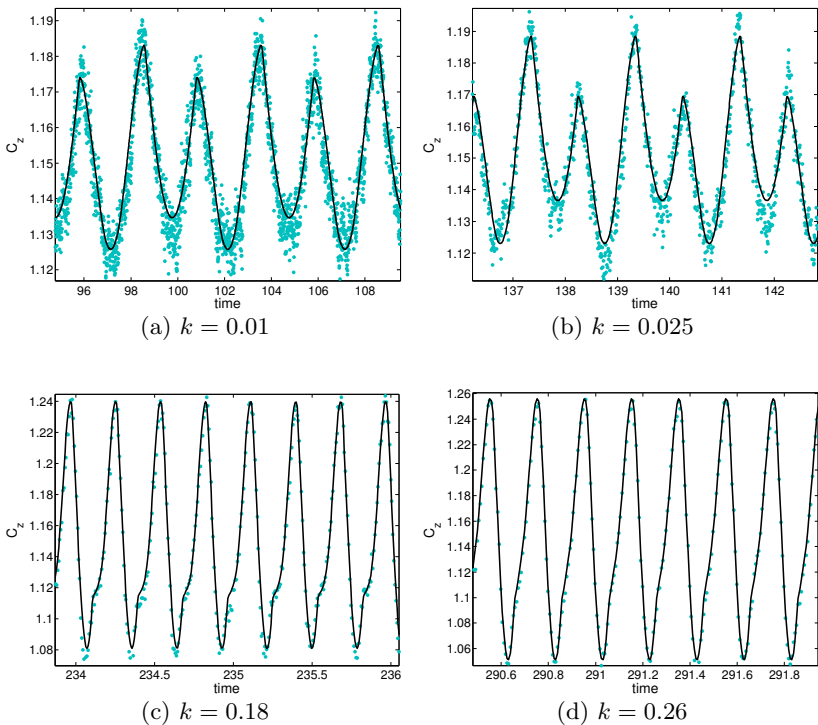


Figure 14: Least-squares fit of the empirical model to the experimental data for a mean angle of attack of  $\alpha_0 = 3.2^\circ$ ,  $\Delta\alpha = 1^\circ$  and different reduced frequencies  $k$ .

pitching remains unknown. More data would be required to infer definitive trends of the model parameters ( $A_1$ ,  $\theta$ ,  $\phi_{lag}$ ) and to make conclusive remarks on the predictive capabilities of such a simple model.

## **6. Conclusion and summary**

This report presents some of the initial results of LES of an unsteady natural laminar flow airfoil. The parameter range of the unsteady simulations was based on XFOIL calculations and experimental data. Preliminary simulations of stationary airfoils were performed to ensure the desired aerodynamic characteristics are captured by the numerical simulations. The unsteady simulations showed a non-linear response for the aerodynamic force coefficients while the unsteady boundary-layer development showed large variations of the point of transition over the suction side of the airfoil. These large variations in transition are shown to be linked to the static characteristics of the airfoil. The temporal variation can be related to the static transition curve with the use of a simple phase-lag

concept, which implies that the boundary-layer evolution can be considered to be quasi-steady in time (at least as a first order assumption).

Based on this phase-lag and quasi-steady concept, an empirical model is developed to explain the non-linearities observed in the unsteady response of natural laminar flow airfoils. The empirical model has its roots in the unsteady model proposed by Theodorsen (1935) and is able to model the aerodynamic non-linearities observed in the experiments of Lokatt (2017).

Higher resolution simulations for this flow case are ongoing.

## Acknowledgements

Financial support for this work was provided by Vinnova through the NFFP project UMTAPS, with grant number 2014-00933, and the European Research Council under grant agreement 694452-TRANSEP-ERC-2015-AdG. The computations were performed on resources provided by the Swedish National Infrastructure for Computing (SNIC) at the PDC Center for High Performance Computing at the Royal Institute of Technology (KTH). Simulations were also carried out at the High Performance Computing Center, Stuttgart (HLRS), with the computer time provided by the 15<sup>th</sup> PRACE Project Access Call (number 2016163965).

The authors would like to thank Roger Larsson from SAAB and Dr. Eller and Dr. Lokatt for all the insightful discussions on the aerodynamic aspects of the project. The authors would also like to thank Elektra Kleusberg for the helpful comments on the manuscript.

## REFERENCES

- BISPLINGOFF, L. R., ASHLEY, H. & HALFMAN, R. L. 1983 *Aeroelasticity*. Dover Publications INC.
- BRANDT, L., SCHLATTER, P. & HENNINGSON, D. S. 2004 Transition in boundary layers subject to free-stream turbulence. *Journal of Fluid Mechanics* **517**.
- DONG, S., KARNIADAKIS, G. E. & CHRYSSOSTOMIDIS, C. 2014 A robust and accurate outflow boundary condition for incompressible flow simulations on severely-truncated unbounded domains. *Journal of Computational Physics* **261**, 83–105.
- DRELA, M. 1989 *XFOIL: An Analysis and Design System for Low Reynolds Number Airfoils*, pp. 1–12. Berlin, Heidelberg: Springer Berlin Heidelberg.
- ERICSSON, L. & REDING, J. 1988 Fluid mechanics of dynamic stall part i. unsteady flow concepts. *Journal of Fluids and Structures* **2** (1), 1 – 33.
- FISCHER, P. F., LOTTES, J. W. & KERKEMEIER, S. G. 2008 Nek5000 web page. <http://nek5000.mcs.anl.gov>.
- GLAUERT, H. 1930 The force and moment on an oscillating aerofoil. In *Vorträge aus dem Gebiete der Aerodynamik und verwandter Gebiete: Aachen 1929* (ed. A. Gilles, L. Hopf & T. v. Kármán), pp. 88–95. Berlin, Heidelberg: Springer Berlin Heidelberg.
- GREEN, J. E. 2008 Laminar flow control-back to the future. *38th Fluid Dynamics Conference and Exhibit, Fluid Dynamics and Co-located Conferences, AIAA 3738*.

- HALFMAN, R. L. 1952 Experimental aerodynamic derivatives of a sinusoidally oscillating airfoil in two-dimensional flow. *Tech. Rep.*. National Advisory Committee for Aeronautics; Washington, DC, United States.
- HEBLER, A., SCHOJDA, L. & MAI, H. 2013 Experimental investigation of the aeroelastic behavior of a laminar airfoil in transonic flow. In *Proceedings IFASD*.
- HO, L.-W. & PATERA, A. T. 1990 A Legendre spectral element method for simulation of unsteady incompressible viscous free-surface flows. *Computer Methods in Applied Mechanics and Engineering* **80** (1), 355 – 366.
- HO, L.-W. & PATERA, A. T. 1991 Variational formulation of three-dimensional viscous free-surface flows: Natural imposition of surface tension boundary conditions. *International Journal for Numerical Methods in Fluids* **13** (6), 691–698.
- HOSSEINI, S. M., VINUESA, R., SCHLATTER, P., HANIFI, A. & HENNINGSON, D. S. 2016 Direct numerical simulation of the flow around a wing section at moderate Reynolds number. *International Journal of Heat and Fluid Flow* **61**, 117 – 128.
- JEONG, J. & HUSSAIN, F. 1995 On the identification of a vortex. *Journal of Fluid Mechanics* **285**.
- KARMAN, T. V. & SEARS, W. R. 1938 Airfoil theory for non-uniform motion. *Journal of Aeronautical Sciences* **5** (10), 379–390.
- KLEUSBERG, E. 2017 Wind turbine simulations using spectral elements. Licentiate thesis, Royal Institute of Technology (KTH), Stockholm, Sweden.
- LANGTRY, R. B. & MENTER, F. R. 2009 Correlation-Based Transition Modeling for Unstructured Parallelized Computational Fluid Dynamics Codes. *AIAA Journal* **47**, 2894–2906.
- LEISHMAN, J. G. 2000 *Principles of Helicopter Aerodynamics*. Cambridge University Press.
- LOKATT, M. 2017 On aerodynamic and aeroelastic modeling for aircraft design. Doctoral thesis, KTH Royal Institute of Technology.
- LOKATT, M. & ELLER, D. 2017 Robust viscous-inviscid interaction scheme for application on unstructured meshes. *Computers & Fluids* **145**, 37 – 51.
- LOMAX, H. 1954 Lift developed on unrestrained rectangular wings entering gusts at subsonic and supersonic speeds. *Tech. Rep.*. National Advisory Committee for Aeronautics. Ames Aeronautical Lab.; Moffett Field, CA, United States.
- LOMAX, H., HEASLET, M. A., FULLER, F. B. & SLUDER, L. 1952 Two-and three-dimensional unsteady lift problems in high-speed flight. *Tech. Rep.*. National Advisory Committee for Aeronautics. Ames Aeronautical Lab.; Moffett Field, CA, United States.
- MAI, H. & HEBLER, A. 2011 Aeroelasticity of a laminar wing. In *Proceedings IFASD*. Paris.
- MCCROSKEY, W. J. 1982 Unsteady airfoils. *Annual Review of Fluid Mechanics* **14** (1), 285–311.
- NEGI, P. S., VINUESA, R., HANIFI, A., SCHLATTER, P. & HENNINGSON, D. S. 2017 Unsteady aerodynamic effects in pitching airfoils studied through large-eddy simulations. In *Proc. Int. Symp. Turbulence & Shear Flow Phenomenon (TSFP-10)*. Chicago, USA.
- SCHLATTER, P. 2001 Direct numerical simulation of laminar-turbulent transition in boundary layer subject to free-stream turbulence. Diploma thesis, Royal Institute of Technology (KTH), Stockholm, Sweden.

- SCHLATTER, P., BRANDT, L., DE LANGE, H. C. & HENNINGSON, D. S. 2008 On streak breakdown in bypass transition. *Physics of Fluids* **20** (10), 101505.
- THEODORSEN, T. 1935 General theory of aerodynamic instability and the mechanism of flutter. *Tech. Rep.*. National Advisory Committee for Aeronautics; Langley Aeronautical Lab.; Langley Field, VA, United States.
- VINUESA, R., NEGI, P. S., HANIFI, A., HENNINGSON, D. S. & SCHLATTER, P. 2017 High-fidelity simulations of flow around wings at high Reynolds numbers. In *Proc. Int. Symp. Turbulence & Shear Flow Phenomenon (TSFP-10)*. Chicago, USA.



# Paper 3

3



# Unsteady aerodynamic effects in small-amplitude pitch oscillations of an airfoil

P. S. Negi, R. Vinuesa, A. Hanifi, P. Schlatter and D. S. Henningson

Department of Mechanics, Linné FLOW Centre and Swedish e-Science Research Centre (SeRC), KTH Royal Institute of Technology, SE-100 44 Stockholm, Sweden

*In Proc. 10<sup>th</sup> Int. Sym. on Turbulence & Shear Flow Phenomenon (TSFP-10 extended version)*

High-fidelity wall-resolved large-eddy simulations (LES) are utilized to investigate the flow-physics of small-amplitude pitch oscillations of an airfoil at  $Re_c = 100,000$ . The investigation of the unsteady phenomenon is done in the context of natural laminar flow airfoils, which can display sensitive dependence of the aerodynamic forces on the angle of attack in certain “off-design” conditions. The dynamic range of the pitch oscillations is chosen to be in this sensitive region. Large variations of the transition point on the suction-side of the airfoil are observed throughout the pitch cycle resulting in a dynamically rich flow response. Changes in the stability characteristics of a leading-edge laminar separation bubble has a dominating influence on the boundary layer dynamics and causes an abrupt change in the transition location over the airfoil. The LES procedure is based on a relaxation-term which models the dissipation of the smallest unresolved scales. The validation of the procedure is provided for channel flows and for a stationary wing at  $Re_c = 400,000$ .

**Key words:** unsteady aerodynamics, dynamic-response, transition, wall-resolved les

---

## 1. Introduction

A large focus of the research on unsteady wings tends towards stall dynamics such as the earlier works of McCroskey (1981); McCroskey *et al.* (1982); McCroskey (1973); McCroskey *et al.* (1976); Carr *et al.* (1977); Ericsson & Reding (1988a,b), *etc.* More recent works by Dunne & McKeon (2015); Rival & Tropea (2010); Choudhry *et al.* (2014); Visbal (2011, 2014); Visbal & Garmann (2017); Alferez *et al.* (2013); Rosti *et al.* (2016) *etc.* continue the investigation which appears far from complete. The review by McCroskey (1982) and a more recent one by Coorke & Thomas (2015) provide an overview of the dynamic stall process. Studies on the aerodynamic behavior of small-amplitude pitch oscillations are typically done from the perspective of aeroelasticity where investigations tend to focus on the time varying aerodynamic forces on the airfoil with much less

attention paid to the boundary-layer characteristics. Some studies focusing on the time dependent boundary layer in small pitch amplitudes include the work done by Pascazio *et al.* (1996) which shows a time delay in laminar-turbulent transition during pitching. Nati *et al.* (2015) analyzed the effect of small amplitude pitching on a laminar separation bubble at low Reynolds numbers. Mai & Hebler (2011) and Hebler *et al.* (2013) investigate the boundary layer changes in an oscillating natural laminar flow airfoil in transonic conditions. Such cases qualitatively represent small changes in operating conditions, such as

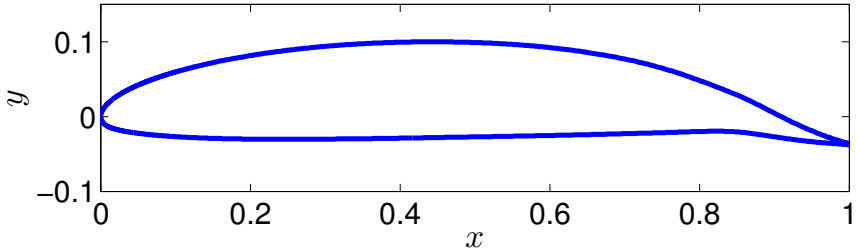


Figure 1: Natural Laminar Flow (NLF) airfoil tested at the Aeronautical and Vehicle engineering department of KTH (Lokatt & Eller 2017; Lokatt 2017)

the changes due to structural deformations or small trailing-edge flap deflections. The understanding of flow response to such changes can be crucial in cases where small perturbations induce large variations in aerodynamic forces. Such sensitive dependence of aerodynamic forces may be found in the static characteristics of natural laminar flow (NLF) airfoils for a certain range of angle of attack. Their performance critically depends on maintaining laminar flow over the suction side of the airfoil and a loss of laminar flow over the airfoil causes large variations of the aerodynamic forces. In addition to such sensitive dependence of the aerodynamic characteristics, recent transonic unsteady experiments using NLF airfoils have brought to light a peculiar property of these airfoils. The unsteady aerodynamic coefficients for laminar airfoils exhibit a non-linear dynamic response to simple harmonic pitch motions (Mai & Hebler 2011; Hebler *et al.* 2013). Such a non-linear response is inconsistent with the predictions of classical unsteady aerodynamic models (Theodorsen 1935). Similar experiments within the subsonic range have been performed by Lokatt (2017) who also found strongly non-linear behavior of the normal force coefficient. These non-linearities occur only for oscillations within a certain range of angle of attack ( $\alpha$ ) and have been strongly linked to the free movement of transition over the suction side of the airfoil. They seem to be nearly absent when suction side transition is fixed at the leading-edge (Mai & Hebler 2011; Lokatt 2017).

The present work investigates the flow physics of small-amplitude pitch oscillations of a laminar airfoil (figure 1). The airfoil was designed at the Aeronautical and Vehicle Engineering department of KTH, where it has been used in previous experimental and numerical works (Lokatt & Eller 2017). The same airfoil was used in the unsteady experiments of Lokatt (2017). The simulations

are performed at a chord-based Reynolds number of  $Re_c = 100,000$ . The angle of attack range for the oscillation was chosen from the static characteristics of the airfoil. The static characteristics were calculated using an integral boundary layer code XFOIL (Drela 1989), which predicted sharp changes in the coefficient of moment ( $C_m$ ) and suction-side transition location (figure 2) above an angle of attack  $\alpha > 6^\circ$ . The steep slope of the coefficient of moment curve indicates a region where aerodynamic forces are sensitive to small changes in  $\alpha$ . The pitch oscillations are performed within this sensitive region. Simulations with a static airfoil are performed to ascertain the exact dynamic range of the pitching motion which is described in section 3.

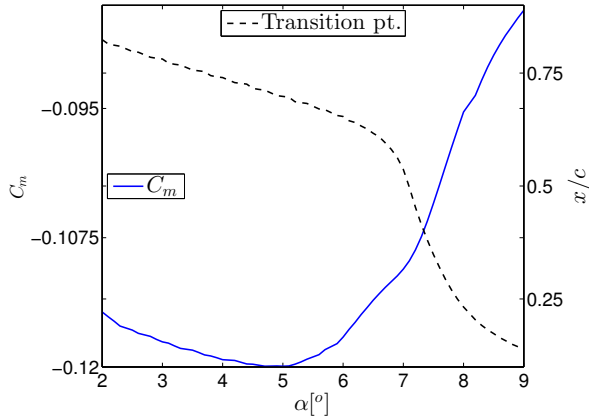


Figure 2: Coefficient of moment ( $C_m$ ) (values on the left axis), and suction side transition location (values on the right axis) as calculated using XFOIL.

In recent works, wall-resolved large-eddy simulations have proven to be an effective tool for studying flow physics at high Reynolds numbers with a computational cost which is much lower than that of direct numerical simulations (DNS). Some of the works to utilize this method include spatially evolving boundary layers (Eitel-Amor *et al.* 2014), turbulent channel flows (Schlatter *et al.* 2006*b,a*), pipe flows (Chin *et al.* 2015) and flow over wings (Uzun & Hussaini 2010; Lombard *et al.* 2016). Successful application of the approach has motivated its use in the present work, which aims to gain insight into the flow-physics of unsteady airfoils undergoing small amplitude pitch oscillations.

The remainder of the paper is divided into 3 sections. Section 2 describes the numerical setup and presents the results of the validation of the LES. Results of both the stationary and pitching simulations are discussed in Section 3. The conclusions of the study are presented in Section 4.

## 2. Computational setup

### 2.1. Numerical method

The computational code used for the simulations is Nek5000, which is an open-source incompressible Navier–Stokes solver developed by Fischer *et al.* (2008) at Argonne National Laboratory. It is based on a spectral-element method which allows the mapping of elements to complex geometries along with a high-order spatial discretization within the elements. The method uses Lagrange interpolants as basis functions and utilizes Gauss–Lobatto–Legendre (GLL) quadrature for the distribution of points within the elements. The spatial discretization is done by means of the Galerkin approximation, following the  $P_N$ - $P_{N-2}$  formulation (Maday & Patera 1989). An 11<sup>th</sup> order polynomial approximation is used for the velocity with a 9<sup>th</sup> order approximation for pressure. The nonlinear terms are treated explicitly by third-order extrapolation (EXT3), whereas the viscous terms are treated implicitly by a third-order backward differentiation scheme (BDF3). Aliasing errors are removed with the use of over-integration. The Arbitrary-Lagrangian-Eulerian (ALE) formulation is used to account for the mesh deformation due to the motion of the pitching airfoil (Ho & Patera 1990, 1991). All equations are solved in non-dimensional units with the velocities normalized by the reference free-stream velocity  $U_0$  and the length scales in all directions are normalized by the chord length  $c$ . The resultant non-dimensional time unit is given by  $c/U_0$ .

### 2.2. Relaxation-term large-eddy simulation (RT-LES)

The LES method is based on the RT3D variant of the ADM-RT approach first used by Schlatter *et al.* (2004). The method supplements the governing equations with a dissipative term ( $\chi\mathcal{H}(u)$ ). The equations for the resolved velocity and pressure thus read as

$$\frac{\partial u}{\partial t} + u \cdot \nabla u = -\frac{1}{\rho} \nabla p + \frac{1}{Re} \nabla^2 u - \chi\mathcal{H}(u), \quad (1a)$$

$$\nabla \cdot u = 0, \quad (1b)$$

where  $\mathcal{H}$  is a high-pass spectral filter and  $\chi$  is a model parameter. Together the two parameters determine the strength of the dissipative term. The method has been used in earlier studies of spatially developing boundary layers (Eitel-Amor *et al.* 2014) and channel flows (Schlatter *et al.* 2006b). The method has been shown to be reliable in predicting transition location and also preserving the characteristic structures which are seen in the DNS of transitional flows (Schlatter *et al.* 2006b).

A number of tests were carried out in a channel flow at a friction Reynolds number of  $Re_\tau = 395$ , and the results are compared with the DNS data of Moser *et al.* (1999). The final mesh was set up such that the streamwise resolution was  $\Delta x^+ = 18$  and the spanwise resolution was  $\Delta z^+ = 9$ . The first point in the wall-normal direction was set at  $\Delta y_w^+ = 0.64$  and the wall-normal resolution near the boundary layer edge was  $y_{max}^+ = 11$ . The superscript  $+$  indicates

normalization in inner units. A comparison of the results for the turbulent channel flow is shown for the mean velocity in figure 3a, and for the turbulent kinetic energy (TKE) budget in figure 3b. The dissipation profile shown in the figure is the sum of resolved dissipation and the added dissipation by the relaxation term. A good agreement with the DNS is found for the mean velocity and all the kinetic energy budget terms (including the total dissipation). The resolution used this study is much finer than the typical LES and closer to the coarse DNS resolutions used in the studies of turbulent flows. A very similar resolution is used in the simulation of spatially developing boundary-layer over a flat-plate by Eitel-Amor *et al.* (2014) where the ADM-RT model is used. Similarly, LES cases of pipe flows at  $Re_\tau \approx 1000$  by Chin *et al.* (2015) uses slightly coarser resolutions than the one used in the present study.

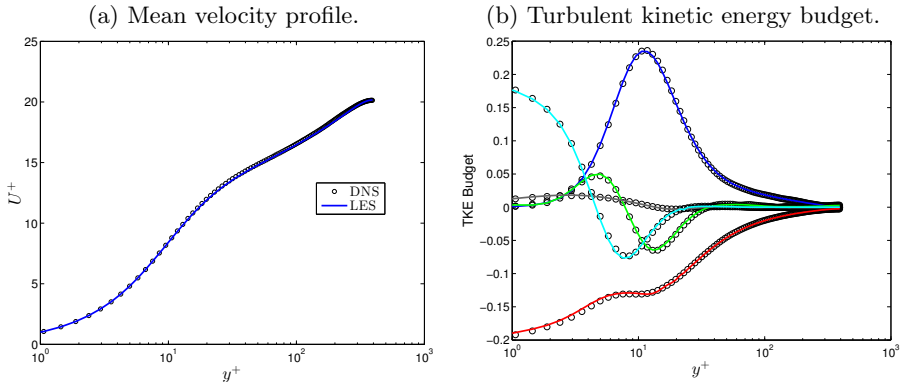


Figure 3: Comparison of mean velocity profile and turbulent kinetic energy budget. Circles represent the DNS data from Moser *et al.* (1999) while the lines represent the values from the LES. All values are normalized with inner units. The individual terms are color coded as: Production (blue), dissipation (red), viscous diffusion (cyan), turbulent diffusion (green), velocity-pressure correlation (gray)

### 2.3. Mesh generation

The optimum mesh resolution (in inner units) obtained in the channel flow results is then used to design the mesh around the airfoil. Wall-shear stress data is obtained using XFOIL to estimate the grid spacing on the airfoil. A trip is introduced in XFOIL at  $x/c \approx 0.1$  to obtain turbulent wall-shear values on both the suction and pressure sides of the airfoil. Here  $c$  denotes the chord length. The grid design around the airfoil uses the following criteria:

- For  $0.1 < x/c < 0.6$ ,  $\Delta x^+ = 18$ ,  $\Delta y_{wall}^+ = 0.64$  and  $\Delta y_{max}^+ = 11$ , using the local wall-shear ( $\tau_w$ ) values on the airfoil. Since the flow is expected to be laminar on the pressure side, the stream-wise resolution is slightly relaxed to  $\Delta x^+ = 25$  while keeping the same wall-normal resolution.

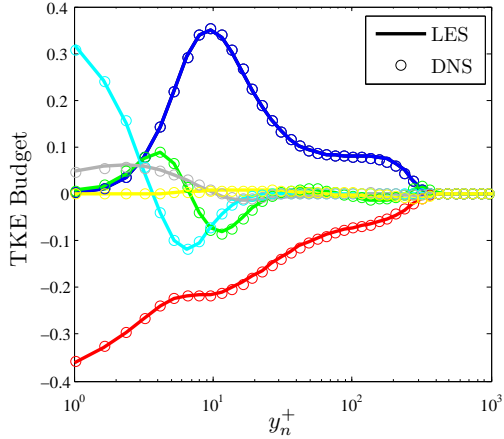


Figure 4: Comparison of turbulent kinetic energy budget for a NACA4412 wing section at the suction side location of  $x/c = 0.7$ . The circles represent DNS data from Hosseini *et al.* (2016) while the lines are data from the LES. The individual terms are color coded as: Production (blue), dissipation (red), viscous diffusion (cyan), turbulent diffusion (green), velocity-pressure correlation (gray), convection (yellow)

- For  $x/c < 0.1$ , the peak  $\tau_w$  value over the suction side of the airfoil is used to estimate the grid spacing.
- For  $x/c > 0.6$ , the suction side experiences a large adverse pressure gradient which significantly reduces  $\tau_w$  values. Therefore, the  $\tau_w$  values from the pressure side are used for both the suction and pressure sides.
- A structured mesh is used, which is extruded in the spanwise direction. Hence the spanwise resolution is constant throughout the domain. The resolution is set to  $\Delta z^+ = 9$ , where the peak  $\tau_w$  value from the suction side is used.

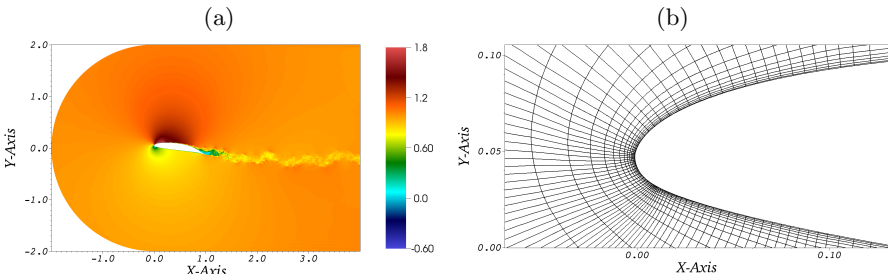


Figure 5: (a) 2D section of the simulation domain. Colors represent the instantaneous streamwise velocity. (b) Close-up view of the spectral-element grid near the airfoil surface.

A different criterion is needed for defining the resolution in the wake where the wall-based criteria are not valid. Accordingly, Reynolds-averaged Navier–Stokes (RANS) simulations were performed using the transition  $k\text{--}\Omega$  SST model (Langtry & Menter 2009) with ANSYS® FLUENT, to estimate the Kolmogorov length scale ( $\eta$ ) in the wake region. The RANS is setup with domain boundaries at a distance of 100 chords from the airfoil. The grid in the wake region for the LES is designed such that the average grid spacing between the GLL points follows the criteria:  $\Delta x/\eta < 9$ . The computational domain is set up such that the far field boundaries of the computational domain are two chords away from the airfoil leading edge in either direction. The outflow boundary is four chords downstream from the airfoil leading edge and the inlet is designed as a curved inflow boundary with a constant radial distance of two chords from the leading edge of the airfoil. The spanwise width of the domain is  $l_z = 0.25$  chords. The domain can be visualized in figure 5a and a close-up view of the spectral-elements is shown in (figure 5b). Each of the spectral-elements are further discretized by  $12 \times 12 \times 12$  grid points in 3D, corresponding to an 11<sup>th</sup> order spectral discretization. Periodic boundary conditions are imposed on the spanwise boundaries, while the energy-stabilized outflow condition suggested by Dong *et al.* (2014) is imposed on the outflow boundary. Velocity field data for locations corresponding to the boundaries of the LES computational domain is extracted from an unsteady RANS simulation. The extracted data is imposed as a Dirichlet boundary condition on these boundaries for the LES. The method is very similar to the one used by Hosseini *et al.* (2016) in their DNS of flow around a wing section. In order to simulate low turbulence flight conditions, free-stream turbulence of intensity  $Ti = 0.1\%$  is superimposed on the Dirichlet boundary conditions. The free-stream turbulence is generated using Fourier modes with a von Kármán spectrum. The procedure is similar to the one described in Schlatter (2001); Brandt *et al.* (2004) and Schlatter *et al.* (2008) and has been used for the study of transition in flat plate boundary layers under the influence of free-stream turbulence. The same method has also been used for generating grid-turbulence in simulations of wind-turbines (Kleusberg 2017).

A validation of the above methodology for complex geometries such as a wing section was performed at a chord based Reynolds number of  $Re_c = 400,000$  for NACA4412 airfoil. The LES grid resolution was setup with the same grid criteria as described above. The domain boundaries and boundary conditions are identical to the setup in Hosseini *et al.* (2016). A comparison of the wall-normal profiles of the normalized kinetic energy budget is shown in figure 4. The profiles are extracted a streamwise location of  $x/c = 0.7$  on the suction side of the airfoil. The LES profiles (lines) match well with the DNS data (circles) of Hosseini *et al.* (2016), signifying the high accuracy of the LES with the current resolution.

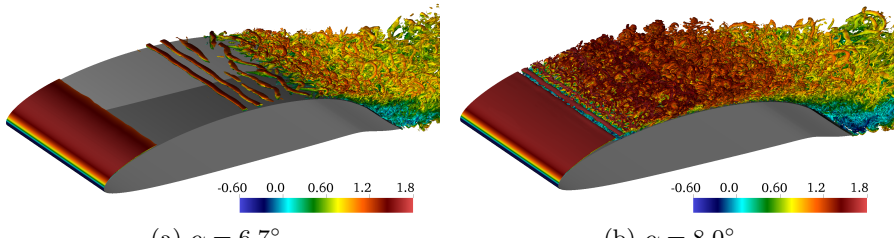


Figure 6: Isocontours of instantaneous  $\lambda_2$  structures observed for two different (stationary) angles of attack.

### 3. Results and discussion

### 3.1. Steady results

Simulations with a stationary airfoil were performed to investigate the location of transition without pitching motion. The simulations were performed for  $Re_c = 100,000$  at two different angles of attack ( $\alpha = 6.7^\circ$  and  $\alpha = 8.0^\circ$ ). As observed in figure 6, the iso-contours of coherent structures, identified by negative  $\lambda_2$  method (Jeong & Hussain 1995), show a substantial change in transition location for a small  $\Delta\alpha = 1.3^\circ$ . For  $\alpha = 6.7^\circ$  the strong pressure gradient effects near the trailing edge cause transition at  $x/c \approx 0.7$ . While for  $\alpha = 8.0^\circ$ , a leading-edge laminar separation bubble forms, causing flow transition much closer to the leading edge at  $x/c \approx 0.2$ . Such a leading-edge laminar separation bubble is not observed for the  $\alpha = 6.7^\circ$  case. The results are consistent with the trends obtained from XFOIL calculations, showing a large variation in the transition point within a small  $\alpha$  change (figure 2).

### 3.2. Unsteady boundary layer characteristics

Once the static characteristics of the airfoil are obtained, the dynamic effects on the boundary layer are investigated by pitching the airfoil about a mean angle  $\alpha_0 = 6.7^\circ$  with an amplitude of  $\Delta\alpha = 1.3^\circ$ . The reduced frequency of oscillation is  $k = 0.5$  and the pitch axis is located at  $(x_0, y_0) = (0.35, 0.034)$ . The reduced frequency is defined as  $k = \Omega b/U_0$ , where  $\Omega$  is the angular frequency of oscillation,  $b$  is the semi-chord length and  $U_0$  is the free-stream velocity. The motion of the airfoil is prescribed by equation 2. The pitching motion corresponds to an oscillation time period of  $T_{osc} = 2\pi$ .

$$\alpha = \alpha_0 + \Delta\alpha \sin(\Omega t). \quad (2)$$

The time variation of the coefficient of lift ( $C_L$ ) is shown in figure 7. The initial phase of pitching motion is carried out using a lower resolution (polynomial order  $N = 5$ ) to simulate the initial transient period of the flow at a lower computational cost. The polynomial order is then smoothly raised to  $N = 11$  before the fourth pitch cycle. Due to the fairly large separation at the trailing edge, effects of transition movement and turbulence, successive pitch cycles are not expected to have identical behavior, however some of qualitatively repeating

trends can be observed. The behavior of the lift coefficient shows a chaotic but qualitatively repeating pattern where  $C_L$  shows a smooth increase during the pitch-up motion, with strong secondary effects occurring near the maxima of the pitch cycles. Similarly in the pitch-down phase the lift decreases smoothly with secondary effects again becoming important at the minima of the pitch-cycles.

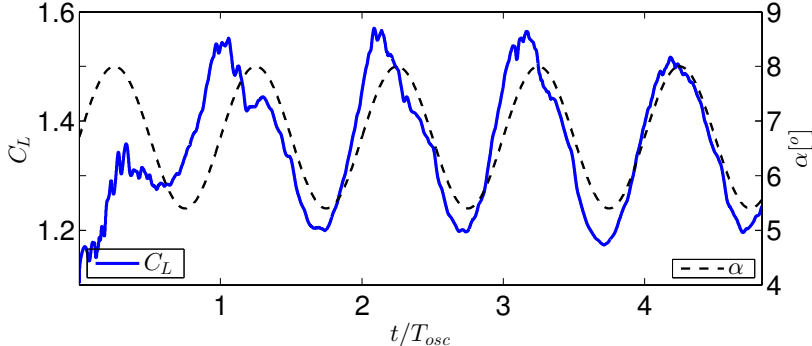


Figure 7: Coefficient of lift ( $C_L$  —) and angle of attack ( $\alpha$  --) variation with time.  $C_L$  is on the left axis while  $\alpha$  is on the right axis.

In order to understand the time variation of the spatially developing boundary layer on the airfoil, we analyze the space-time evolution of the instantaneous spanwise averaged wall-shear stress. The space-time surface plot is shown in figure 8a, which spans the fourth and fifth pitch cycles. The color specifies the value of wall-shear stress on the suction side of the airfoil. Regions with color intensity strongly towards red are indicative of high shear and thus turbulent flow. The exception to the rule being the region close to the leading edge where the flow is laminar but a high shear region exists due to the extremely thin boundary layer close to the stagnation point. The same space-time surface is shown again as a binary colored surface plot in figure 8b, where black colored regions indicate negative wall-shear stress and hence separated flow, while the white region corresponds to locations with attached flow ( $\tau_w > 0$ ).

It is obvious from the two plots in figure 8, that the developing boundary layer on the airfoil exhibits a dynamically rich response to small-amplitude pitch oscillations, with different key boundary layer characteristics controlling the dynamics of the flow in different phases of the pitch cycle. We identify some of the key boundary-layer characteristics to paint an over-all picture of the dynamics. A persistent trailing-edge separation can be identified in figure 8b beyond  $x/c > 0.8$ . The trailing-edge separation does not exhibit reverse flow 100% of the time, as can be seen from the white patches dispersed between largely black colored regions. An isolated separated region (distinct from the trailing edge separation) is observed at  $x/c \approx 0.6$  at times  $t/T_{osc} \approx 3$  and  $t/T_{osc} \approx 4$ . This is identified as a trailing-edge LSB. This LSB is short lived in time, existing for slightly less than a quarter of the pitch-cycle. A large separated region near the leading edge is a leading-edge LSB, similar to the

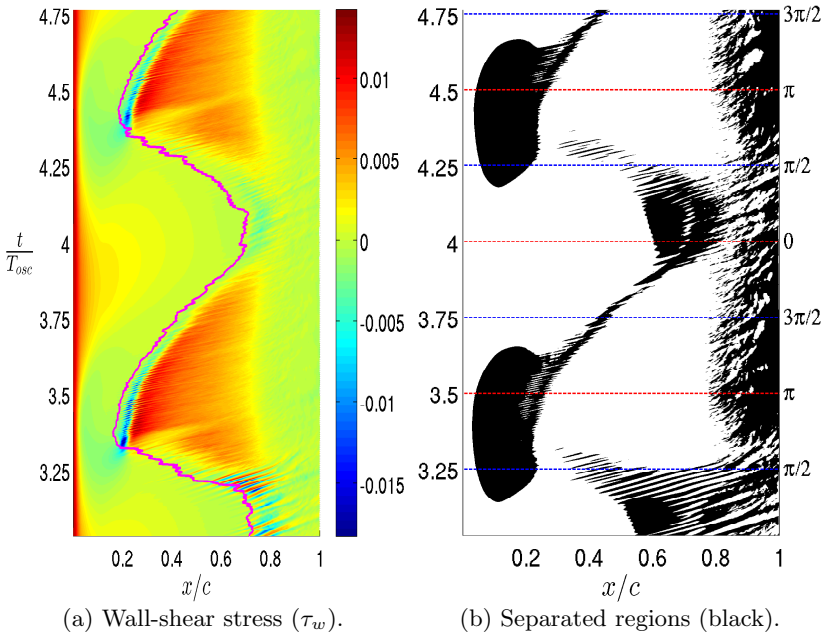


Figure 8: (a) Space-time plot for the wall-shear values ( $\tau_w$ ) and (b) separated flow regions. The values are obtained from the instantaneous flow averaged over the spanwise direction. Magenta line in (a) denotes the calculated transition location. Horizontal blue dashed lines in (b) represent the extrema of the angle of attack, while the red dashed lines represent phases corresponding to mean angle of attack.

one seen in the steady case at  $\alpha = 8.0^\circ$ . The separation bubble persists much longer in time, spanning nearly half a pitch cycle. Evident from figure 8a is that the transition point changes substantially throughout the pitch cycle. Interestingly, the flow over the airfoil differs significantly during the pitch-up and the pitch-down phases for the same angle of attack. For example, when the instantaneous angle of attack is at phase  $\phi = 0$  ( $t/T_{osc} = 3, 4$ ), which represents mean angle of attack but in the pitch-up phase, the flow over the airfoil is mostly laminar up to  $x/c \approx 0.7$ . On the other hand, for a phase of  $\phi = \pi$  ( $t/T_{osc} = 3.5, 4.5$ ), representing the airfoil at the mean angle of attack but in the pitch-down phase, the flow is almost entirely turbulent with the start of the turbulent region approximately at  $x/c \approx 0.22$ .

### 3.3. Transition location

In the present work we focus on the variation of transition location throughout the pitch cycles. Since the flow case is unsteady, and the transition location does not remain fixed, a criteria based on the instantaneous state of the flow is needed to determine the transition location. To this end, we calculate statistical

quantities which are averaged in the homogeneous spanwise direction, and also averaged for a short duration ( $\Delta t$ ) in time. This averaged value is considered as the “instantaneous” value for that quantity. Thus this instantaneous value of any statistical quantity  $\bar{q}(x, y, t)$  can be evaluated as in equation 3:

$$\bar{q}(x, y, t) = \left( \frac{1}{z_{max} - z_{min}} \right) \left( \frac{1}{\Delta t} \right) \int_{t'=t}^{t'=t+\Delta t} \int_{z=z_{min}}^{z=z_{max}} q(x, y, z, t') dz dt'. \quad (3)$$

Here  $(z_{max} - z_{min})$  is the spanwise extent of the computational domain. In order for such a quantity to be representative of the instantaneous state of the flow, the time duration of the averaging must be small. For the current case we use  $\Delta t = 4 \times 10^{-3}$ , which amounts to 0.06% of the oscillation time period during which the flow can be assumed to remain in approximately the same state. Using this procedure we evaluate the fluctuating Reynolds stress,  $\overline{u'v'}(x, y, t)$ , in order to determine the instantaneous transition location. The first streamwise location (on the suction-side) where the fluctuating Reynolds stress becomes larger than a certain threshold is denoted as the transition point. In order to prescribe a suitable threshold, the maximum value of  $|\overline{u'v'}|$  across the entire boundary layer is evaluated for all times. This maximum value does not exhibit large variations, remaining within the same order of magnitude for all times with its mean value being  $|\overline{u'v'}|_{max} \approx 0.05$ . The threshold for determining transition is set to 5% of this value. The transition point is thus the first point where  $|\overline{u'v'}| > 0.0025$ . Since we use an ad-hoc criterion for transition location, this is cross-checked by evaluating the variance of the spanwise velocity fluctuations  $\overline{w'w'}$ , and following an identical procedure as described above. In this case the transition criterion is prescribed as  $|\overline{w'w'}| > 0.005$  since the peak spanwise fluctuation intensities are found to be nearly twice the peak Reynolds stress  $|\overline{u'v'}|$ . Physically, growing spanwise velocity fluctuations indicate the onset of three-dimensionality in the boundary layer, which are associated with secondary instabilities. The temporal variation and the phase portrait of the calculated transition location using the aforementioned two criteria are shown in figure 9. The magenta line in figure 8 shows the calculated transition locations superposed on the space-time plot of the wall-shear stress. The calculated transition locations are consistent with the picture of wall-shear stress with transition marginally preceding regions of turbulent flow. While the thresholds specified may be considered ad-hoc, the qualitative picture of transition movement is not very sensitive to small changes in the threshold. Changing the thresholds by a factor of 2 still produces the same qualitative trends (not shown). Moreover, the time variation of transition point determined by two different physical quantities agree very well with each other. Thus we consider the quantities as a good representations of instantaneous flow characteristics.

The superposed plots in figure 8 indicate that the two LSBs play a dominating role in the flow dynamics and that transition location is governed by the characteristics of these LSBs. Figure 10 (left) shows the iso-contours of instantaneous vortical structures, identified by the  $\lambda_2$  method (Jeong & Hussain 1995), at four different times during the pitch-up cycle when the transition is

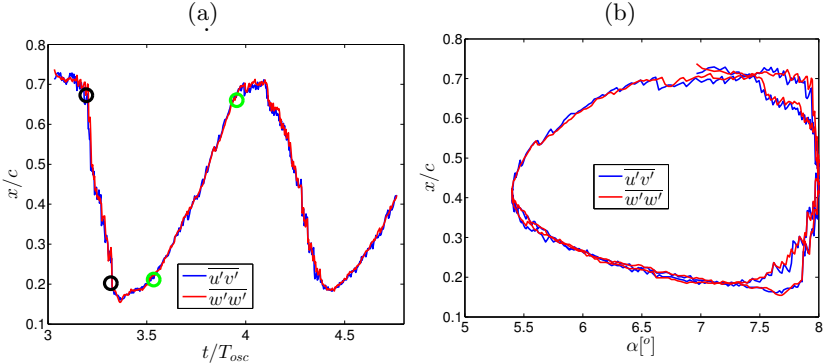


Figure 9: Time variation (a) and phase portrait with  $\alpha$  (b) of transition location evaluated using the criteria for  $|u'v'|$  and  $|w'w'|$ . The circles mark the points used to approximate the upstream (black circles) and downstream (green circles) velocities of the transition point.

moving upstream. This phase is marked by the appearance of a leading-edge LSB which grows in size. The top figure shows the flow state near the mean angle of attack ( $t/T_{osc} = 3.09$ ) during the pitch-up phase. The flow is mostly laminar across the airfoil with no structures observed prior to flow transition and there is no leading-edge LSB. The high adverse pressure gradient near the trailing edge causes the laminar flow to easily separate, forming a LSB and flow transitions over this separated shear layer. Figure 10 (left) from top to bottom shows the part of the oscillation cycle when transition is moving upstream at time instants of  $t/T_{osc} = 3.09, 3.2, 3.3$  and  $3.47$ . Note that pitch-up phase completes at  $t/T_{osc} = 3.25$  when the airfoil is at the highest angle of attack. Thus upstream movement of transition starts nearly at the end of the pitch-up phase and continues to move upstream even during the pitch-down cycle. The laminar separation bubble close to the trailing edge ceases to exist as transition moves upstream. At  $t/T_{osc} = 3.47$  the flow transition is seen to occur on the separated shear layer of the leading-edge LSB (bottom left in figure 10).

As the airfoil progresses through the pitch-down cycle the leading-edge LSB shrinks in size and the transition point then starts moving downstream, initiating the process of flow re-laminarization (figure 10 right, top to bottom). The leading-edge LSB eventually disappears, although the transition point moves downstream of the LSB before it completely disappears. The flow over the airfoil is not completely re-laminarized even when the airfoil is at the lowest angle of attack and the re-laminarization process continues into the pitch-up phase. There is a marked asymmetry between the upstream and downstream movement of the transition point. An approximate velocity for both the upstream and downstream motion of the transition point is calculated across the points marked by circles in figure 9a which correspond to transition movement with near constant velocity. The velocity of upstream transition

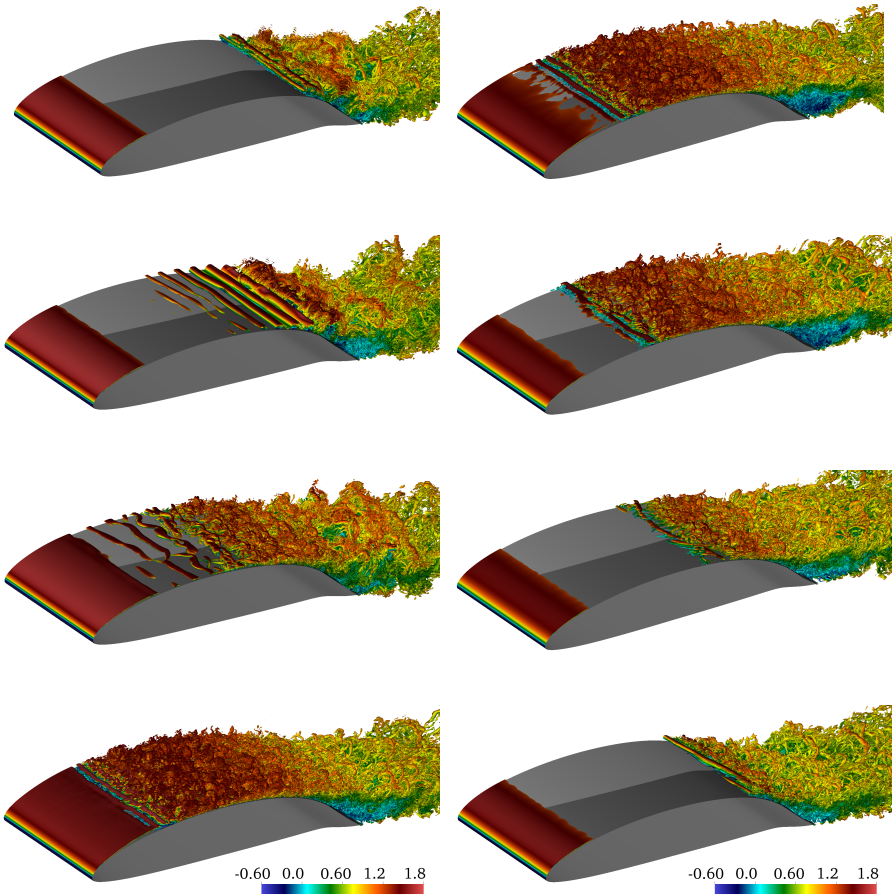


Figure 10: Visualization of instantaneous  $\lambda_2$  structures at different phases of the pitch cycle. The figures on the left are during the phase of the pitch cycle when the transition is moving upstream. From top to bottom the time-stamps of the instantaneous snapshots correspond to a normalized flow time of  $t/T_{osc} = 3.09, 3.2, 3.3, 3.47$ . On the right the instantaneous snapshot correspond to the re-laminarization phase as transition moves downstream. The time-stamps from top to bottom on the right correspond to  $t/T_{osc} = 3.55, 3.63, 3.82, 4.01$

movement is calculated across the black circles and is equal to  $V_u^{tr} = -0.60$  while the velocity of the downstream motion of transition is calculated across the green circles and is equal to  $V_d^{tr} = 0.17$ . Thus the upstream spread of turbulent regions is much faster than flow re-laminarization.

Specifying a velocity of transition movement implies that the transition location changes smoothly with time. This is true for the downstream movement

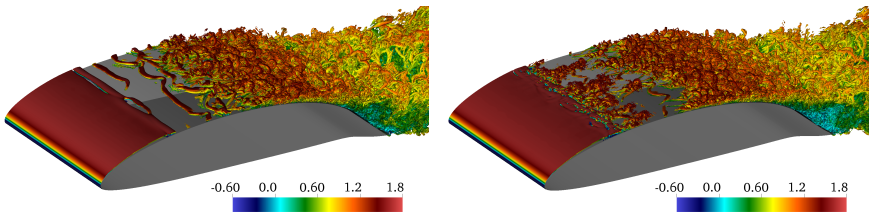


Figure 11: Comparison of boundary layer transition at two different time instants of  $t/T_{osc} = 3.33$  (left) and  $t/T_{osc} = 3.35$  (right).

of transition, however the final stages of the upstream movement appear to be more complex. Figure 11 shows the instantaneous vortical structures at two time instants during the upstream movement phase. In the left figure ( $t/T_{osc} = 3.33$ ) a single connected region of turbulence can be observed which is preceded by a laminar region identified by the near absence of small vortical structures. This region starts at about 40% and the entire boundary layer downstream is turbulent. On the right figure ( $t/T_{osc} = 3.35$ ) there is a similar large connected region of turbulence, spreading from approximately 40% of the chord. However there is also a nascent region of turbulence starting at  $x/c \approx 0.2$ . These two regions are separated by a patch of laminar flow. The figure on the right then has two distinct locations where transition to turbulence takes place. After a short while, turbulence spreads downstream from this newly formed transition location and eventually the entire boundary layer downstream is turbulent. This flow state, where two distinct turbulent regions can be identified exists only for a short duration and by  $t/T_{osc} = 3.4$  no intermediate regions of laminar flow can be identified. However the emergence of two distinct transition locations indicates that at least two competing mechanisms exist for the growth of disturbances in the boundary layer and that their relative strength changes during the pitch cycle. Given that this new transition occurs at the separated shear layer of the leading-edge LSB, the stability properties of the LSB are likely to play a role in the emergence of this new transition point.

### 3.4. Stability characteristics of the laminar separation bubble

The stability characteristics of the leading-edge LSB can help shed some light on the changing transition locations throughout the pitch cycle and in particular on the existence of competing mechanisms for transition. The competition between convective and absolute instability characteristics may provide a possible explanation for the transient existence of two distinct points of transition. The change of flow state from laminar to turbulent is often governed by the linear amplification of small disturbances within the boundary layer. For flows with streamwise and spanwise homogeneity the evolution of small perturbations

within the boundary layer is governed by the Orr-Sommerfeld equation

$$\left[ \left( \frac{\partial}{\partial t} + U \frac{\partial}{\partial x} \right) \nabla^2 - U'' \frac{\partial}{\partial x} - \frac{1}{Re} \nabla^4 \right] v = 0, \quad (4)$$

where  $v$  is wall-normal component of the velocity fluctuations and  $U''$  is the second derivative in the wall-normal direction of the streamwise velocity  $U$ . Due to Squire's theorem, analyzing the two-dimensional perturbations is sufficient to study the modal stability characteristics. Following Schmid & Henningson (2001) and assuming an ansatz function for the wall-normal perturbations as

$$v = \tilde{v}(y) e^{i(k_x x - \lambda t)}, \quad (5)$$

results in a dispersion relation between the complex frequency  $\lambda$  and the streamwise wavenumber  $k_x$  given by

$$\left[ (-i\lambda + ik_x U)(\mathcal{D}^2 - k_x^2) - ik_x U'' - \frac{1}{Re} (\mathcal{D}^2 - k_x^2)^2 \right] \tilde{v} = 0. \quad (6)$$

Here  $\mathcal{D}$  represents the derivative in the wall-normal ( $y$ ) direction. While strictly valid for homogeneous flows, the Orr-Sommerfeld equation has often been used for flows that exhibit weak inhomogeneity such as the Blasius boundary layer and also for the case of laminar separation bubbles (Alam & Sandham 2000; Hammond & Redekopp 1998; Häggmark *et al.* 2001). A temporal stability analysis using a real spatial wavenumber  $k_x$  results in an eigenvalue problem for the frequency  $\lambda$ . Resulting complex frequencies with a positive imaginary part signify that the boundary layer is unstable and that small perturbations within the boundary layer would grow in time and cause transition.

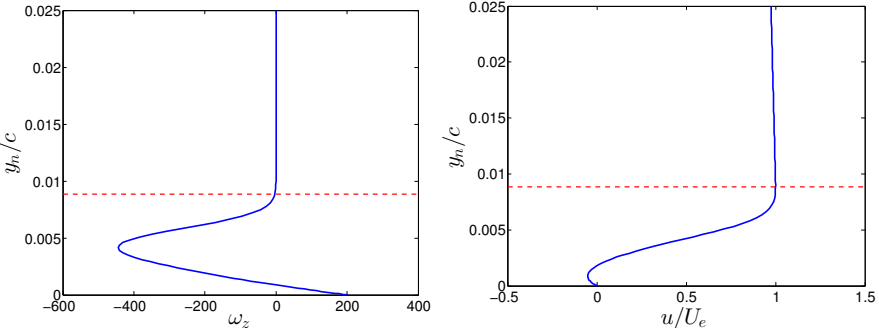


Figure 12: Wall-normal profiles of vorticity (left) and tangential velocity (right) observed in the leading-edge LSB at  $t/T_{osc} = 3.25$ . Dashed lines mark the boundary layer edge.  $t_n$  is the distance along the local wall-normal direction.

To explore the time varying stability properties of the LSB, temporal stability analysis of the Orr-Sommerfeld equations is performed using the instantaneous wall-normal profiles of tangential velocity, calculated as per equation 3. Several velocity profiles can be considered for local analysis. Alam & Sandham (2000) and Häggmark *et al.* (2001) in their local analysis associate

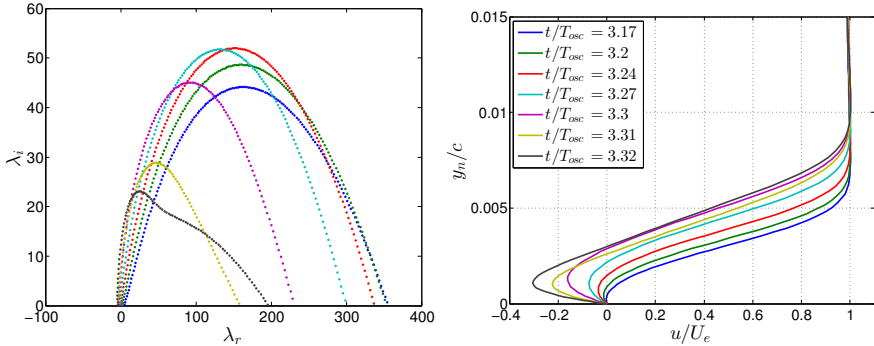


Figure 13: Unstable eigenvalues (left) obtained from a temporal stability analysis for different instantaneous velocity profiles (right).

the stability characteristics of the LSB with the maximum reverse flow intensities. In accordance with the previous studies, we focus on the wall-normal profiles of tangential velocity which exhibit the maximum reverse flow intensity relative to the boundary layer edge velocity. The edge velocity of the local profiles was determined using the criterion of vanishing spanwise vorticity *i.e.*  $\bar{\omega}_z \approx 0$ . Since there is a very small but finite amount of vorticity in the far-field due to the free-stream turbulence, the criterion for boundary layer height is set as the wall-normal distance where the vorticity decays to 1% of its maximum value in the boundary layer. Figure 12 shows the wall-normal profiles of tangential velocity and spanwise vorticity along with the evaluated height of the boundary layer.

Figure 13 shows the unstable complex frequencies obtained from the temporal stability analysis (with varying  $k_x$ ) for instantaneous profiles at several different time instants in the fourth pitch cycle. The reverse-flow intensity continues to increase with time until flow transition occurs at the LSB. The flow is unstable for all the analyzed velocity profiles as shown by the existence of complex frequencies with a positive imaginary part. However the highest amplification rate (frequency with maximum imaginary part) does not monotonically increase with reverse-flow intensity. At first the maximum amplification rate increases in time, but later it is seen to decrease. This changing characteristics can be associated with structural changes in the LSB, where at first the region of maximum reverse-flow is found near the center of the LSB, but as the LSB grows in size, this region of strong reverse flow moves closer to the downstream end of the LSB. Such qualitative changes in the shape of the LSB can be seen in figure 14. Structural changes in the LSB and its stability characteristics have previously been linked in the works of Theofilis *et al.* (2000); Cherubini *et al.* (2010) and Rodríguez & Theofilis (2010).

While the local stability analysis show that the boundary layer is unstable, an additional distinction needs to be made with regards to the nature of the instability which may be classified as either convective or absolute (Briggs 1964). The instability characteristics are usually elucidated using the simple concept of

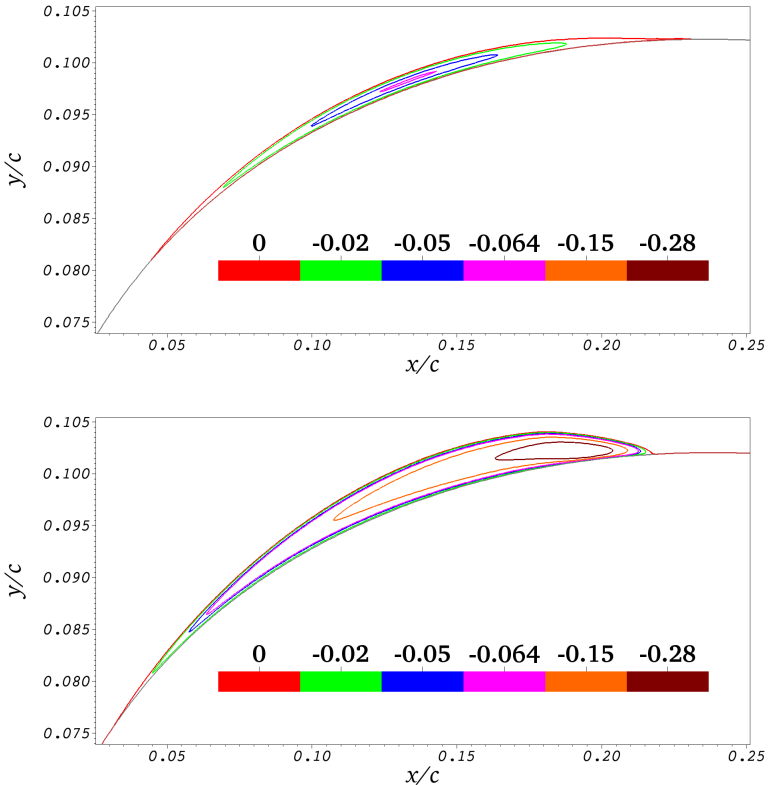


Figure 14: Contours of negative streamwise velocity in the leading-edge LSB at  $t/T_{osc} = 3.25$  (top) and  $t/T_{osc} = 3.32$  (bottom).

group velocity of perturbations,  $C_g$ . Growing perturbations that travel with a positive group velocity are deemed convectively unstable since they move away from the source of disturbance. On the other hand perturbations with zero group velocity are referred to as absolutely unstable, since they do not convect away from the origin of instability and create a self-sustaining process of perturbation growth. In the context of LSBs, high reverse-flow intensity has been associated with the presence of an absolute instability. Alam & Sandham (2000) with their local stability analysis of a two-parameter family of reverse flow profiles indicated that reverse flow intensities above 15% may cause the flow to be locally absolutely unstable. With a similar analysis on a three parameter family of profiles Hammond & Redekopp (1998) obtained onset of absolute instabilities at 20% reverse flow velocities. In the same study the authors also performed global stability analysis on a synthetically created boundary layer with a symmetric separation bubble and found the flow to be globally unstable for 30% reverse flow velocities. Figure 15 shows the absolute value of the maximum reverse flow intensity in the leading-edge LSB found in the present study. The reverse flow

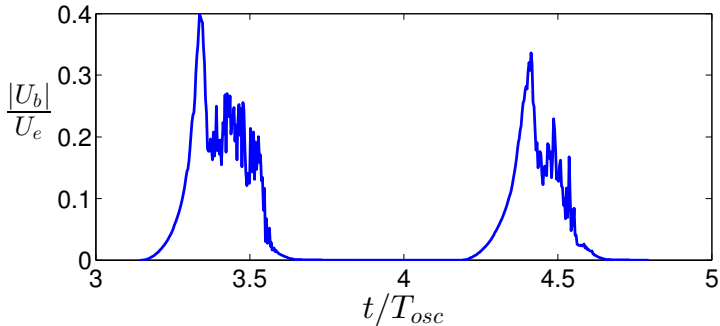


Figure 15: Ratio of maximum reverse flow ( $U_b$ ) in the leading-edge LSB to the boundary layer edge velocity ( $U_e$ ).

velocities are found to be higher than 30% in both the fourth and fifth pitch cycles, which is higher than the thresholds indicated by earlier investigators for absolute instability. In such a case it is likely that the leading-edge LSB changes character to become absolutely unstable during the pitch cycle. The change of characteristics may explain the simultaneous existence of two different transition points in the boundary layer. Initially when the reverse-flow intensity in the LSB is small, the flow is convectively unstable and perturbations grow while traveling downstream. Thus transition occurs downstream of the LSB. As the reverse-flow intensity becomes larger, the region of absolute instability may exist within the LSB which would cause perturbations to grow in time without being convected away. When these perturbations grow large they would cause transition over the LSB. Thus momentarily, there would be two distinct transition points, one due to the growth of absolute instabilities in the LSB and one due to convectively amplifying disturbances which cause transition downstream of the LSB.

To explore such a possibility, from the local stability analysis, one needs to identify unstable modes with zero group velocity. Briggs (1964) proposed a general method for the identification of absolute instabilities in a system which is commonly referred to as the Briggs method. The method involves solving the spatial stability problem for a range of complex  $\lambda$ , thus mapping contours on the complex frequency plane onto the complex wavenumber plane through the dispersion relation. Saddle points obtained in the complex wavenumber plane are the points where the dispersion relation has a double root. These points are known as the “pinch-points” in the complex wavenumber plane where the branches corresponding to the forward and backward propagating solutions of the dispersion relation meet via a double root. These pinch points correspond to perturbation modes that have zero group velocity. The mapping of the saddle-point on the frequency plane gives the absolute frequency  $\lambda^0$ . If this absolute frequency lies in the unstable half of the plane, then the system exhibits an absolute instability. Kupfer *et al.* (1987) proposed the inverse method called the cusp-map method, which maps contours in the complex wavenumber plane

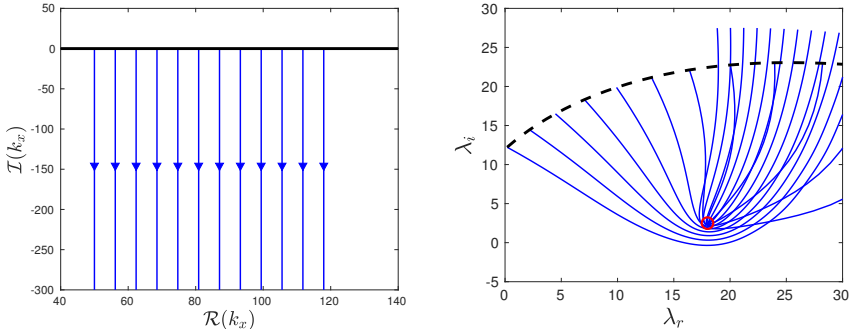


Figure 16: Contours on the complex wavenumber plane (left) and their corresponding mapping onto the complex frequency plane (right) at  $t/T_{osc} = 3.32$ . Figure on the right shows the unstable cusp associated with absolute instability, located at  $\lambda^0 = 18.02 + 2.46i$  (red circle). The dashed black line in the right figure corresponds to solutions of the Orr-Sommerfeld equation for real  $k_x$  (black line on the left).

on to the complex frequency plane via the dispersion relation and identified the absolute instability by locating the cusp in the complex frequency plane. This allowed for solving the simpler linear eigenvalue problem for  $\lambda$  rather than the non-linear eigenvalue problem for  $k_x$  in the Briggs method (Briggs 1964). Several contours need to be mapped from the wavenumber to the frequency plane for the location of the cusp. Kupfer *et al.* (1987) proposed mapping contours along lines with constant real part of  $k_x$ . Figure 16 and 17 show the cusps obtained in the complex frequency plane for the profiles with the highest reverse-flow intensity of tangential velocity. In the fourth cycle at  $t/T_{osc} = 3.32$  an unstable cusp is obtained with a positive absolute amplification rate of  $\lambda_i^0 = 2.46$ . On the other hand the cusp found in the fifth cycle is just marginally stable with an absolute amplification rate of  $\lambda_i^0 = -0.5$  at  $t/T_{osc} = 4.4$ . Since the velocity profiles considered here are averaged values instead of stationary base-flow profiles, it is possible that small temporal variation and/or non-linear modification of the flow hides the absolute instability properties when an averaged flow-field is considered. Nonetheless the results provide a strong indication that the LSB changes character to become absolutely unstable during the pitch cycle.

Caution needs to be taken in the interpretation of the stability analysis. The local stability analysis using the Orr-Sommerfeld equations assumes stationary homogeneous base state. Neither of which are strictly fulfilled when using the instantaneous, spanwise averaged velocity profiles. One can compare the properties of the LSB and the instability time-scales to judge the validity of such an analysis. The ratio of the time-period of the absolute instability ( $4^{th}$  cycle) to the time period of oscillation is 0.05, suggesting that the boundary layer would appear nearly stationary to the amplifying disturbances. For the spatial inhomogeneity, the ratio of the maximum boundary layer height to the length of the separation bubble can be used as an indicator. This ratio is

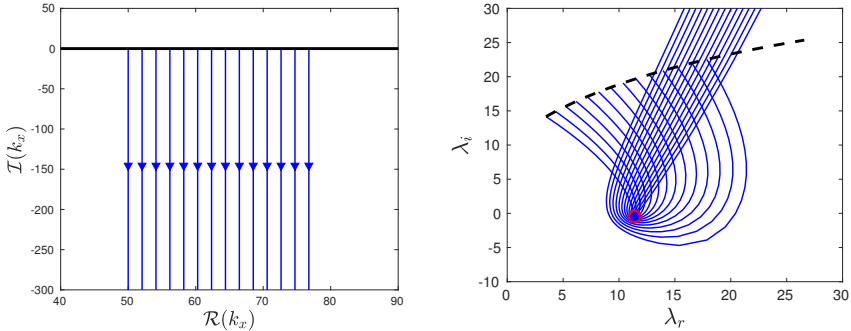


Figure 17: Contours on the complex wavenumber plane (left) and their corresponding mapping onto the complex frequency plane (right) at  $t/T_{osc} = 4.40$ . Figure on the right shows the marginally stable cusp located at located at  $\lambda^0 = 11.41 - 0.49i$  (red circle).

equal to  $\delta^{max}/L_x = 0.03$  which suggests a weak spatial inhomogeneity. Here  $\delta^{max}$  is the maximum value of the boundary layer height over the LSB and  $L_x$  is the spatial extent of the LSB. Both the above quantities indicate the quasi-steady, homogeneous flow assumptions may be used to obtain qualitative features of the flow case. The analysis then suggests that the convective instability properties of the boundary layer initially become stronger as the LSB grows in size. Structural changes occur in the LSB as it grows in size with regions of high reverse-flow moving to the end of the bubble. At high reverse-flow intensities the LSB changes character and exhibits a region of absolute instability. This can potentially explain the emergence of two distinct transition locations. The upstream transition would be caused by the temporally growing instabilities which amplify within the region of absolute instability without being convected downstream. On the other hand spatially growing waves associated with convective instabilities would trigger transition further downstream of the LSB. The emergence of the second transition point associated with absolute instabilities would cause abrupt changes in the boundary layer characteristics.

#### 4. Conclusion

A relaxation-term filtering procedure is used for wall-resolved LES of flow over a pitching airfoil. Validation of the LES procedure is done in a channel flow at  $Re_\tau = 395$  and for a wing section at  $Re_c = 400,000$  and the results show a good agreement with available DNS data sets.

Flow over an airfoil is simulated using the LES procedure at a chord based Reynolds number of  $Re_c = 100,000$  within an angle of attack range where the aerodynamic forces on the airfoil exhibit sensitive dependence on the angle of attack. This sensitive dependence is captured in the steady simulations at different angles of attack with large changes in transition location within a small variation of  $\alpha$ .

Pitch oscillations of the airfoil within this  $\alpha$  range of sensitive dependence displays a rich variety of unsteady flow phenomena. The flow goes through alternating periods of fully turbulent and laminar flow over the suction-side of the airfoil with different governing mechanisms for transition through the oscillating phases. When the flow is mostly laminar over the airfoil surface it separates easily under the effect of adverse pressure gradient, forming an LSB near the trailing-edge. Flow transition occurs over this separated shear layer. As the angle of attack increases, a leading-edge LSB is formed which first excites spatially growing waves (convective instability) causing transition downstream of the LSB. Initially the amplification rate of these spatially growing waves increases as the size of the LSB grows causing transition to move upstream. Eventually a region of absolute instability develops within the LSB and flow transition occurs abruptly on the separated shear layer. When transition is first triggered by this absolute instability mechanism the flow exhibits two distinct transition locations and abrupt changes in the boundary layer follow.

In the pitch-down cycle, the reverse phenomenon occurs where the leading-edge LSB shrinks in size and the region of absolute instability ceases to exist. The transition is then again governed by spatially amplifying waves. The spatial amplification rate now reduces as the LSB shrinks and transition moves downstream. The flow thus goes through states of convective and absolute instability, leading to constantly changing transition location. The upstream and downstream velocities of the transition point movement however are vastly different, with an average upstream velocity being around  $V_u^{tr} \approx -0.60$  and a much slower downstream velocity of  $V_d^{tr} \approx 0.17$ . This asymmetry is yet to be investigated, but may be an important parameter in unsteady turbulence modeling.

## Acknowledgement

The computations were performed on resources provided by the Swedish National Infrastructure for Computing (SNIC) at the PDC Center for High Performance Computing at the Royal Institute of Technology (KTH). Simulation have also been performed at the Barcelona Supercomputing Center, Barcelona, with computer time provided by the 12<sup>th</sup> PRACE Project Access Call (number 2015133182). The work was partially funded by European Research Council under grant agreement 694452-TRANSEP-ERC-2015-AdG. The work was also partially funded by Vinnova through the NFFP project UMTAPS, with grant number 2014-00933. We would like to thank Dr. David Eller and Dr. Mikaela Lokatt for providing us with the NLF design and the numerous discussions on different aerodynamic aspects of the project.

## REFERENCES

- ALAM, M. & SANDHAM, N. D. 2000 Direct numerical simulation of 'short' laminar separation bubbles with turbulent reattachment. *Journal of Fluid Mechanics* **410**, 1–28.

- ALFEREZ, N., MARY, I. & LAMBALLAIS, E. 2013 Study of stall development around an airfoil by means of high fidelity large eddy simulation. *Flow, Turbulence and Combustion* **91** (3), 623–641.
- BRANDT, L., SCHLATTER, P. & HENNIGSON, D. S. 2004 Transition in boundary layers subject to free-stream turbulence. *Journal of Fluid Mechanics* **517**.
- BRIGGS, R. J. 1964 *Electron-Stream Interaction with Plasmas*. The MIT Press, Cambridge, Massachusetts.
- CARR, L. W., MCALISTER, K. W. & MCCROSKEY, W. J. 1977 Analysis of the development of dynamic stall based on oscillating airfoil experiments. *Tech. Rep.* NASA Ames Research Center; Moffett Field, CA, United States.
- CHERUBINI, S., ROBINET, J.-C. & PALMA, P. D. 2010 The effects of non-normality and nonlinearity of the navier-stokes operator on the dynamics of a large laminar separation bubble. *Physics of Fluids* **22** (1), 014102.
- CHIN, C., NG, H., BLACKBURN, H., MONTY, J. & OOI, A. 2015 Turbulent pipe flow at  $Re_\tau = 1000$ : A comparison of wall-resolved large-eddy simulation, direct numerical simulation and hot-wire experiment. *Computers and Fluids* **122**, 26 – 33.
- CHOUDHRY, A., LEKNYS, R., ARJOMANDI, M. & KELSO, R. 2014 An insight into the dynamic stall lift characteristics. *Experimental Thermal and Fluid Science* **58**, 188 – 208.
- COORKE, T. C. & THOMAS, F. O. 2015 Dynamic stall in pitching airfoils: Aerodynamic damping and compressibility effects. *Annual Review of Fluid Mechanics* **47** (1), 479–505.
- DONG, S., KARNIADAKIS, G. E. & CHRYSOSTOMIDIS, C. 2014 A robust and accurate outflow boundary condition for incompressible flow simulations on severely-truncated unbounded domains. *Journal of Computational Physics* **261**, 83–105.
- DRELA, M. 1989 *XFOIL: An Analysis and Design System for Low Reynolds Number Airfoils*, pp. 1–12. Berlin, Heidelberg: Springer Berlin Heidelberg.
- DUNNE, R. & McKEON, B. J. 2015 Dynamic stall on a pitching and surging airfoil. *Experiments in Fluids* **56** (8), 157.
- EITEL-AMOR, G., ÖRLÜ R. & SCHLATTER, P. 2014 Simulation and validation of a spatially evolving turbulent boundary layer up to  $Re_\theta = 8300$ . *International Journal of Heat and Fluid Flow* **47**, 57–69.
- ERICSSON, L. & REDING, J. 1988a Fluid mechanics of dynamic stall part i. unsteady flow concepts. *Journal of Fluids and Structures* **2** (1), 1 – 33.
- ERICSSON, L. & REDING, J. 1988b Fluid mechanics of dynamic stall part ii. prediction of full scale characteristics. *Journal of Fluids and Structures* **2** (2), 113 – 143.
- FISCHER, P. F., LOTTES, J. W. & KERKEMEIER, S. G. 2008 Nek5000 web page. <http://nek5000.mcs.anl.gov>.
- HÄGGMARK, C. P., HILDINGS, C. & HENNIGSON, D. S. 2001 A numerical and experimental study of a transitional separation bubble. *Aerospace Science and Technology* **5** (5), 317–328.
- HAMMOND, D. & REDEKOPP, L. 1998 Local and global instability properties of separation bubbles. *European Journal of Mechanics - B/Fluids* **17** (2), 145 – 164.
- HEBLER, A., SCHOJDA, L. & MAI, H. 2013 Experimental investigation of the aeroelastic behavior of a laminar airfoil in transonic flow. In *Proceedings IFASD*.
- HO, L.-W. & PATERA, A. T. 1990 A Legendre spectral element method for simulation

- of unsteady incompressible viscous free-surface flows. *Computer Methods in Applied Mechanics and Engineering* **80** (1), 355 – 366.
- HO, L.-W. & PATERA, A. T. 1991 Variational formulation of three-dimensional viscous free-surface flows: Natural imposition of surface tension boundary conditions. *International Journal for Numerical Methods in Fluids* **13** (6), 691–698.
- HOSSEINI, S. M., VINUESA, R., SCHLATTER, P., HANIFI, A. & HENNINGSON, D. S. 2016 Direct numerical simulation of the flow around a wing section at moderate Reynolds number. *International Journal of Heat and Fluid Flow* **61**, 117 – 128.
- JEONG, J. & HUSSAIN, F. 1995 On the identification of a vortex. *Journal of Fluid Mechanics* **285**.
- KLEUSBERG, E. 2017 Wind turbine simulations using spectral elements. Licentiate thesis, Royal Institute of Technology (KTH), Stockholm, Sweden.
- KUPFER, K., BERS, A. & RAM, A. K. 1987 The cusp map in the complex-frequency plane for absolute instabilities. *The Physics of Fluids* **30** (10), 3075–3082.
- LANGTRY, R. B. & MENTER, F. R. 2009 Correlation-Based Transition Modeling for Unstructured Parallelized Computational Fluid Dynamics Codes. *AIAA Journal* **47**, 2894–2906.
- LOKATT, M. 2017 On aerodynamic and aeroelastic modeling for aircraft design. Doctoral thesis, KTH Royal Institute of Technology.
- LOKATT, M. & ELLER, D. 2017 Robust viscous-inviscid interaction scheme for application on unstructured meshes. *Computers & Fluids* **145**, 37 – 51.
- LOMBARD, J.-E. W., MOXLEY, D., SHERWIN, S. J., HOESSLER, J. F. A., DHANDAPANI, S. & TAYLOR, M. J. 2016 Implicit Large-Eddy Simulation of a Wingtip Vortex. *AIAA Journal* **54**, 506–518.
- MADAY, Y. & PATERA, A. T. 1989 Spectral element methods for the incompressible Navier-Stokes equations. In *State-of-the-art surveys on computational mechanics (A90-47176 21-64)*. New York, American Society of Mechanical Engineers, 1989, p. 71-143. Research supported by DARPA., pp. 71–143.
- MAI, H. & HEBLER, A. 2011 Aeroelasticity of a laminar wing. In *Proceedings IFASD*. Paris.
- MCCROSKEY, W. J. 1973 Inviscid flowfield of an unsteady airfoil. *AIAA Journal* **11** (8), 1130 – 1137.
- MCCROSKEY, W. J. 1981 Phenomenon of dynamic stall. *Tech. Rep.*. NASA Ames Research Center; Moffett Field, CA, United States.
- MCCROSKEY, W. J. 1982 Unsteady airfoils. *Annual Review of Fluid Mechanics* **14** (1), 285–311.
- MCCROSKEY, W. J., CARR, L. W. & MCALISTER, K. W. 1976 Dynamic stall experiments on oscillating airfoils. *AIAA Journal* **14** (1), 57 – 63.
- MCCROSKEY, W. J., MCALISTER, K. W., CARR, L. W. & PUCCI, S. L. 1982 An experimental study of dynamic stall on advanced airfoil sections. volume 1: Summary of the experiment. *Tech. Rep.*. NASA Ames Research Center, Moffett Field, CA, United States.
- MOSER, R. D., KIM, J. & MANSOUR, N. N. 1999 Direct numerical simulation of turbulent channel flow up to  $Re_\tau = 590$ . *Physics of Fluids* **11** (4), 943–945.
- NATI, A., DE KAT, R., SCARANO, F. & VAN OUDHEUSDEN, B. W. 2015 Dynamic pitching effect on a laminar separation bubble. *Experiments in Fluids* **56** (9), 172.

- PASCAZIO, M., AUTRIC, J., FAVIER, D. & MARESCA, C. 1996 Unsteady boundary-layer measurement on oscillating airfoils-transition and separation phenomena in pitching motion. In *34th Aerospace Sciences Meeting and Exhibit*, p. 35.
- RIVAL, D. & TROPEA, C. 2010 Characteristics of pitching and plunging airfoils under dynamic-stall conditions. *Journal of Aircraft* **47** (1), 80–86.
- RODRÍGUEZ, D. & THEOFILIS, V. 2010 Structural changes of laminar separation bubbles induced by global linear instability. *Journal of Fluid Mechanics* **655**, 280–305.
- ROSTI, M. E., OMIDYEGANEH, M. & PINELLI, A. 2016 Direct numerical simulation of the flow around an aerofoil in ramp-up motion. *Physics of Fluids* **28** (2), 025106.
- SCHLATTER, P. 2001 Direct numerical simulation of laminar-turbulent transition in boundary layer subject to free-stream turbulence. Diploma thesis, Royal Institute of Technology (KTH), Stockholm, Sweden.
- SCHLATTER, P., BRANDT, L., DE LANGE, H. C. & HENNINSON, D. S. 2008 On streak breakdown in bypass transition. *Physics of Fluids* **20** (10), 101505.
- SCHLATTER, P., STOLZ, S. & KLEISER, L. 2004 LES of transitional flows using the approximate deconvolution model. *International Journal of Heat and Fluid Flow* **25** (3), 549 – 558, turbulence and Shear Flow Phenomena (TSFP-3).
- SCHLATTER, P., STOLZ, S. & KLEISER, L. 2006a *Analysis of the SGS energy budget for deconvolution- and relaxation-based models in channel flow*, pp. 135–142. Dordrecht: Springer Netherlands.
- SCHLATTER, P., STOLZ, S. & KLEISER, L. 2006b Large-eddy simulation of spatial transition in plane channel flow. *Journal of Turbulence* **7**, N33.
- SCHMID, P. J. & HENNINSON, D. S. 2001 *Stability and Transition in Shear Flows*. Springer.
- THEODORSEN, T. 1935 General theory of aerodynamic instability and the mechanism of flutter. *Tech. Rep.* National Advisory Committee for Aeronautics; Langley Aeronautical Lab.; Langley Field, VA, United States.
- THEOFILIS, V., HEIN, S. & DALLMANN, U. 2000 On the origins of unsteadiness and three-dimensionality in a laminar separation bubble. *Philosophical Transactions of the Royal Society of London A: Mathematical, Physical and Engineering Sciences* **358** (1777), 3229–3246.
- UZUN, A. & HUSSAINI, M. Y. 2010 Simulations of vortex formation around a blunt wing tip. *AIAA Journal* **48**, 1221–1234.
- VISBAL, M. R. 2011 Numerical investigation of deep dynamic stall of a plunging airfoil. *AIAA Journal* **49** (10), 2152 – 2170.
- VISBAL, M. R. 2014 Analysis of the onset of dynamic stall using high-fidelity large-eddy simulations. In *52nd Aerospace Sciences Meeting, AIAA SciTech Forum*. AIAA.
- VISBAL, M. R. & GARMANN, D. J. 2017 Numerical investigation of spanwise end effects on dynamic stall of a pitching naca 0012 wing. In *55th AIAA Aerospace Sciences Meeting, AIAA SciTech Forum*. AIAA.

# Paper 4

4



# High-fidelity simulations of the flow around wings at high Reynolds numbers

R. Vinuesa, P. S. Negi, A. Hanifi, D. S. Henningson and P. Schlatter

Department of Mechanics, Linné FLOW Centre and Swedish e-Science Research Centre (SeRC), KTH Royal Institute of Technology, SE-100 44 Stockholm, Sweden

*In Proc. 10<sup>th</sup> Int. Sym. on Turbulence & Shear Flow Phenomenon (TSFP-10)*

Reynolds-number effects in the adverse-pressure-gradient (APG) turbulent boundary layer (TBL) developing on the suction side of a NACA4412 wing section are assessed in the present work. To this end, we conducted a well-resolved large-eddy simulation of the turbulent flow around the NACA4412 airfoil at a Reynolds number based on freestream velocity and chord length of  $Re_c = 1,000,000$ , with  $5^\circ$  angle of attack. The results of this simulation are used, together with the direct numerical simulation by Hosseini *et al.* (Int. J. Heat Fluid Flow **61**, 2016) of the same wing section at  $Re_c = 400,000$ , to characterize the effect of Reynolds number on APG TBLs subjected to the same pressure-gradient distribution (defined by the Caluser pressure-gradient parameter  $\beta$ ). Our results indicate that the increase in inner-scaled edge velocity  $U_e^+$ , and the decrease in shape factor  $H$ , is lower in the APG on the wing than in zero-pressure-gradient (ZPG) TBLs over the same Reynolds-number range. This indicates that the lower- $Re$  boundary layer is more sensitive to the effect of the APG, a conclusion that is supported by the larger values in the outer region of the tangential velocity fluctuation profile in the  $Re_c = 400,000$  wing. Future extensions of the present work will be aimed at studying the differences in the outer-region energizing mechanisms due to APGs and increasing Reynolds number.

**Key words:** adverse pressure-gradient, boundary-layer, wings

---

## 1. Introduction

Turbulent boundary layers (TBLs) subjected to streamwise pressure gradients (PGs) are relevant to a wide range of industrial applications from diffusers to turbines and wings, and pose a number of open questions regarding their structure and underlying dynamics. A number of studies over the years have aimed at shedding some light on these open questions from the theoretical (Townsend 1956; Mellor & Gibson 1966), experimental (Skåre & Krogstad 1994; Harun *et al.* 2013) and numerical (Spalart & Watmuff 1993; Skote *et al.* 1998)

perspectives, but the large number of parameters influencing the structure of PG TBLs raises serious difficulties when comparing databases from different experimental or numerical databases (Monty *et al.* 2011). The current work is focused on the analysis of adverse-pressure-gradient (APG) effects on TBLs, a flow case that can be observed, for instance, on the suction side of wings. As the boundary layer develops, it encounters a progressively larger resistance manifested in the increased pressure in the streamwise direction. This APG decelerates the boundary layer, increases its wall-normal momentum, and increases its thickness while reducing the wall-shear stress. As a result of the larger boundary-layer thickness the wake parameter in the mean velocity profile increases (Vinuesa *et al.* 2014), and more energetic turbulent structures develop in the outer region (Maciel *et al.* 2017). The recent work by Bobke *et al.* (2017) highlights the importance of the flow development in the establishment of an APG TBL, and in particular the streamwise evolution of the Clauser pressure-gradient parameter  $\beta = \delta^*/\tau_w dP_e/dx$  (where  $\delta^*$  is the displacement thickness,  $\tau_w$  the wall-shear stress and  $dP_e/dx$  is the streamwise pressure gradient). In their study, Bobke *et al.* (2017) compared different APG TBLs subjected to various  $\beta(x)$  distributions, including several flat-plate cases and one APG developing on the suction side of a wing section (Hosseini *et al.* 2016). Their main conclusion was the fact that the effect of APGs was more prominent in the cases where the boundary layer had been subjected to a stronger pressure gradient for a longer streamwise distance, a conclusion that demonstrates the relevance of accounting for the  $\beta(x)$  distribution when assessing pressure-gradient effects on TBLs. Along these lines, the numerical studies by Kitsios *et al.* (2016), Lee (2017) and Bobke *et al.* (2017) aim at characterizing the effect of APGs on TBLs in cases with a constant pressure-gradient magnitude, *i.e.*, in flat-plate boundary layers exhibiting long regions with constant values of  $\beta$ . The aim of the present work is to assess the effect of the Reynolds number ( $Re$ ) on two APG TBLs subjected to the same  $\beta(x)$ . In particular, we consider the turbulent flow around a NACA4412 wing section at two Reynolds numbers based on freestream velocity  $U_\infty$  and chord length  $c$ , namely  $Re_c = 400,000$  and  $1,000,000$ . As discussed below, the  $\beta(x)$  distribution is almost identical in the two cases, a fact that allows to characterize the impact of  $Re$  on the boundary-layer development. The former database is a the direct numerical simulation (DNS) by Hosseini *et al.* (2016), whereas the latter is a well-resolved large-eddy simulation (LES) conducted in the current study, and described in the next section.

## 2. Computational setup

A well-resolved LES of the flow around a NACA4412 wing section was carried out using the spectral-element code Nek5000 (Fischer *et al.* 2008), developed at Argonne National Laboratory. In the spectral-element method (SEM) the computational domain is decomposed into elements, where the velocity and pressure fields are expressed in terms of high-order Lagrange interpolants of Legendre polynomials, at the Gauss–Lobatto–Legendre (GLL) quadrature points.

In the present work we used the  $\mathbb{P}_N - \mathbb{P}_{N-2}$  formulation, which implies that the velocity and pressure fields are expressed in terms of polynomials of order  $N$  and  $N - 2$ , respectively. The time discretization is based on an explicit third-order extrapolation for the nonlinear terms, and an implicit third-order backward differentiation for the viscous ones. The code is written in Fortran 77 and C and the message-passing-interface (MPI) is used for parallelism. We have used Nek5000 to simulate wall-bounded turbulent flows in moderately complex geometries in a wide range of internal (Marin *et al.* 2016) and external (Vinuesa *et al.* 2015) configurations.

A two-dimensional slice of the computational domain is shown in Figure 1 (left), where  $x$ ,  $y$  and  $z$  denote the horizontal, vertical and spanwise directions, respectively. The domain is periodic in the spanwise direction, with a width of  $L_z = 0.2c$ . A total of 4.5 million spectral elements was used to discretize the domain with a polynomial order  $N = 7$ , which amounts to a total of 2.3 billion grid points. As in the DNS simulation by Hosseini *et al.* (2016), a Dirichlet boundary condition extracted from an initial RANS (Reynolds-Averaged Navier-Stokes) simulation was imposed on all the boundaries except the outflow, where the boundary condition by Dong *et al.* (2014) was employed. The initial RANS simulation was carried out with the  $k - \omega$  SST (shear-stress transport) model (Menter 1994) implemented in the commercial software ANSYS Fluent. In the current configuration, a Reynolds number of  $Re_c = 1,000,000$  was considered, together with an angle of attack of  $5^\circ$ . The LES approached is based on a relaxation-term (RT) filter, which provides an additional dissipative force in order to account for the contribution of the smallest, unresolved, turbulent scales (Schlatter *et al.* 2004). A validation of the method in turbulent channel flows and the flow around a NACA4412 wing section is given by Negi *et al.* (2017). The mesh resolution around the wing follows these guidelines:  $\Delta x^+ < 27$ ,  $\Delta y_{\text{wall}}^+ < 0.96$  and  $\Delta z^+ < 13$ , where the superscript ‘ $+$ ’ denotes scaling in terms of the friction velocity  $u_\tau = \sqrt{\tau_w/\rho}$  (with  $\rho$  being the fluid density). Regarding the wake, we defined the criterion  $\Delta x/\eta < 13$ , where  $\eta = (\nu^3/\varepsilon)^{1/4}$  is the Kolmogorov scale ( $\nu$  is the fluid kinematic viscosity, and  $\varepsilon$  the local isotropic dissipation). An instantaneous flow field showing the coherent structures identified with the  $\lambda_2$  method (Jeong & Hussain 1995) is shown in Figure 1 (right), which also highlights the adequacy of the present LES approach to simulate this flow. Note that the boundary layers on the suction and pressure sides were tripped using the volume-force method described by Schlatter & Örlü (2012).

### 3. Results and discussion

As discussed in the introduction, the aim of the current study is to investigate the Reynolds-number effects on APG TBLs subjected to the same  $\beta(x)$  distribution. In particular, we aim at assessing such effects on the turbulent boundary layer developing on the suction side (denoted as  $ss$ ) of a NACA4412 wing section with  $5^\circ$  angle of attack. To this end, we compare the results from the DNS database

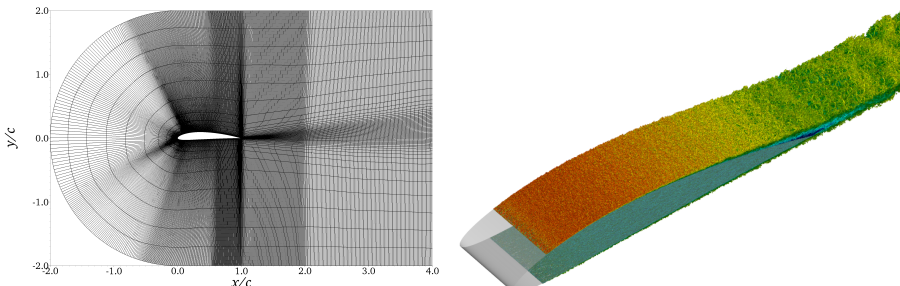


Figure 1: (Left) Two-dimensional slice of the computational domain showing the spectral-element distribution, but not the individual GLL points. (Right) Instantaneous flow field showing coherent structures identified with the  $\lambda_2$  method (Jeong & Hussain 1995), and colored with horizontal velocity. In this figure, dark blue represents a horizontal velocity of  $-0.1$  and dark red a value of  $2$ .

at  $Re_c = 400,000$  by Hosseini *et al.* (2016) with the current well-resolved LES at  $Re_c = 1,000,000$ . The turbulence statistics presented in this study for the  $Re_c = 1,000,000$  case were obtained after averaging for one flow-over time (where the time is non-nondimensionalized in terms of  $U_\infty$  and  $c$ ). Note that the spanwise width of the current simulation is twice as large as the one considered by Hosseini *et al.* (2016), a fact that effectively increases the statistical samples by a factor of two. Although this averaging period does not allow to obtain converged turbulent kinetic energy (TKE) budgets, the mean and fluctuating profiles discussed here start to exhibit convergence up to  $x_{ss}/c \simeq 0.7$ . The boundary-layer development, mean velocity and Reynolds-stress profiles are discussed in the next sections.

### 3.1. Boundary-layer development

In Figure 2 (top left) we show the streamwise evolution of the Clauer pressure-gradient parameter  $\beta$  for the TBLs on the suction side of the two wing cases under study. As expected, the two boundary layers are subjected to almost identical  $\beta(x)$  distributions, with small relative differences only arising beyond  $x_{ss}/c > 0.9$ . Note that the boundary layers are subjected to conditions close to zero pressure gradient (ZPG) up to  $x_{ss}/c \simeq 0.3$ , point after which the value of  $\beta$  increases beyond 0.1. In the next section we will study the velocity profiles at  $x_{ss}/c = 0.4$  and  $0.7$ , in which the pressure-gradient magnitude is moderate ( $\beta \simeq 0.6$ ) and strong ( $\beta \simeq 2$ ), respectively. Although the value of  $\beta$  increases throughout the whole suction side of the wing, an inflection point is observed at  $x_{ss}/c = 0.4$ , which is the point of maximum camber in the NACA4412 airfoil. Beyond this point, the rate of change of  $\beta$  increases significantly with  $x$ , a fact that is explained by the progressive reduction in airfoil thickness, which produces a larger increase in streamwise adverse pressure gradient.

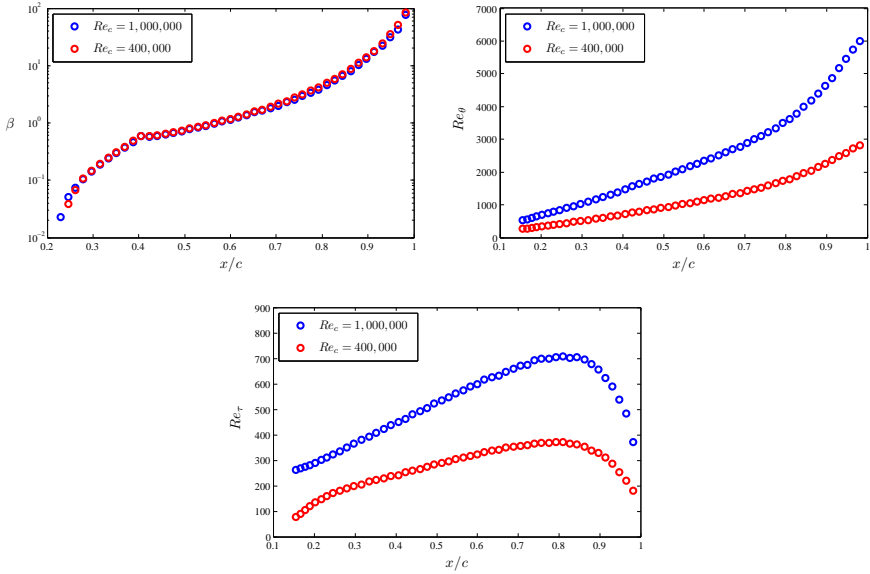


Figure 2: Streamwise evolution of (top left) the Clauser pressure-gradient parameter  $\beta$ , (top right) the Reynolds number based on momentum thickness  $Re_\theta$  and (bottom) the friction Reynolds number  $Re_\tau$ , for the two wing cases under study.

In Figure 2 (top right) and (bottom) we show the streamwise evolution of the Reynolds number based on momentum thickness  $Re_\theta$ , and the friction Reynolds number  $Re_\tau = \delta_{99} u_\tau / \nu$ , respectively. Note that  $\delta_{99}$  is the 99% boundary-layer thickness, which was determined following the method described by Vinuesa *et al.* (2016) for pressure-gradient TBLs. The  $Re_\theta$  trends increase monotonically in the two boundary layers, due to the fact that both Reynolds number and APG promote the increase of the boundary-layer thickness. In particular, the thickening experienced by the TBLs due to the APG significantly increases  $Re_\theta$  in both cases, up to a maximum value of 2,800 in the  $Re_c = 400,000$  case, and up to  $Re_\theta = 6,000$  in the higher- $Re_c$  wing, both observed close to the trailing edge. Regarding the friction Reynolds number, note that in the two boundary-layer cases the maximum is located at  $x_{ss}/c \simeq 0.8$ , and not close to the trailing edge as in  $Re_\theta$ . This is due to the fact that, although the APG increases the boundary-layer thickness, it also decreases the wall-shear stress; thus, the very strong APGs beyond  $x_{ss}/c \simeq 0.8$  (where  $\beta \simeq 4.1$  in both cases) produce a larger reduction in  $u_\tau$  than the increase in  $\delta_{99}$ . The maximum  $Re_\tau$  values are 373 and 707 in the  $Re_c = 400,000$  and 1,000,000 wings, respectively.

The skin-friction coefficient  $C_f = 2(u_\tau/U_e)^2$  (where  $U_e$  is the velocity at the boundary-layer edge) and the shape factor  $H = \delta^*/\theta$  are shown, as a function of the streamwise position on the suction side of the wing, in Figure 3. The

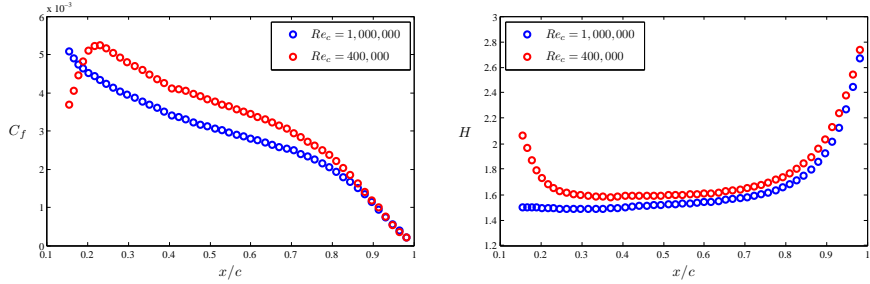


Figure 3: Streamwise evolution of (left) the skin-friction coefficient  $C_f$  and (right) the shape factor  $H$ , for the two wing cases under study.

$C_f$  curves show different trends up to  $x_{ss}/c \simeq 0.2$ , a fact that is explained by the volume-force tripping at  $x_{ss}/c = 0.1$ . In the present high- $Re$  case, the tripping parameters were chosen following the work by Schlatter & Örlü (2012) in ZPG TBLs; however, in the  $Re_c = 400,000$  wing the number of modes in the spanwise direction was larger than in Schlatter & Örlü (2012), a fact that produces a long intermittent region in the post-transitional region. Nevertheless, the boundary layers can be considered to be essentially independent of the tripping beyond  $x_{ss}/c \simeq 0.2$  (Vinuesa *et al.* 2016). It can be observed that the  $C_f$  curve in the high- $Re$  wing is below the one of the lower- $Re$  case up to  $x_{ss}/c \simeq 0.9$ , point after which the differences between both curves are significantly reduced. Since the two boundary layers are subjected to the same  $\beta(x)$  distribution, it can be argued that the differences between both curves are due to Reynolds-number effects, a fact that is consistent with what is observed in ZPG TBLs since  $C_f$  decreases with  $Re$ . Interestingly, the effect of Reynolds number becomes essentially negligible beyond  $x_{ss}/c \simeq 0.9$ , where the very strong APG conditions (with a value of  $\beta \simeq 14$  at  $x_{ss}/c = 0.9$ ) define the state of the boundary layer. Regarding the shape factor, note that APG and Reynolds number have opposite effects on a TBL: whereas the former increases  $H$  (due to the thickening of the boundary layer caused by the increased wall-normal momentum), the latter decreases the shape factor. This can also be observed in Figure 3 (right), where the  $H$  curve from the  $Re_c = 1,000,000$  is below the one from the  $Re_c = 400,000$  throughout the whole suction side of the wing. Note that, since the two boundary layers are subjected to essentially the same pressure-gradient effects, the lower values of  $H$  are produced by the higher Reynolds number. The differences between the effects of  $\beta$  and  $Re$  on TBLs are further discussed in the next section.

### 3.2. Inner-scaled mean velocity and Reynolds-stress profiles

Figure 4 shows the inner-scaled mean velocity profiles at  $x_{ss}/c = 0.4$  and  $0.7$  for the wing cases, where in the former the value of  $\beta$  is around 0.6 and in the latter  $\beta \simeq 2$ . Note that  $U_t^+$  is the inner-scaled mean velocity in the direction tangential to the wing surface, whereas  $y_n^+$  is the inner-scaled wall-normal

coordinate. In Figure 4 (left) we show the two wing profiles, with  $Re_\tau = 242$  and 449, together with ZPG TBL profiles at matched  $Re_\tau$  obtained from the DNS database by Schlatter & Örlü (2010). These comparisons are aimed at assessing the effect of the APG with respect to the baseline ZPG case, and although this comparison can be done by matching several quantities (such as  $Re_{\delta^*}$  or  $Re_\theta$ ), in the present work we fixed  $Re_\tau$  as in the studies by Monty *et al.* (2011), Harun *et al.* (2013) or Bobke *et al.* (2017). Note that by fixing  $Re_\tau$  we compare two boundary layers which essentially exhibit the same range of spatial scales, but subjected to different pressure-gradient conditions. The first noticeable conclusion is the more prominent wakes present in the APG TBLs compared with the corresponding ZPG TBLs at the same  $Re_\tau$ , which is due to the lower skin-friction coefficient caused by the boundary-layer thickening due to the APG. A first step towards characterizing the effect of  $Re$  in the TBLs subjected to this particular  $\beta(x)$  distribution is to observe the evolution of  $U_e^+$  between  $Re_\tau = 242$  and 449 in the ZPG and in the APG cases: in the former, the increase in the inner-scaled edge velocity is 11%, whereas in the latter it is 9.7%. On the other hand, the decrease in  $H$  is 3.1% in the ZPG boundary layers, whereas the APG cases experience a larger decrease in shape factor of 5.9%. These observations are also present in the profiles at  $x_{ss}/c = 0.7$  shown in Figure 4 (right), where the  $Re_\tau$  values are 356 and 671 in the  $Re_c = 400,000$  and 1,000,000 wing cases, respectively. At this location, the increase in  $U_e^+$  is around 9.7% in the ZPG boundary layer, whereas in the APG case this increase is 8.8%. Moreover, the shape factor decreases by 2.5% from  $Re_\tau = 356$  to 671 in the ZPG boundary layer, whereas the wings exhibit a larger decrease of 4.5%. On the one hand, the shape factor is larger in APG TBLs, and decreases with Reynolds number as in ZPGs (which are PG TBLs with  $\beta = 0$ ). Interestingly, the decrease in the APG case is more pronounced than the one observed in ZPG boundary layers, a fact that suggests that the values of  $H$  in the low- $Re$  boundary layer are more severely affected by the APG than the ones at higher Reynolds numbers. On the other hand, the values of the inner-scaled edge velocity increase both with Reynolds number and with the APG, since in both cases the boundary layer grows and experiences a reduction in the velocity gradient at the wall. The fact that the increase in  $U_e^+$  is larger in the ZPG case than in the APG indicates that in the low-Reynolds-number case the boundary layer experienced a stronger effect of the pressure gradient, therefore exhibiting a larger value of  $U_e^+$  which led to a lower increase than in the  $\beta = 0$  case. Thus, the evolution of  $U_e^+$  and  $H$  indicates that the low- $Re$  boundary layer is more sensitive to the effect of the pressure gradient than the high- $Re$ , when both boundary layers were subjected to the same  $\beta(x)$  distribution. Additional support for this claim can be found in the mean velocity profiles at  $y_n^+ \simeq 25$ , where the ZPG cases and the high- $Re$  wing exhibit almost identical values of the inner-scaled velocity  $U_t^+$ , but the low- $Re$  wing shows values below these in the two streamwise positions. Lower velocities in the buffer layer with respect to the ZPG are associated with strong effects of the APG, as documented for instance by Spalart & Watmuff (1993) or Bobke *et al.* (2017). Since these lower

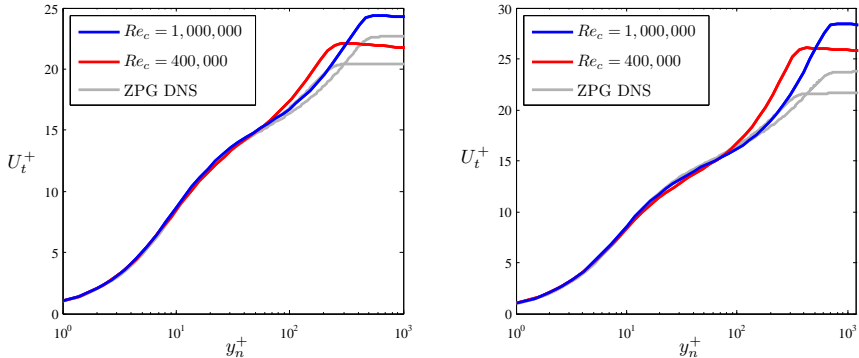


Figure 4: Inner-scaled mean velocity profiles at (left)  $x_{ss}/c = 0.4$  and (right)  $x_{ss}/c = 0.7$  for the two wing cases under study, compared with the DNS results of ZPG TBL by Schlatter & Örlü (2010) at matched  $Re_\tau$  values.

velocities are significant in the  $Re_c = 400,000$  wing, it can be stated that the effect of the APG is more pronounced in this case than in the high- $Re$  wing.

As discussed by Harun *et al.* (2013) or Bobke *et al.* (2017), the APG energizes the outer region of the boundary layer, producing more energetic turbulent structures. This effect is also observed when increasing the Reynolds number in a ZPG TBL, since as the boundary layer develops the outer region exhibits more energetic structures as shown for instance in the experiments by Hutchins & Marusic (2007) and the numerical simulations by Eitel-Amor *et al.* (2014). However, the mean velocity profiles shown in Figure 4 suggest that there may be differences in the way that this energizing process takes place, since the evolution of the mean flow parameters with Reynolds number is not the same in the  $\beta = 0$  (ZPG) as in the APG cases. In particular, it is interesting to note that at low Reynolds numbers the effect of the APG appears to be more prominent than at higher  $Re$ . Large-scale energetic motions develop in ZPG TBLs at increasing Reynolds number together with the development of the outer region of the boundary layer. The present results suggest that such development of the outer region takes place in a different way when an APG is present, a fact that is closely connected to the much larger wall-normal convection in APGs. In APG TBLs there are two complementing mechanisms responsible for the development of the boundary-layer outer region, namely due to  $\beta$  and due to  $Re$ . In order to further analyze the differences between these mechanisms, several components of the Reynolds-stress tensor are shown for the two wing cases at  $x_{ss}/c = 0.4$  and 0.7 in Figure 5. Note that we also show the inner-scaled streamwise velocity fluctuation profiles from the ZPG DNS by Schlatter & Örlü (2010) at matched  $Re_\tau$  values for comparison. The first important conclusion that can be drawn from Figure 5 is the fact that all the components of the Reynolds-stress tensor exhibit a more energetic outer region in comparison with ZPG TBLs, as discussed for instance by Kitsios *et al.* (2016)

or Bobke *et al.* (2017). Moreover, in Figure 5 (left) it can be observed that the increase in the near-wall peak of the tangential velocity fluctuation profile  $\overline{u_t^2}^+$  from  $Re_\tau = 242$  to 449 is of around 4.5%, which interestingly is approximately the same increase as in the wing cases. In fact, and as discussed by Eitel-Amor *et al.* (2014), the wall-resolved LES method employed in the present study slightly attenuates the near-wall peak of  $\overline{u_t^2}^+$ , a fact that would indicate that the increase in the wing boundary layers is slightly larger than in the ZPG. On the other hand, the  $Re_c = 400,000$  wing exhibits a much more energetic outer region than the corresponding ZPG case at the same  $Re_\tau$ : for instance, at  $y_n^+ = 100$  the low- $Re$  wing case shows a  $\overline{u_t^2}^+$  value 41% larger than the ZPG at the same location. On the other hand, this difference is significantly lower in the high- $Re$  wing, where the  $\overline{u_t^2}^+$  is only around 17% higher than the ZPG at  $y_n^+ = 200$  (note that this wall-normal location corresponds to  $y_n/\delta_{99} \simeq 0.29$ , *i.e.*, approximately the same distance from the wall in outer units as in the low- $Re$  case). This suggests that in the low- $Re$  APG there is a higher energy concentration in the outer region than in the high- $Re$  one. This is further confirmed by the results shown in Figure 5 (right) at  $x_{ss}/c = 0.7$ , where the  $Re_\tau$  values are 356 and 671. Firstly, the increase in the near-wall peak of  $\overline{u_t^2}^+$  is slightly larger in the APG boundary layers (5.1%) than in the ZPG (4.5%), a difference that could be larger if the fact that the well-resolved LES slightly attenuates the near-wall peak in the high- $Re$  case. However, the most significant result in Figure 5 (right) is the fact that both APG boundary layers exhibit a plateau in the outer region of the tangential velocity fluctuation profile. In particular, the  $\overline{u_t^2}^+$  value in this plateau is larger in the lower- $Re$  wing (5.75) than in the high- $Re$  case (5.0). Since the high- $Re$  wing exhibits a larger value of the near-wall peak, the ratio between this maximum and the plateau in the outer region is significantly larger in the  $Re_c = 1,000,000$  case (1.78) than in the  $Re_c = 400,000$  wing (1.48). This is a very relevant result, since it shows not only that the energizing mechanisms of the outer region in the boundary layer are different when they are connected to APG than when they are associated to  $Re$ , but also that lower- $Re$  TBLs are more sensitive to pressure-gradient effects than high- $Re$  ones. In particular, the tangential velocity fluctuation profiles show larger values in the outer region in the lower- $Re$  case, which is a manifestation of more prominent energy accumulation in the large-scale motions than in the high- $Re$  APG boundary layer.

#### 4. Summary and conclusions

The present study is aimed at further understanding the mechanisms responsible for the development of the outer region of TBLs and for the energizing of the large-scale motions, as well as their connection with APGs and increasing Reynolds number. To this end, we performed a well-resolved LES of the flow around a NACA4412 wing section at  $Re_c = 1,000,000$ , with  $5^\circ$  angle of attack, using the spectral-element code Nek5000. The setup is similar to the one

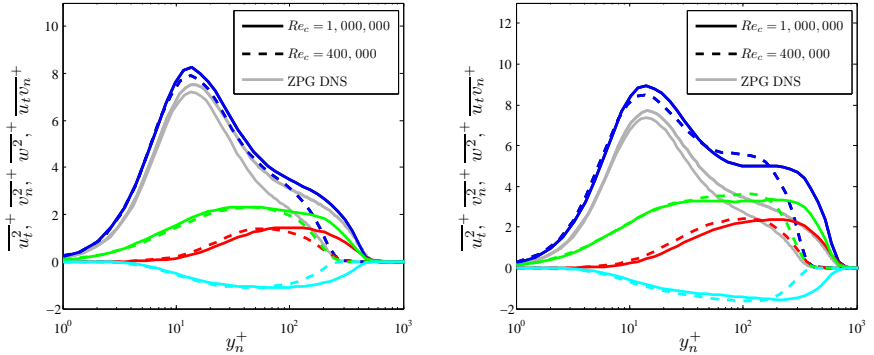


Figure 5: Selected components of the inner-scaled Reynolds-stress tensor at (left)  $x_{ss}/c = 0.4$  and (right)  $x_{ss}/c = 0.7$  for the two wing cases under study, compared with the DNS results of ZPG TBL by Schlatter & Örlü (2010) at matched  $Re_\tau$  values. The Reynolds stresses are represented as: — tangential — wall-normal and — spanwise velocity fluctuations, and — Reynolds shear stress.

employed by Hosseini *et al.* (2016) to perform a DNS of the same flow case at a lower  $Re_c = 400,000$ . The boundary layers developing on the suction side of the two wing sections are subjected to essentially the same streamwise Clauser pressure-gradient distribution  $\beta(x)$ , a fact that allows to characterize the effect of the Reynolds number in APG TBLs subjected to an increasing APG magnitude.

As a TBL develops, the increasing Reynolds number produces a more energetic outer region, a fact that is manifested in the Reynolds-stress tensor profiles. On the other hand, an APG also produces more energetic large-scale motions in the outer region of the boundary layer due to the lift-up effect and the increased wall-normal convection associated to it. Our results indicate that the skin-friction curve from the wing at  $Re_c = 1,000,000$  is below the one at  $Re_c = 400,000$  (up to around  $x_{ss}/c \simeq 0.9$ ), a fact that is consistent with the well-known effect of Reynolds number in ZPG TBLs. Moreover, the shape factor curve in the high- $Re$  wing is also below the one at  $Re_c = 400,000$ , which is associated with another effect of Reynolds number, *i.e.*, to reduce  $H$ .

We also analyzed the inner-scaled mean velocity profiles at  $x_{ss}/c = 0.4$  and 0.7, which are subjected to  $\beta$  values of 0.6 and 2, respectively. At  $x_{ss}/c = 0.4$ , the increase of  $U_e^+$  from  $Re_\tau = 242$  to 449 is 9.7%, which is lower than the increase in ZPG TBLs over the same  $Re_\tau$  range (11%). Similarly, at  $x_{ss}/c = 0.7$  the increase in  $U_e^+$  from  $Re_\tau = 356$  to 671 is 8.8%, also below the one in ZPGs, which is 9.7%. On the other hand, the shape factor is reduced at  $x_{ss}/c = 0.4$  by 5.9% and at  $x_{ss}/c = 0.7$  by 4.5% (compared to only 3.1% and 2.5% in the corresponding ZPG case). The steeper decrease in  $H$  and the more moderate increase in  $U_e^+$  compared to ZPG TBLs indicate that the lower- $Re$  APG is more

sensitive to pressure-gradient effects than the high- $Re$  one. This conclusion is supported by the observations on several components of the Reynolds-stress tensor, in particular in the tangential velocity fluctuation profile. Our results show that at  $x_{ss}/c = 0.4$  the lower- $Re$  wing exhibits a larger ratio of  $\overline{u_t^2}^+$  in the outer region with respect to the corresponding ZPG case than the high- $Re$  case, again indicating a more pronounced effect of the APG on the lower Reynolds number wing. Regarding the profiles at  $x_{ss}/c = 0.7$ , it is interesting to note that although the high- $Re$  wing exhibits a larger near-wall peak in  $\overline{u_t^2}^+$  than the lower- $Re$  case, the latter exhibits larger values in the outer region. Thus, while the former shows a value of 5.0 in the plateau located in the outer part of the  $\overline{u_t^2}^+$  profile, the latter exhibits a higher value of 5.75. Consequently, the ratio between the near-wall peak and the plateau in the  $\overline{u_t^2}^+$  profile is 1.78 in the high- $Re$  wing, and 1.48 in the lower- $Re$  case. This shows that the energy distribution in the two wing boundary layers, subjected to the same  $\beta(x)$ , is significantly different. Further analysis of these results will help to elucidate the differences in the mechanisms for outer-region energizing due to APG and Reynolds number.

## Acknowledgments

The simulations were performed on resources provided by the Swedish National Infrastructure for Computing (SNIC) at the Center for Parallel Computers (PDC), in KTH, Stockholm. RV and PS acknowledge the funding provided by the Swedish Research Council (VR) and from the Knut and Alice Wallenberg Foundation. This research is also supported by the ERC Grant No. “2015-AdG-694452, TRANSEP” to DH.

## REFERENCES

- BOBKE, A., VINUESA, R., ÖRLÜ, R. & SCHLATTER, P. 2017 History effects and near-equilibrium in adverse-pressure-gradient turbulent boundary layers. *J. Fluid Mech.*, Accepted .
- DONG, S., KARNIADAKIS, G. E. & CHRYSSOSTOMIDIS, C. 2014 A robust and accurate outflow boundary condition for incompressible flow simulations on severely-truncated unbounded domains. *Journal of Computational Physics* **261**, 83–105.
- EITEL-AMOR, G., ÖRLÜ, R. & SCHLATTER, P. 2014 Simulation and validation of a spatially evolving turbulent boundary layer up to  $Re_\theta = 8300$ . *Int. J. Heat Fluid Flow* **47**, 57–69.
- FISCHER, P. F., LOTTES, J. W. & KERKEMEIER, S. G. 2008 Nek5000 web page. <http://nek5000.mcs.anl.gov>.
- HARUN, Z., MONTY, J. P., MATHIS, R. & MARUSIC, I. 2013 Pressure gradient effects on the large-scale structure of turbulent boundary layers. *J. Fluid Mech.* **715**, 477–498.
- HOSSEINI, S. M., VINUESA, R., SCHLATTER, P., HANIFI, A. & HENNINGSON, D. S. 2016 Direct numerical simulation of the flow around a wing section at moderate Reynolds number. *Int. J. Heat Fluid Flow* **61**, 117–128.

- HUTCHINS, N. & MARUSIC, I. 2007 Evidence of very long meandering features in the logarithmic region of turbulent boundary layers. *J. Fluid Mech.* **579**, 1–28.
- JEONG, J. & HUSSAIN, F. 1995 On the identification of a vortex. *Journal of Fluid Mechanics* **285**.
- KITSIOS, V., ATKINSON, C., SILLERO, J. A., BORRELL, G., GUNGOR, A. G., JIMÉNEZ, J. & SORIA, J. 2016 Direct numerical simulation of a self-similar adverse pressure gradient turbulent boundary layer. *Int. J. Heat Fluid Flow* **61**, 129–136.
- LEE, J. H. 2017 Large-scale motions in turbulent boundary layers subjected to adverse pressure gradients. *J. Fluid Mech.* **810**, 323–361.
- LOKATT, M. 2017 On aerodynamic and aeroelastic modeling for aircraft design. Doctoral thesis, KTH Royal Institute of Technology.
- LOKATT, M. & ELLER, D. 2017 Robust viscous-inviscid interaction scheme for application on unstructured meshes. *Computers & Fluids* **145**, 37–51.
- MACIEL, Y., SIMENS, M. P. & GUNGOR, A. G. 2017 Coherent structures in a non-equilibrium large-velocity-defect turbulent boundary layer. *Flow Turbul. Combust.* **98**, 1–20.
- MARIN, O., VINUESA, R., OBABKO, A. V. & SCHLATTER, P. 2016 Characterization of the secondary flow in hexagonal ducts. *Phys. Fluids* **28**, 125101.
- MELLOR, G. L. & GIBSON, D. M. 1966 Equilibrium turbulent boundary layers. *J. Fluid Mech.* **24**, 225–253.
- MENTER, F. R. 1994 Two-equation eddy-viscosity turbulence models for engineering applications. *AIAA J.* **32**, 1598–1605.
- MONTY, J. P., HARUN, Z. & MARUSIC, I. 2011 A parametric study of adverse pressure gradient turbulent boundary layers. *Int. J. Heat Fluid Flow* **32**, 575–585.
- NEGI, P. S., VINUESA, R., SCHLATTER, P., HANIFI, A. & HENNINGSON, D. S. 2017 Unsteady aerodynamic effects in pitching airfoils studied through large-eddy simulations. In *Int. Symp. Turbulence & Shear Flow Phenomena (TSFP-10), July 6–9, Chicago, US*.
- SCHLATTER, P. & ÖRLÜ, R. 2010 Assessment of direct numerical simulation data of turbulent boundary layers. *Journal of Fluid Mechanics* **659**, 116–126.
- SCHLATTER, P. & ÖRLÜ, R. 2012 Turbulent boundary layers at moderate Reynolds numbers: inflow length and tripping effects. *J. Fluid Mech.* **710**, 5–34.
- SCHLATTER, P., STOLZ, S. & KLEISER, L. 2004 LES of transitional flows using the approximate deconvolution model. *Int. J. Heat Fluid Flow* **25**, 549–558.
- SKOTE, M., HENNINGSON, D. S. & HENKES, R. A. W. M. 1998 Direct numerical simulation of self-similar turbulent boundary layers in adverse pressure gradients. *Flow Turbul. Combust.* **60**, 47–85.
- SKÅRE, P. E. & KROGSTAD, P.-R. 1994 A turbulent equilibrium boundary layer near separation. *J. Fluid Mech.* **272**, 319–348.
- SPALART, P. R. & WATMUFF, J. H. 1993 Experimental and numerical study of a turbulent boundary layer with pressure gradients. *J. Fluid Mech.* **249**, 337–371.
- TOWNSEND, A. A. 1956 The Structure of Turbulent Shear Flow. Cambridge Univ. Press, Cambridge, UK.
- VINUESA, R., BOBKE, A., ÖRLÜ, R. & SCHLATTER, P. 2016 On determining characteristic length scales in pressure-gradient turbulent boundary layers. *Phys. Fluids* **28**, 055101.
- VINUESA, R., ROZIER, P. H., SCHLATTER, P. & NAGIB, H. M. 2014 Experiments

and computations of localized pressure gradients with different history effects.  
*AIAA J.* **55**, 368–384.

VINUESA, R., SCHLATTER, P., MALM, J., MAVRIPLIS, C. & HENNINGSON, D. S. 2015  
Direct numerical simulation of the flow around a wall-mounted square cylinder  
under various inflow conditions. *J. Turbul.* **16**, 555–587.

## Appendix A. Domain Validation

### A.1. Numerical setup

Validation study is performed in order to study the influence of domain truncation on the LES of flow around sections. The numerical setup is described in detail earlier in section 2 and the setup for the domain validation simulations follows a very similar approach. The airfoil used for the study is ED36F128 designed at the Aeronautics and Vehicle Engineering department at KTH, Stockholm, where several experiments have been performed for both static (Lokatt & Eller 2017) and dynamic flow cases (Lokatt 2017). The chord-based Reynolds number used in the investigation is  $Re_c = 100,000$  and the angle of attack is set to  $\alpha = 6.7^\circ$ . The spanwise width of the domain for all simulations was set to  $l_z/c = 0.1$ . The flow is tripped to induce flow transition on both the suction and pressure side of the airfoil at a chord-wise location of  $x/c = 0.1$ . Data from a RANS simulations with the  $k-\omega$  SST turbulence model is used to obtain the velocity field and the kolmogorov length scale  $\eta$ . The RANS velocity field data is imposed as Dirichlet boundary condition on the inlet and far-field boundaries. Periodic boundary conditions are applied on the spanwise boundaries of the domain. Simulations are performed using Nek5000 (Fischer *et al.* 2008) with an 11<sup>th</sup> order polynomial discretization. Velocity and length scales are normalized by free-stream velocity and chord length respectively. The grid resolution in the boundary layer around the airfoil is set such that  $\Delta x^+ \approx 18$ ,  $\Delta y_w^+ \approx 0.6$ ,  $\Delta z^+ \approx 9$ . In order to account for the varying shear-stress values over the airfoil the following rules are used for the determination of the resolution:

1. The  $u_\tau$  values from the RANS are used without modification in the region  $0.1 \leq x/c \leq 0.6$  for both the pressure (ps) and suction sides (ss).
2. For  $x/c > 0.6$ , the  $u_\tau$  from the pressure-side was used to design the mesh on both the suction and the pressure sides. The strong adverse-pressure gradient on the suction-side causes flow separation and  $u_\tau \approx 0$ . Thus the pressure-side is used to design the mesh on both sides.
3. For  $x/c < 0.1$ , a constant  $u_\tau$  value was used which was equal to the value at  $x/c = 0.1$  for both the suction and pressure sides.
4. The spectral-element distribution is uniform in the span-wise direction with the value of  $u_\tau$  at  $x/c = 0.25$  used for calculating the  $\Delta z^+$  spacing.
5. In the wake the criteria is based on the kolmogorov length scale  $\eta$ . The resolution in the wake is set such that  $\Delta x, \Delta y, \Delta z \leq 10\eta$ . The value of  $\eta$  is estimated from the RANS solution.

### A.2. Validation cases

Table 1 lists the different domain sizes tested in the present investigation along with the boundary condition used at the outlet boundary of the domain. All distances are measured from the leading-edge. All computational domains contain a curved inflow due to the C-grid type mesh topology. Thus the inlet distance is a radial distance from the leading-edge. A large reference case is set

up in order to compare the results of the simulations with domain truncation. The stress-free boundary condition is used at the outlet for the reference case. In the subsequent test cases the energy-stabilized outflow boundary condition as suggested by Dong *et al.* (2014) is used. The boundary condition has been shown to improve accuracy and numerical stability in severely truncated domains (Dong *et al.* 2014). A 2-D cross-section of the grid for the reference domain is

No.	Case Name	Inlet	Far-field	Outlet	Outlet B.C.
1	Reference	5c	5c	5c	Stress-free
2	FF1W3	1c	1c	3c	Dong
3	FF2W4	2c	2c	4c	Dong

Table 1: Validation cases

visualized in figure 6. Iso-contours of the instantaneous vortical structures in the flow-field for the reference case are depicted in figure 7. All simulations are run for 20 simulation time units and all statistics from the first 10 time units are discarded to remove initial transient effects.

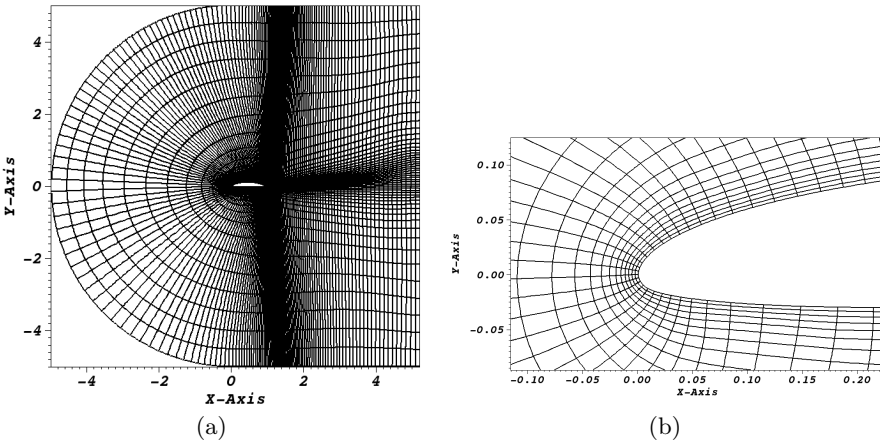


Figure 6: The simulation domain (a) and a close-up (b) near the leading edge, of the orthogonal and structured spectral-element grid for the reference case.

In the case FF1W3 the domain is truncated such that the far-field and inlet boundaries are one chord away from the airfoil ( $FF = 1$ ) and the wake region is truncated to three chords downstream of the leading-edge ( $W = 3$ ). Comparison of the wall-shear stress with the Reference case is shown in figure 8. Even with such a severely truncated computational domain, it is found that the flow field is only marginally disturbed with respect to the Reference case. The wall shear-stress ( $\tau_w$ ) deviates only slightly from the reference values and this deviation occurs near a local peak of  $\tau_w$  at  $x/c \approx 0.24$ .

For the case FF2W4 the domain size is slightly increased such that the far-field is now two chords away ( $FF = 2$ ) and the wake region is truncated

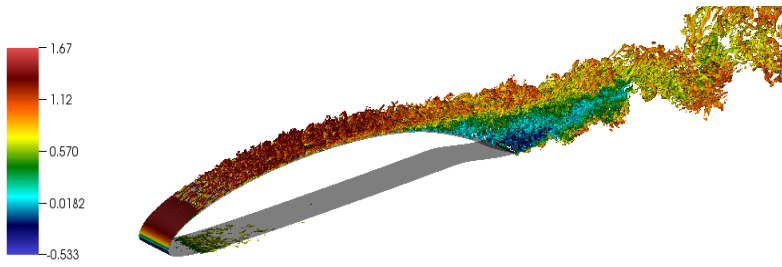


Figure 7: Visualization of the instantaneous flow structures identified by the  $\lambda_2$  criterion Jeong & Hussain (1995). The isocontours are colored by streamwise velocity.

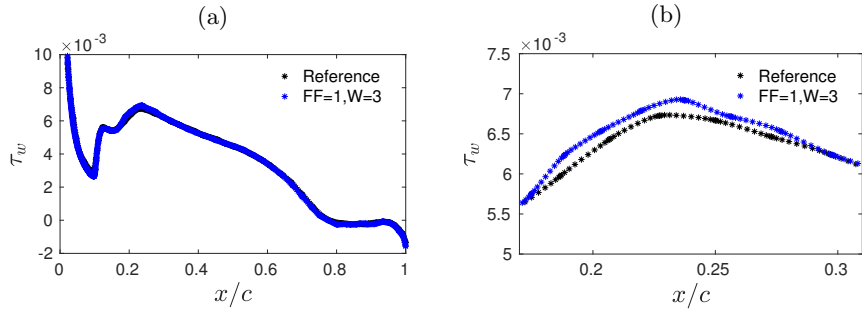


Figure 8: The suction-side wall shear-stress comparison for the case FF1W3 depicting (a)the chord-wise variation of  $\tau_w$  and (b) the close-up region near the peak of the wall shear-stress.

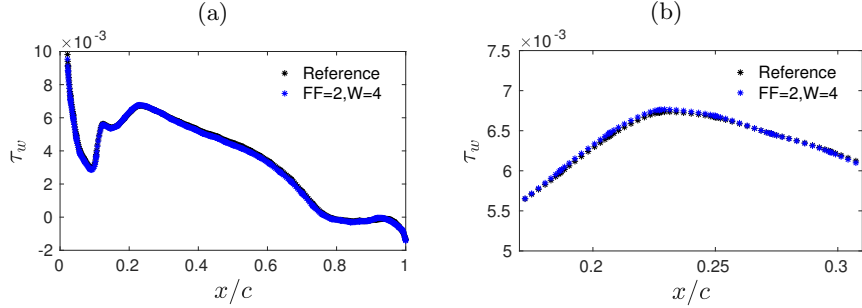


Figure 9: The suction-side wall shear-stress comparison for the case FF2W4 depicting (a)the chord-wise variation of  $\tau_w$  and (b) the close-up region near the peak of the wall shear-stress.

to four chords downstream of the leading-edge ( $W = 4$ ). The deviation of wall shear-stress nearly vanishes. Figure 9a shows the development of  $\tau_w$  across the airfoil which matches well with the reference case, and figure 9b shows the close-up region near the peak  $\tau_w$  where, unlike figure 8b, no large deviation from the reference case values is visible. Mean flow profiles (figure 10a) and

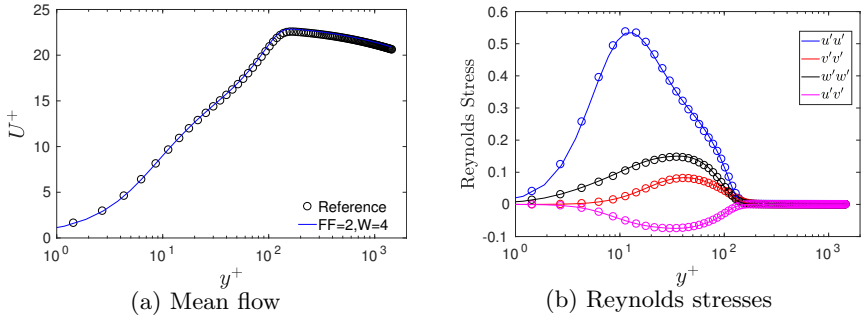


Figure 10: Comparison of wall-normal profiles of (a) mean tangential-flow and (b) Reynolds stresses for the case FF2W4.

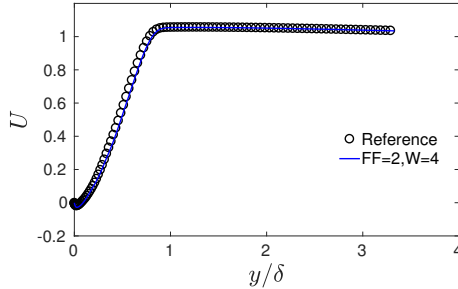


Figure 11: Comparison of mean tangential-flow velocity profile in the separated region on the suction-side ( $x/c = 0.85$ ).

Reynolds stress terms (10b), evaluated at  $x/c = 0.6$  on the suction side, are examined for this case. All the evaluated quantities show a good agreement with the reference case values. Furthermore, mean velocity profile is evaluated in the separated region at  $x/c = 0.85$  and even in the separated region a very good agreement is found as evident in figure 11. In the separated region  $\tau_w$  is nearly zero, therefore the mean velocity is normalized using the far-field velocity of  $U_\infty = 1.0$ . Figure 12a shows a 2D x-y section of the truncated domain with figure 12b showing a close-up of the grid near the leading edge. The setup is very similar to the Reference case (figure 6). Figure 13 shows the isocontours of flow structures identified by the  $\lambda_2$  criterion, which look qualitatively similar to the ones seen in the reference case (figure 7).

### A.3. Summary

Simulations of flow around a wing section with different domain sizes show that for a C-grid type mesh topology, flow distortion effects due to domain truncation and boundary conditions are minimized when the far-field boundary is two chords away from the airfoil leading-edge and the outflow boundary is four chords downstream of the leading-edge. The results are subject to the imposition of a RANS velocity field as Dirichlet boundary condition on the

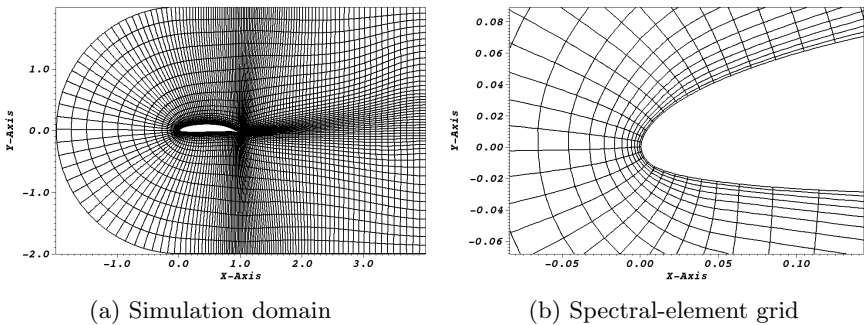


Figure 12: (a) Optimum truncated domain. (b) A close-up near the leading edge of the orthogonal and structured spectral-element grid. Domain is truncated such that the far-field is 2 chords from the airfoil and the outflow is 4 chords downstream from the leading-edge.

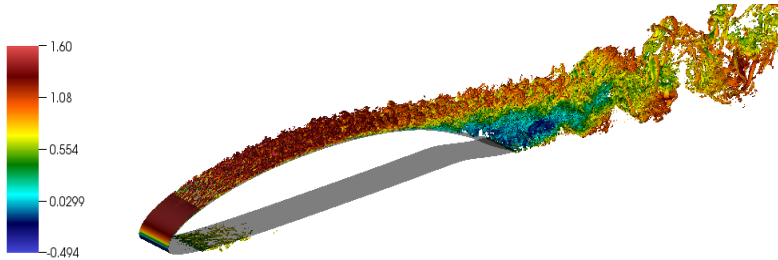


Figure 13: Visualization of the instantaneous flow structures in the truncated domain. The flow structures are identified by the isocontours of the  $\lambda_2$  criterion and are colored by streamwise velocity.

far-field boundaries and the energy-stabilized outflow boundary condition on the outlet boundaries of the simulation.